Università degli Studi di Palermo (UNIPA)
Dipartimento di Ingegneria (DI)
Université du Québec
Institut National de la Recherche Scientifique (INRS)
Centre Énergie, Matériaux et Télécommunications (EMT)

IMPLEMENTATION OF SIGNAL-PROCESSING FUNCTIONALITIES IN THE TERAHERTZ FREQUENCY DOMAIN

by
Giacomo Balistreri

Thesis or dissertation submitted to obtain the double Degree of
Philosophy Doctor (Ph.D.)
in Energy and Materials Science (EMT), Varennes, Quebec
and
in Information and Communication Technologies (DI), Palermo, Italy

Jury d’évaluation

Président du jury	Prof. Alessandro Busacca, University of Palermo, Italy
Examinateur externe	Prof. Andrea Fratalocchi KAUST, Saudi Arabia
Examinateur externe	Prof. Costantino De Angelis University of Brescia
Directeur de recherche	Prof. Roberto Morandotti INRS-EMT, Québec, Canada
Codirecteur de recherche	Prof. Salvatore Stivala University of Palermo, Italy
Codirecteur de recherche	Prof. José Azaña INRS-EMT, Québec, Canada

This work is dedicated to

my parents,

my brothers and sisters,

and my friends.

ACKNOWLEDGMENTS

I am really grateful to have known my advisors at INRS-EMT, Prof. Roberto Morandotti and Prof. José Azaña, and at University of Palermo, Prof. Salvatore Stivala. They have been foremost my mentors and inspiring figures, and set a remarkable example of what it means to be an experimental physicist. Thanks to them, I had the great opportunity to work on some important projects. Their insight into the concepts of this Ph.D. project, and their professional guidance have been continuously inspiring. I have been very fortunate to have them as advisors during my doctoral studies.

A special acknowledgment goes to Dr. Alessandro Tomasino and Dr. Junliang Dong, who taught me many useful and practical skills in my 4 years at INRS in Canada, and to always think out of the box to overcome the issues encountered on my way towards the achievement of this important milestone. It was great to work with them, and to consider them as friends during this journey.

I would like to thank also Prof. James van Howe, not only for the very interesting and fruitful science-related conversations and his creative approach, but especially for his valuable support and his precious help. Thank you for all the moments shared together, especially our traditional beers plus TV shows nights. Finally, thanks for pushing me to always give my best and never stop pursuing my goals. I have learned some very valuable lessons, and I will be always grateful for that.

I wish to thank my colleagues, both at INRS-EMT and University of Palermo, for the great time we spent together in the past years. Their support is something I am really grateful for, especially for the family-like love when I was thousands of kilometers away from my native country. They cheered me up and gave me the strength while here in Montreal. Achieving this goal would not have been possible without them. I am also grateful to those people who have been particularly close to me during the whole Ph.D. journey and made this experience something unique, funny and interesting.

Last but not least, I wish to thank my parents and my family, who have been supportive during my period in Montreal. They have always encouraged me to choose my own path and follow my dreams, even if this meant living far away from them. All of this would have been meaningless without them.

ABSTRACT

Terahertz radiation owns frequencies falling in the region of the electromagnetic spectrum between the microwave and far-infrared regions, i.e. between 0.1 and 10 THz. This region has been known for a long time as the “Terahertz gap”, mostly because of the lack of any reliable device operating in this specific frequency range. However, the tremendous efforts made towards the development of Terahertz technology in the past decades, has resulted in a significant decrease, if not almost a closure, of this technological gap.

Among the many interesting applications of Terahertz technology, we can find Information and Communication Technologies. As a matter of fact, in the past decades, we have observed a steep increase in the demand for higher bandwidths and data-transfer rates in wireless communications. Two of the most significant bottlenecks in current wireless communication systems are the atmospheric absorbance of the infrared signal, as well as the atmospheric turbulence, both ultimately leading to a misalignment of the infrared beam on the transceiver. Communication links employing Terahertz technology would exhibit several advantages over either the millimeter-wave or the infrared ones. More specifically, compared to the millimeter waves, Terahertz communication links would lead to a larger utilizable bandwidth, relative to the higher carrier frequency. On the other hand, they would result in a less susceptibility to scintillation effects, with respect to the infrared links. In order to accommodate the capacities for high data-rate transfers, which are strongly required for the design and building of new communication networks, it is crucial to design and implement signal-processing functionalities embedded in a Terahertz guiding structure, due to the many potential advantages of such an approach over free-space schemes, such as a more efficient performance of the designed component, as well as a larger compactness of the experimental set-up.

Following a brief introduction on Terahertz radiation, its properties and the state-of-the-art of the related technology, we will review the main waveguides, both dielectric- and metal-based, proposed and demonstrated so far, as well as the approaches adopted so far in the Terahertz domain for the design and realization of signal-processing operations. Additionally, we will briefly review the signal-processing components developed so far, by exploiting either free-space or waveguide-embedded approaches. Subsequently, we will show that it is possible to induce resonances across the low-frequency portion of the Terahertz spectrum, by exploiting the fabrication of trenches on one side of a parallel-plate waveguide, which causes the generation of Spoof Surface Plasmon Polaritons at the interface between a metal and a dielectric material. More specifically, we will report on the results obtained from the numerical investigations performed on the so-fabricated trenches on one of the wires of a two-wire waveguide with the goal of retrieving an optimal set of parameters that results in the occurrence of a single resonance in the whole Terahertz spectrum. Additionally, we will discuss the fabrication process of the samples, as well as the results obtained from their experimental characterization, which was performed via a typical Terahertz Time-Domain Spectroscopy setup.

Finally, we will report on how a tapered configuration of a two-wire waveguide, which exhibits a subwavelength value of the wire interspacing, i.e. the air gap between the two wires, results in a strong field enhancement of the Terahertz field coupled at its input. In more detail, the trend of the field enhancement obtained at the waveguide output closely resembles the ideal behavior of a first-order temporal integrator. Moreover, we will demonstrate that, a necessary condition that has to be satisfied in order to achieve such an enhancement, involves the values of the waveguide geometrical parameters, i.e. the wire radius and interspacing. After a detailed explanation of the theoretical aspects beneath this phenomenon, we will first show and discuss the results obtained from the numerical investigation of a similar structure, and then the experimental ones obtained from the characterization of the designed structure with a Terahertz Time-Domain Spectroscopy setup.

SOMMARIO

La radiazione Terahertz contiene quelle frequenze che ricadono nella porzione dello spettro elettromagnetico che si trova tra le microonde ed il lontano infrarosso, ovvero nell'intervallo di frequenze compreso tra 0.1 e 10 THz. Per lungo tempo, nel campo scientifico, ci si è riferiti alla radiazione Terahertz come "*Terahertz gap*", a causa della mancanza di dispositivi efficienti funzionanti in questa regione. Da allora, l'intenso lavoro svolto da molti gruppi di ricerca ha portato ad un notevole sviluppo in questo campo, avendo come risultato l'implementazione di diverse sorgenti e rivelatori. Questo, a sua volta, ha portato ad un significativo restringimento, se non una quasi totale chiusura, di questo *gap* tecnologico. Tra le tante ed interessanti applicazioni di questa particolare radiazione, sono sicuramente da annoverare quelle volte allo sviluppo del campo delle telecomunicazioni. Infatti, negli ultimi decenni, abbiamo potuto notare un rapido aumento nelle richieste per comunicazioni a banda sempre maggiore e per velocità di trasferimento dati più elevate. Allo stato attuale, i sistemi di comunicazione *wireless* mostrano due grandi problematiche, ovvero l'assorbimento atmosferico del segnale e la sensibilità all'umidità dell'ambiente, che risultano in un disallineamento del fascio infrarosso sul ricevitore. Lo sviluppo di un nuovo sistema di comunicazione basato sulla tecnologia Terahertz mostra diversi vantaggi su quelli già esistenti. Ad esempio, uno dei vantaggi rispetto ai sistemi basati sulle onde millimetriche riguarda la larghezza di banda utilizzabile, legata alla frequenza portante più elevata. Dall'altro lato, rispetto alle comunicazioni basate sulla radiazione infrarossa, le onde Terahertz sarebbero meno suscettibili agli effetti di scintillazione. Uno degli obiettivi principali da raggiungere per aumentare le velocità di trasferimento dati in un sistema di comunicazione basato sulla tecnologia Terahertz è la progettazione, nonchè l'implementazione di dispositivi integrati in strutture guidanti, che siano capaci di effettuare delle operazioni di *signal-processing* su un impulso Terahertz arbitrario al suo ingresso.

Nel contesto di questo progetto di ricerca, inizieremo la dissertazione fornendo una breve introduzione sulla radiazione Terahertz, sulle sue proprietà e sullo stato dell'arte della tecnologia in questo *range* spettrale. In seguito, introdurremo le principali guide d'onda, basate sia su materiali dielettrici e metallici, sviluppate finora in questo *range* spettrale, forniremo un'esaustiva panoramica sugli approcci adottati finora per la progettazione e la realizzazione di funzionalità di *signal-processing* nel campo Terahertz. In particolare, noteremo come uno degli approcci più efficaci sia l'integrazione di tali dispositivi in una struttura guidante, considerati i notevoli vantaggi che questa soluzione offre rispetto ad un approccio in *free-space,* come ad esempio una prestazione più efficace del dispositivo così implementato, e una maggiore compattezza. Vedremo inoltre come la tecnica principale impiegata finora per la realizzazione di filtri elimina-banda consista nella fabbricazione di solchi periodici sulla superficie di una guida metallica. Nel corpo di questa dissertazione mostreremo come, seguendo un simile approccio suna guida bifilare, sia possibile innescare delle risonanze nella parte inferiore dello spettro Terahertz, causate dall'eccitazione di plasmoni di superficie all'interfaccia tra un materiale metallico ed uno dielettrico. In particolare, mostreremo dapprima i risultati ottenuti dall'investigazione teorica di tale fenomeno, eseguita col fine di valutare l'effetto dei parametri geometrici dei solchi fabbricati sulla risposta spettrale del dispositivo. In seguito discuteremo il processo di fabbricazione di questi solchi, nonchè i risultati ottenuti dalla caratterizzazione sperimentale dei campioni fabbricati, eseguita impiegando un tipico sistema di spettroscopia Terahertz. Infine, dimostreremo che, confinando il campo Terahertz in una particolare configurazione della struttura bifilare, detta "a tromba", inneschi un arricchimento del campo elettromagnetico alla sua uscita, il cui andamento somiglia notevolmente a quello ideale di un integratore temporale del primo ordine. Più in dettaglio, dimostreremo che, una condizione necessaria al fine di ottenere un arricchimento del campo con un simile andamento coinvolge i parametri geometrici della guida, ad esempo il raggio del filo e la distanza tra i due fili. Dapprima introdurremo i risultati ottenuti dall'investigazione teorica di una tale struttura, ed infine quelli ottenuti dalla sua caratterizazzione sperimentale.

RÉSUMÉ

L’objectif principal de ce travail de thèse est la mise en œuvre de dispositifs intégrés dans des guides d’ondes qui sont capable d’accomplir des opérations de traitement du signal dans le domaine de la radiation Térahertz (THz). Le rayonnement Térahertz possède des fréquences qui se situent dans la région du spectre électromagnétique entre les régions des micro-ondes et de l’infrarouge lointain, c’est-à-dire entre 0.1 et 10 THz. Cette région est connue depuis longtemps sous le nom de « Térahertz gap », principalement en raison de l’absence de tout dispositif fiable fonctionnant dans cette gamme de fréquences spécifique. Toutefois, les efforts considérables déployés pour le développement de la technologie Térahertz au cours des dernières décennies ont permis de réduire considérablement, voire de combler presque entièrement, cette lacune technologique. Parmi les nombreuses applications intéressantes de la technologie Térahertz, on trouve les technologies de l’information et de la communication. En fait, au cours des dernières décennies, nous avons observé une forte augmentation de la demande de largeurs de bande et de taux de transfert de données plus élevées dans les systèmes de communication sans fil.

Deux des principaux problématiques des systèmes de communication actuels sont l’absorption atmosphérique du signal infrarouge, ainsi que les turbulences atmosphériques, qui entraînent toutes deux un mauvais alignement du faisceau infrarouge sur l’émetteur-récepteur. Les liaisons de communication utilisant la technologie Térahertz présenteraient plusieurs avantages par rapport aux ondes millimétriques ou aux infrarouges. Plus précisément, par rapport aux ondes millimétriques, les liaisons de communication en Térahertz conduiraient à une plus grande largeur de bande utilisable, par rapport à la fréquence porteuse plus élevée. D’autre part, ils entraîneraient une moindre susceptibilité aux effets de scintillation, si on le compare aux liaisons infrarouges. Afin d’accommoder les capacités de transfert de données à haut débit, qui sont fortement requises pour la conception et la construction de nouveaux

réseaux de communication, il est crucial de concevoir et de mettre en œuvre des fonctionnalités de traitement du signal intégrées dans une structure de guidage pour le rayonnement Térahertz, en raison des nombreux avantages potentiels d'une telle approche, par rapport aux schémas en espace libre, tels qu'une performance plus efficace du dispositif, ainsi qu'une plus grande compacité du dispositif expérimental.

Après une brève introduction sur le rayonnement Térahertz, ses propriétés et l'état de l'art de la technologie Térahertz, nous passerons en revue les principaux guides d'ondes, à base de matériaux diélectriques ou métalliques, proposés et démontrés jusqu'à présent, ainsi que les approches adoptées jusqu'à présent dans le domaine Térahertz pour la conception et la réalisation d'opérations de traitement du signal. En outre, nous donnerons un bref aperçu des dispositifs pour le traitement du signal développé jusqu'à présent, en exploitant soit l'espace libre, soit les approches intégrées aux guides d'ondes. Par la suite, nous montrerons qu'il est possible d'induire des résonances dans la partie basse fréquence du spectre Térahertz, en exploitant la fabrication de tranchées sur un côté d'un guide d'ondes à plaques parallèles, qui provoque la génération de polaritons plasmonique de surface à l'interface entre un métal et un matériau diélectrique. Plus précisément, nous rendrons compte des résultats obtenus à partir des investigations numériques effectuées sur les tranchées ainsi construites sur l'un des fils d'un guide d'ondes bifilaire dans le but de récupérer un ensemble optimal de paramètres qui aboutissent à l'apparition d'une seule résonance dans l'ensemble du spectre Térahertz. De plus, nous discuterons du processus de fabrication des échantillons, ainsi que des résultats obtenus lors de leur caractérisation expérimentale, qui a été réalisée par une installation typique de spectroscopie dans le domaine temporel pour le rayonnement Térahertz.

Enfin, nous expliquerons comment une configuration effilée d'un guide d'ondes bifilaire, qui présente une valeur de sous-longueur d'onde de l'espacement entre les fils, c'est-à-dire l'entrefer entre les deux fils, entraîne une forte augmentation du champ Térahertz couplé à son entrée. Plus précisément, la tendance de l'amélioration du champ obtenue à la sortie du guide d'ondes ressemble beaucoup au comportement idéal d'un intégrateur temporel du premier ordre. En outre, nous démontrerons qu'une condition nécessaire qui doit-être remplie pour obtenir une telle amélioration, implique les valeurs des paramètres géométriques du guide d'ondes, c'est-à-dire le rayon et l'espacement des fils. Après une explication détaillée des aspects théoriques de ce phénomène, nous montrerons et discuterons d’abord les résultats obtenus par les études numériques de telle structure, puis les résultats expérimentaux obtenus par la caractérisation de la structure conçue avec un dispositif de spectroscopie dans le domaine du temps pour le rayonnement Térahertz.

TABLE OF CONTENTS

CHAPTER 1

TERAHERTZ WAVES

1.1. INTRODUCTION TO THE TERAHERTZ RADIATION

Several frequency domains lie over the entire electromagnetic (EM) spectrum, including microwaves, infrared (IR) radiation, visible light and X-rays [1–3]. Terahertz (THz) radiation ranges between the microwave and the far infrared (FIR) regions of the spectrum, in a frequency range between 0.1 and 10 THz, as also shown in Figure 1.1. In the EM spectrum, radiation at a frequency of 1 THz, exhibits the following properties in vacuum [4]:

- Period of 1 ps;
- Wavelength of 300 μm;
- Wavenumber of 33 cm^{-1};
- Photon energy of 4.1 meV;
- Equivalent temperature of 47.6 K;

However, it is worth mentioning that some authors still talk about THz radiation even when they deal with EM waves exhibiting a frequency content partially covering the FIR region, i.e. between 10 and 30 THz [5]. The reason behind this extended definition is that this radiation is being generated and/or detected by sources and detectors able to manage extremely short time transients, with a continuum bandwidth spanning in a frequency window of several tens of THz. The very first experiment involving the generation of THz transients in quartz crystals is dated

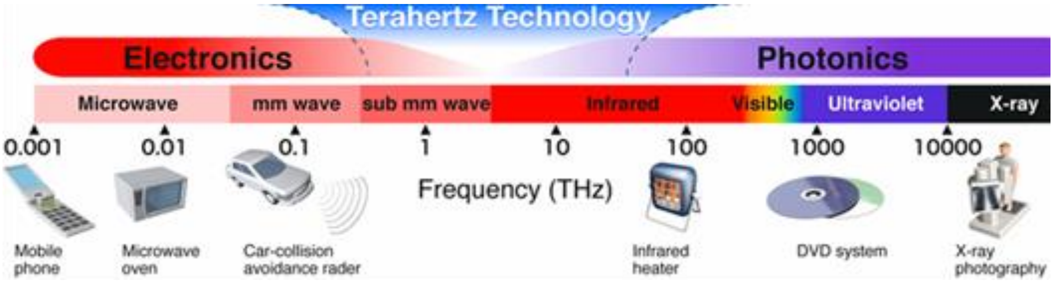

Figure 1.1. Typical subdivision of the electromagnetic (EM) spectrum. Terahertz (THz) radiation is located in the frequency range between the microwave (left-side, lower frequencies), and the far infrared (FIR, right-side, higher frequencies), i.e. between 0.1 and 10 THz, corresponding to a wavelength range between 0.03 and 3 mm [3].

in the early 1960s [6], right after the invention of the first laser system. After that, the investigation of this frequency window has been mostly set aside, mainly because of the poor interest, as well as the bare knowledge of the actual mechanism behind this type of radiation, especially if compared to the emerging optical domain, which was instead boosted by the ongoing development of the laser technology.

Another key factor that has hindered the development of the THz technology earlier in time was the lack of suitable emitters for THz radiation, as well as efficient sensors able to both collect and record it. Therefore, this portion of the EM spectrum has been known as “Terahertz gap” for a long time, due to the inability to realize systems able to either generate or detect (and, in general manipulate) the information carried by a THz transient in an efficient way. However, since then, there has been a tremendous effort in order to fill this gap, leading to its significant decrease, if not almost to its closure. As a matter of fact, it was through the development of ultrafast optoelectronics, which led to the successful generation and detection of THz pulses in the middle 1980s [7–10], that the interest in this particular type of radiation finally bloomed. Later on, the development of ultrafast chirped pulsed laser systems, able to emit optical pulses with temporal duration in the femtosecond scale, significantly contributed to the further advancement of research in the THz domain [11–13]. Since then, a plethora of new and exciting opportunities has emerged in the area of THz science and technology, with potential applications in many research and industrial fields, such as imaging, spectroscopy, microelectronics, and telecommunications [14–18]. The properties and behavior of THz radiation are governed by Maxwell's equations, but they are not as easy to handle, mainly because of their specific location in the EM spectrum. For this reason, it has been necessary to develop new principles, technologies and tools that would allow for a better understanding, and in general for the manipulation of this kind of EM radiation. In spite of all the difficulties experienced through the first years of research in this field, the unique nature and properties of THz radiation have stimulated several research groups worldwide to further develop this frequency band. For instance, over the past two decades, this region of the EM spectrum has been the focus of an extensive investigation for applications in spectroscopy, driven by the unique properties of Terahertz Time-Domain Spectroscopy (THz-TDS) [19]. This technique has been found to be crucial for spectroscopic characterization, i.e. in terms of frequency response, of different materials in the THz domain. As a consequence, it has attracted particular interest in different fields, such as material science [20,21], quality control [22], and medicine [23,24]. In more detail, many biological and chemical compounds (mostly polar molecules) exhibit distinct signature responses to THz radiation, usually referred to as "fingerprints", because the energy levels of their molecular vibrational and rotational modes fall in this frequency range. Additionally, THz radiation exhibits a non-ionizing nature, so that it is essentially harmless for the human body. Therefore, it shows a great potential for imaging applications in several fields, such as industry, bio-medicine, and security [25–27]. Moreover, another field that could benefit from the peculiar properties of THz radiation is the Information and Communication Technologies (ICT) one [28], which is driven by the increasing demand for higher bandwidths and data-rates in wireless communication systems [18,29] (see Section 1.2 for more details).

In the THz domain, we can distinguish among three different spectral regimes of operation [2], based on the approaches adopted for both the generation and the detection of THz waves: continuous wave (CW), broadband (up to 4 THz) and ultra-broadband (up to 10 THz). In the framework of the Ph.D. project discussed in this dissertation, the main interest falls on the broad- and ultra-broadband THz regimes, for which several techniques have been developed for both the generation and the detection of THz pulses. In the broadband regime, THz radiation can be generated by means of either optical rectification (OR) in quadratic media, or photoconductive switches/antennas (PCAs), whereas for its detection, electro-optic (EOS) and photoconductive sampling (PCS) are the techniques of choice [7,30–36]. As far as the ultra-broadband regime is concerned, two color plasma is used for their generation, while Optically-Biased Coherent Detection (OBCD), Air-Biased Coherent Detection (ABCD), and Solid-State-Biased Coherent Detection (SSBCD), are employed for the detection of THz pulses [37–41].

1.2. MOTIVATION OF THE DOCTORAL PROJECT

The recent deployment of fifth-generation (5G) wireless networks is opening up to new horizons in mobile communications, inspired by the continuous demand for reliable, high-bandwidth communications for different applications, such as smart homes, Internet-of-Things (IoT), and virtual reality [42,43]. Fifth-generation networks promise to offer important connectivity advantages, such as energy saving, higher system capacity and higher data-rates [44,45]. In spite of the significant improvements offered by the newly-developed 5G communication systems, they will (most likely in the next 10 years) be barely able to fulfill the demands of future emerging systems [46]. In order to overcome the constraints intrinsic to 5G systems, a sixth-generation (6G) wireless system will need to be developed, with new and attractive features. The most important requirement for 6G wireless networks is the capability of handling massive volumes of data and very high data-rate connectivity per device [47]. Indeed, according to Edholm's law [18], the demand for point-to-point bandwidth in wireless short-range communications has doubled every 18 months over the past 25 years, as can be also observed in Figure 1.2. It is expected that, among the most important technologies and key factors that will drive the development of 6G, THz radiation will play a major role [48]. Current wireless communication systems suffer from some significant issues:

- Transceiver misalignment, which can be ascribed to the atmospheric turbulence and/or to the humidity fluctuations in the beam path;
- Atmospheric absorbance of the IR signal.

The main consequence of these issues is the variation in the atmospheric real refractive index [49], in both the temporal and spatial coordinates. Consequently, the location of the IR

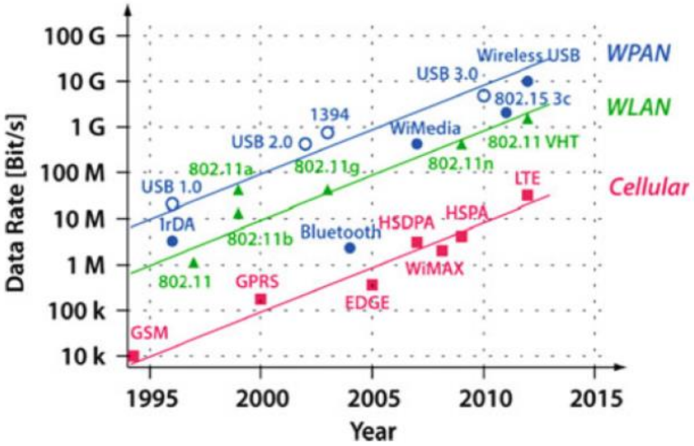

Figure 1.2. Trend of data-rates, measured in bit per second (bps) in wireless communication systems. According to Edholm's law, data-rates double every 18 months [17]. Note the different rates between wireless personal area network (WPAN, blue curve), wireless local area network (WLAN, green curve), and cellular network (pink curve). The figure is adapted from Ref. [28].

beam on the receiver tends to vary in time, an effect that is called scintillation. One might think that the current wireless IR links could be employed for the achievement of the targeted increase in data-rates, which will be one of the main requirements for the future communication networks. Unfortunately, this is not true, mainly because the ambient light noise at these wavelengths is significant. In more detail, the transmission of a symbol, i.e. either "0" or "1", needs some time to exceed the noise level. In order to transmit higher data rates (shorter time), the signal intensity would have to be increased. However, this solution cannot be adopted, because of the existing eye-safety limit [50]. Additionally, the increase in the signal intensity would also result in a higher power consumption, which would represent a significant drawback for battery-powered portable devices, such as smartphones, tablets, and laptops. THz communication links have been reported to exhibit several advantages over both the millimeter-wave and IR links. Among these, we can find the following [49,51]:

- Increased bandwidth capacity, if compared to the microwave systems, mainly due to the higher carrier frequency of THz radiation;
- Higher directionality than microwave or millimeter-wave (MMW) links, due to a less pronounced free-space wave diffraction, the latter being proportional to the wavelength;

- Less attenuation experienced under detrimental atmospheric conditions, such as fog and clouds, if compared to IR radiation [52].

Over the past few decades, several research groups have considered the prospects of employing THz waves as a means to transmit and receive data [53–55]. In fact, THz communication systems with gigabit per second (Gbps) or higher data-rates would enable a wide variety of large-bandwidth applications, such as wireless extensions of broadband access or high-speed fiber optical networks, as well as broadband indoor pico-cells to handle the high data demand from a number of mobile users [56–58]. However, there are still several challenges that must be addressed, mainly from the device and communications point of view, which would require innovative solutions, as well as the revision of well-established concepts in wireless communication systems.

For the realization of an efficient communication network in the THz domain, it is very important to design and realize several building blocks. Among these components, waveguides surely play a pivotal role, since they allow not only for the transfer of the THz signal over relatively long distances with minimal losses, while also enabling the possibility of routing the radiation towards designed points, and at the same time they allow to preserve both the amplitude and phase of the propagating pulse. Furthermore, the development of these waveguides would be beneficial also for THz-TDS systems, the efficiency of which would be strongly enhanced. However, the design and realization of efficient waveguide configurations in the THz domain is not trivial. This has to be mainly ascribed to the intrinsic properties of THz pulses, which usually exhibit a broadband nature, with their pulse duration being in the picosecond or sub-picosecond scale [7,31,59]. Consequently, the waveguides designed in this spectral region would have to guarantee both a low-loss and low-dispersive propagation [60]. Even though several waveguides have already been implemented by employing either metal or dielectric materials, most of these are not very efficient. On the one hand, metal waveguides usually exhibit high ohmic losses. Moreover, metal-based waveguides experience strong dispersion near the cut-off frequency of the guiding mode, unless they support transverse electromagnetic (TEM) modes, which feature no cut-off frequency [61]. On the other hand, dielectric materials feature high absorption losses, especially for frequencies above 1 THz [62].

Another major issue, which affects dielectric-based waveguides, is the group velocity dispersion (GVD), which ultimately leads to a dispersive temporal broadening of the input THz pulse (see Chapter 2).

In order to accommodate the capacities for the high data-rate transfers required to build the future communication networks, it is necessary to design and implement more complex blocks, such as devices able to successfully perform signal-processing operations on THz pulses [55,63], with large operational bandwidths, so that it is possible to cover most of the THz spectral range. Indeed, apart from their potential advantages for applications in the communications field, as already largely demonstrated in the case of telecom wavelengths, where λ_c = 1.55 μm, these devices would also allow for a significant performance boost of current THz-TDS schemes, enabling the implementation of post-processing operations, such as real-time signal reshaping, without recurring to computer algorithms or software. The achievement of such a goal requires the design and the realization of fundamental components, equivalent to their optical counterparts, such as filters, differentiators, integrators and so on, for the development of a wide variety of complex signal-processing and signal characterization functionalities [64]. Components that are able to successfully carry out these operations have already been proposed and demonstrated at telecom wavelengths. In most of the cases, these devices rely on the well-established optical fiber technology, by exploiting the very low propagation losses (~ 0.2 dB/km) intrinsic to optical fibers. Moreover, this choice was also driven by the possibility of exploiting the intrinsic properties of specific Fiber Bragg Grating (FBG) configurations to achieve the targeted spectral responses [64–68].

Conversely, the development and the applications of communication systems in the THz domain are still quite limited, mainly because of the challenges imposed by free-space propagation [69]. In more detail, there is a strong dependence on the atmospheric conditions, which mainly influences the low-frequency components of the THz spectrum. Moreover, handling THz beams in free-space requires the use of several components, which would ultimately result in bulky systems. An optimal solution for addressing these issues would be the employment of waveguides. In more detail, embedding the signal-processing functionalities in a THz waveguide would allow for several advantages with respect to a free-space approach. First, it would avoid the use of intermediate components, which would ultimately lead to the introduction of additional losses. Furthermore, the confinement of the THz field within the waveguide would result in devices with an enhanced efficiency, thus boosting their performance. Finally, the propagation of a THz beam coupled inside a generic waveguide would not be as significantly affected by the environmental conditions as it happens instead in free-space [69]. While the technology for the realization of signal-processing components has witnessed an impressive development in the optical domain, the same cannot be said about the THz domain. Indeed, in this case, the realization of THz signal-processing devices has been strongly hindered by the unusually broadband nature of the THz pulses. As a matter of fact, if compared to the optical pulses, where signals usually feature a very high frequency carrier wave, i.e. $f_O \sim 200$ THz, modulated via microwave techniques, i.e. $f_O \gg \Delta f_O \sim 0.01 - 1$ THz, THz transients obtained via optical down-conversion methods exhibit spectra with a bandwidth that is the same order of magnitude of the central frequency, i.e. $f_{THz} \sim \Delta f_{THz}$. A similar condition makes all the protocols that are usually employed in optical schemes, such as the specific characteristics of resonating structures [64,70], unsuitable for the implementation of analogous devices with operational bandwidths covering the whole THz spectral range. Throughout this dissertation, we demonstrate how it is possible to extend these functionalities to larger bandwidths, if not to almost the whole THz spectrum, by exploiting specific THz waveguide configurations, or by properly processing the guiding structure itself, e.g. with a micromachining process.

1.3. TERAHERTZ TIME-DOMAIN SPECTROSCOPY

As mentioned in the previous notes, THz-TDS has raised an ever-increasing interest, because of its exciting potential applications in several fields. The main advantage of this time-domain spectroscopy technique is the capability of retrieving the information about both the amplitude and the phase of the THz electric field, rather than its intensity, as instead happens in other spectroscopy techniques, such as the Fourier-Transform Infrared (FTIR) one [71]. Considering the relevance of THz-TDS systems in this dissertation, it is worth explaining the working principle behind this spectroscopy technique. Generally speaking, spectroscopy refers to the energy, or equivalently, to the frequency of the photons that propagate through a generic sample. By taking into account that the typical temporal duration (defined as the $1/e^2$ intensity) of the pulse to be detected is in the sub-picosecond or picosecond scale, it is necessary to employ a proper, fast and sensitive detection method for the THz electric field. Unfortunately, typical direct electrical detectors possess rise and fall times in the picosecond scale, so that they do not feature a sufficient temporal resolution. Therefore, in order to achieve the targeted sub-picosecond resolution, various proposed techniques exploit the train of pulses emitted by femtosecond laser systems, where the temporal duration (full-width at half maximum, FWHM) of the optical pulses is ~ 100 fs. The main optical pulsed beam is split along two paths, namely pump and probe beam. By doing so, the two optical pulses can be employed for both the generation and the detection of the time-dependent THz electric field. Therefore, the unknown profile of the THz electric field can be sampled with a femtosecond laser pulse, which is usually referred to as the *read-out* pulse. A generic sketch of a typical THz-TDS setup is shown in Figure 1.3. In general, a THz-TDS setup returns the convolution of the short optical pulse with the THz wave, which usually features a much longer pulse temporal duration. Moreover, the signal is read only as both the optical and the THz pulses arrive on the detector surface, thus allowing to measure the THz electric field as a function of time. Additionally, this spectroscopy technique is sensitive to the sign of the electric field, because the signal measured by the optical detector is the instantaneous THz field amplitude. In order to measure the signal over a wide temporal window, it is necessary to delay the optical pulse relatively to the THz pulse. This task is accomplished by employing a mechanical delay line, which is placed on either the generation or detection arm, as shown in Figure 1.3, and is usually controlled via software.

An issue concerning the THz-TDS schemes is that the water vapor shows strong absorption features in the THz range, which can interfere with the measurements [72]. To minimize the contribution from this absorption, the THz beam path (between emitter and detector) is usually enclosed in a box, which is purged with inert gases, such as Argon (Ar) or nitrogen (N_2). Since these gases do not absorb THz radiation, the absorbance peaks in the THz spectrum, caused by the presence of the water vapor, are removed. As an example, in Figure 1.4 we show a comparison between the THz spectra corresponding to the temporal waveforms retrieved with (blue solid line) and without (red solid line) nitrogen purging. We can immediately observe that employing the nitrogen purging leads to the removal of all the water

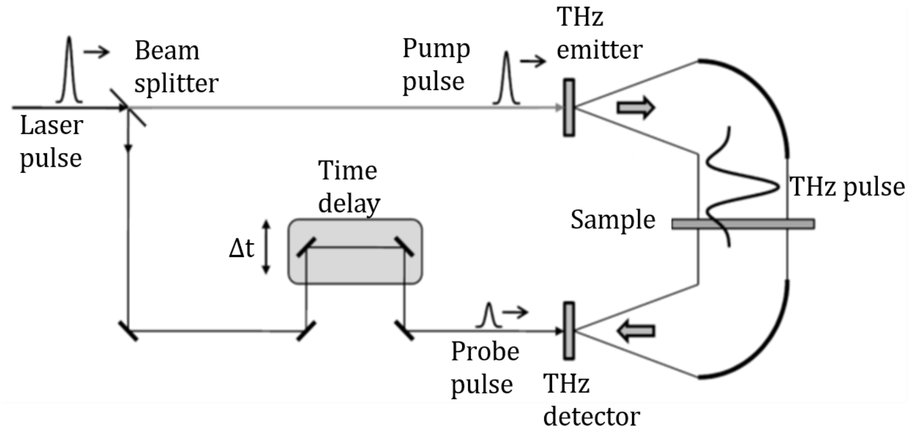

Figure 1.3. Schematic of a typical terahertz time-domain spectroscopy (THz-TDS) setup. The optical beam provided by the laser source is split into pump and probe beams, by employing a beam splitter. The so-obtained beams are then used for both the generation and detection of THz pulses. A mechanical delay line, usually controlled via software, is placed on one of the two paths (detection path usually), to enable the retrieval of the THz electric field values at all time points, t_i, in the temporal scan window. The figure is adapted from Ref. [2].

vapor absorption peaks all over the THz spectrum. As aforementioned, by employing the THz-TDS setup, one recovers the temporal profile of the THz electric field. From the temporal domain, it is possible to retrieve the targeted information also in the frequency domain. To this end, one usually employs a Fourier Transform (FT) algorithm on the retrieved temporal waveforms. We recall here that the FT of a real-valued temporal waveform becomes complex-valued in the frequency domain. The spectrum corresponding to the temporal waveform can be evaluated as follows:

$$E(f) = \mathcal{F}[E(t)] = \frac{1}{\sqrt{2\pi}} \int_{-\infty}^{\infty} E(t) e^{-j2\pi f t} dt = A(f) e^{-j\phi(f)} \tag{1.1}$$

Here, $\mathcal{F}$ is the mathematical symbol for the FT, f and t are the frequency and time, while $A(f)$ and $\phi(f)$ are the amplitude and phase profiles of the retrieved spectrum, respectively. Equation (1.1) is valid in the case of continuous waves. Moreover, as shown in Eq. (1.1), the retrieved complex-valued spectrum can be separated in amplitude and phase, thus enabling

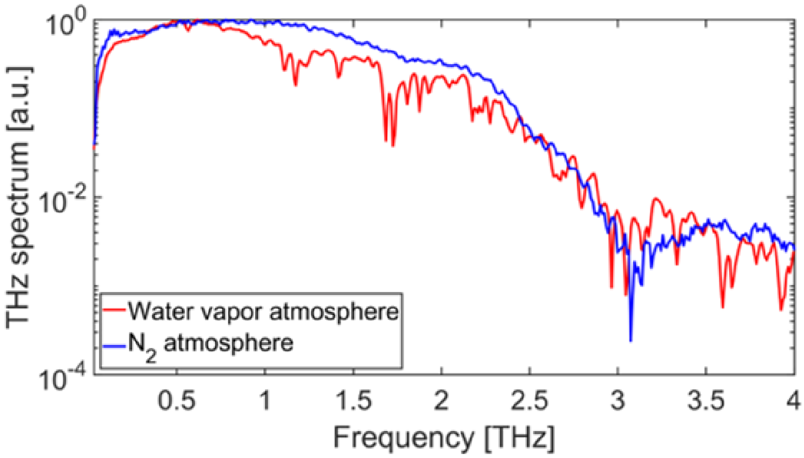

Figure 1.4. Experimentally-retrieved spectra corresponding to the THz electric field waveforms, with (blue solid line) and without (red solid line) nitrogen purging. Note the large difference between the two spectra, further highlighted by the presence of the water vapor absorption peaks in the red curve. These peaks eventually disappear as a consequence of the nitrogen purging (see blue solid curve). The spectra are normalized to their own maxima for a better visualization.

access to information on both properties. The possibility of measuring the spectra in this way allows for the direct determination of the complex-valued refractive index of the material under study, $n(f) = n_r(f) + jn_i(f)$, with $n_r(f)$ and $n_i(f)$ being its real and imaginary part, respectively, without the need to recur to the Kramers-Kronig relationships [73]. Another key parameter that can be determined from the information retrieved in the frequency domain is the absorption coefficient of a material under study. The properties reported in this section make THz-TDS a very powerful tool for the characterization of a large variety of materials and devices.

CHAPTER 2

TERAHERTZ SIGNAL PROCESSING

In the second chapter of this dissertation, we review the state-of-the-art of both waveguide configurations and components aimed at carrying out signal-processing functionalities in the THz domain. The design and the implementation of devices able to perform analog signal-processing operations in the THz domain, i.e. the manipulation of time-varying signals, has been intensively explored in the past years [74–77]. Nonetheless, most of the works reported so far involve operations that address the lowest part of the THz spectrum, i.e. below 0.5 THz. Unfortunately, we still observe a lack of operating devices capable of performing similar operations on broadband THz pulses, i.e. featuring operational bandwidths exceeding 1 THz, similarly to the solutions already implemented and routinely employed at telecom wavelengths [64].

2.1. INTRODUCTION TO SIGNAL-PROCESSING

“Signal-processing” is a term that typically refers to the analysis, synthesis, and modification of a signal detected at the receiver end. The term signal-processing also implies the extraction, as well as the modification, of information carried by the signals recorded at the receiver stage [78]. Therefore, it implies the modification of the signal properties, such as frequency, amplitude and phase [79,80]. The development and improvement of the signal-processing technology are key factors for the design, building and realization of novel communication systems, since the signals that arrive at the receiver may be affected by noise or other type of disturbances, such as linear and nonlinear signal distortions. Therefore, in order to be able to retrieve the correct information carried by the received signal, specific filters must be employed, so that it is possible to reject spurious contributions. This specific signal-processing operation is usually referred to as filtering. The variety of signal-processing operations that it is possible to implement is very large, such as frequency discrimination, phase comparison, signal correlation, temporal differentiation, temporal integration, and so on [81,82]. Additionally, if the information data are transmitted at very high speeds, then it might be necessary to down-convert the signal to a lower frequency region, so that both their manipulation and detection can be carried out in the electronic domain, where it is easier to process the signal itself. Nonetheless, the design and, in general, the implementation of signal-processing operations at the electronics level results in several issues [64,83–85], which are listed in Table 2.1. To give a relevant example, digital signal processors are strongly limited in the bandwidth that can be processed, i.e. < 5 GHz. The main issues listed in Table 2.1 have been cleverly overcome by implementing the abovementioned components entirely in the optical domain, i.e. with all-optical components [64].

The main approach adopted for the achievement of a similar task is the realization of ultrafast all-optical circuits that are able to emulate those already available in the electronic domain. While the strategies adopted for the design and the fabrication of these devices are very similar in the electronic and optical domain, the technology employed in the latter case is that already available in the optical domain, i.e. relying on the use of photonic components, such as FBGs or interferometers. More specifically, most of the basic signal-processing functionalities in the electronic domain, such as logic operations, differentiation and integration, have been achieved with a proper combination of different components, e.g. operational amplifiers, resistors and capacitors [82,86–89]. On the other hand, similar devices in the optical domain have been designed by exploiting either the peculiar properties of optical waveguides, or by relying on peculiar properties of nonlinear materials in the optical regime. The ability to process the input optical signals entirely in the optical domain, thus avoiding the down-conversion of

Electronic Signal-Processing	Optical Signal-Processing
Limited processing bandwidth (< 5 GHz)	Ultra-broad processing bandwidth (> 1 THz)
Need for optic-to-electric and/or electric-to-optic conversions in an optical network	Signals can be directly processed in the optical domain, without need for optic-to-electric and/or electric-to-optic conversion.
Sensitivity to electromagnetic interference	Immunity to electromagnetic interference.

Table 2.1. Comparison between the technology employed for electronic (left column) and optical (right column) signal-processing, with an emphasis on the drawbacks of the former and the advantages of the latter, in terms of processing bandwidth and sensitivity to electromagnetic interference.

the input signal, is also referred to as photonic signal-processing (PSP) [64]. In more detail, the first experimental demonstration of the FBGs, by Kawasaki *et al*. in 1978 [90], operating at telecom wavelengths, has represented a key point in the development of signal-processing components, such as differentiators, integrators, Hilbert transformers, and so on. For this task, different FBG configurations have been employed, such as phase-shifted FBGs [67], apodized uniform-period FBGs [91,92], long-period fiber gratings (LPGs) [65,93–95], and so on.

2.2. TERAHERTZ WAVEGUIDES

As mentioned in Section 1.2, the possibility of embedding the targeted signal-processing operations in a waveguide ultimately results in significant advantages, with respect to a free-space approach. In particular, it would allow for the realization of compact and portable devices, compared to those realized in free-space, which usually involve the use of bulk optical components. Moreover, the efficiency of the signal-processing functionality would be greatly enhanced by the confinement of the THz radiation in a volume size smaller than that it would occupy in free-space. By taking into account the crucial role that waveguides at THz frequencies can play in the design and implementation of signal-processing components with large operational bandwidths, in the following notes, we provide a comprehensive overview about the state-of-the-art of THz waveguides. Additionally, we explain in detail the motivations behind the choices made for the design and demonstration of the functionalities reported in this dissertation.

Generally speaking, a waveguide is a component that allows for the transportation of an electromagnetic wave from one place to another without significant losses in its intensity, while also confining the waveguide fundamental mode within the structure [2]. Waveguides have been commonly employed, in several regions of the EM spectrum, for a large variety of purposes, such as sensing and imaging probes [96,97], guiding an EM wave in sub-wavelength regimes [98,99], as well as to offer a tight confinement of the EM waves in the guiding structure, beyond the Rayleigh range [100,101]. The benefits coming from employing waveguides in other spectral regions are essentially similar to those attainable in the THz range. An interesting feature concerns the tight confinement of the waveguide fundamental mode, which could be potentially achieved by employing waveguides with sub-wavelength features. Such a property would be extremely beneficial for applications in different fields, such as THz sensing, where it is important for non-invasive molecular detection, as well as for spectroscopy of gases and/or liquids [102–104]. Nonetheless, there is a major issue in the development of efficient THz waveguides, mainly regarding the choice of suitable materials for their fabrication. As a matter of fact, dielectric materials usually suffer from a large dispersion, as well as large transmission losses at THz frequencies, while metals usually exhibit large Ohmic losses [105]. Generally speaking, both planar and not-planar waveguides can be divided into two major categories: dielectric-based and metal-based. Let us examine the properties of the commonly-employed dielectric- and metal-based waveguides at THz frequencies.

2.2.1. DIELECTRIC-BASED WAVEGUIDES

Several dielectric-based waveguides, which are generally employed for IR wavelengths, have also been proposed for use with THz radiation, such as dielectric ribbon waveguides [106], sapphire fibers [107], plastic photonic crystal fibers [108], sub-wavelength fibers [109,110], and so on. One of the main issues of dielectric-based waveguides is that they possess a large dispersion, as well as high values of the material absorption coefficient at THz frequencies, especially for frequencies above 1 THz. For instance, in Ref. [106] it has been reported that a THz pulse with a sub-picosecond temporal duration experiences a large broadening (more than 15 ps, with a positive chirp) when propagating within a plastic ribbon waveguide, made of high-density polyethylene (HDPE). Other analogous effects have been numerically and experimentally observed in other dielectric-based waveguides. Several research groups have proposed and investigated a large variety of low-loss materials, featuring different waveguide geometries, in order to address the dispersion loss issue. Among the alternative dielectric that could be employed for dielectric-based waveguides, we can find Teflon [111,112] and polyethylene [109], while the proposed waveguide geometries exhibit sub-wavelength structures [109,110,113]. With the aim of providing a general idea about the behavior of dielectrics at THz frequencies, in Figure 2.1 we show the properties of commonly-employed materials for the realization of THz dielectric-based waveguides [105]. In particular, in Figure 2.1(a) we illustrate the refractive index trend, while in Figure 2.1(b) we show the material absorption coefficients. More specifically, the data plotted in the figure refer to the following polymers: HDPE, polystyrene, polycarbonate, and Perspex (also known as polymethyl methacrylate, PMMA). From Figure 2.1(b), we can observe that the absorption coefficient exhibits large values, especially for frequencies greater than 1 THz.

Another approach that has been adopted to overcome the aforementioned dispersion issue, is the design of dielectric-based waveguides that exhibit sub-wavelength structures. By doing so, most of the THz radiation would be confined in the air volume, instead of the dielectric material. Nonetheless, these structures show issues related to narrow operational bandwidths and large losses at higher frequencies. In other words, such an approach would mostly favor the low frequency components of the propagating THz pulse, which are mainly located in the air region, so that they are not significantly attenuated during the propagation. On the other hand, the high frequencies are mostly located in the dielectric volume, thus experiencing a larger dispersion and absorption. Therefore, while such an approach favors the low-frequency components, it also penalizes the high-frequency ones, thus resulting in detrimental consequences on the whole THz spectrum. An additional issue concerning dielectric-based waveguides is the GVD, i.e. the change in the input THz pulse duration while propagating within the waveguide, due to the change of the wave-packet group velocity. This parameter, under a mathematical point of view, is defined as the first-order derivative of the inverse group velocity, with respect to the frequency [114]. This phenomenon ultimately results in different propagation velocities of the frequency components in the THz spectrum, which in turn leads

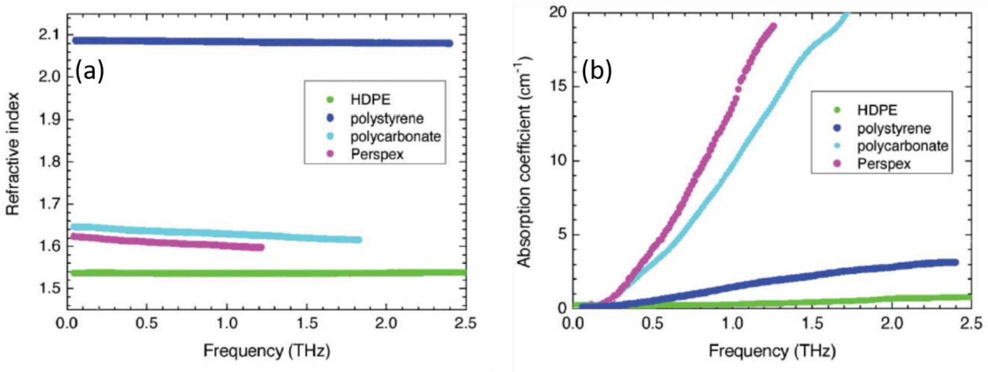

Figure 2.1. Behavior of the (a) refractive index and (b) absorption coefficient (measured in cm^{-1}), as a function of the THz frequency, of a few commonly-used dielectrics, i.e. high-density polyethylene (HDPE, green line), polystyrene (dark blue line), polycarbonate (light blue line), and Perspex (also known as polymethyl methacrylate, PMMA, purple line). All the data are recorded in a frequency range between 0 and 2.5 THz. Both figures are adapted from Ref. [103].

to a distortion of the pulse temporal profile. Group velocity dispersion represents a significant barrier, which limits the applications of dielectric-based waveguides, as well as their employment in THz communication systems. Furthermore, these waveguides suffer from waveguide (geometrical) dispersion [62]. Even though the latter could be tailored so to obtain a flat and almost zero dispersion region over certain frequency windows, it is not straightforward to design these waveguides so that they offer zero dispersion over the entire spectral bandwidth. Furthermore, due to the broadband nature of THz pulses, the implemented waveguides must allow for their low-loss and low-dispersive propagation. As such, in the framework of implementing waveguide-embedded signal-processing components, these are very important aspects, because they would allow for the realization of devices featuring larger operational bandwidths, possibly covering a major portion of the THz spectrum.

2.2.2. METAL-BASED WAVEGUIDES

Metal-based waveguides are more suitable than dielectric-based ones for the design of broadband waveguide-embedded signal-processing functionalities. In general, the configurations for the THz range are mostly scaled-down versions (in terms of dimensions) of well-known structures designed and demonstrated in both the microwave and radio-frequency

(RF) domains. One of the advantages of employing metals for the implementation of THz waveguides is that the corresponding wave would not be as dissipated in metals as it happens at higher frequencies. This has to be ascribed to the fact that the plasma frequency of most metals falls in the visible regime. Among the many topologies demonstrated so far, the most commonly used are the following: hollow circular waveguides (HCWGs) [115], metal single-wire waveguides (SWWGs, also known as "Sommerfeld wires") [116–118], parallel-plate waveguides (PPWGs) [119–121], and two-wire waveguides (TWWG) [122–125]. In Figure 2.2 we show sketches of these structures.

The HCWG, the sketch of which is illustrated in Figure 2.2(a), supports a transverse electric (TE) wave as its fundamental mode, i.e. the TE_{11} mode, which features a radial polarization. THz pulses propagating in this structure usually experience a strong dispersion near the cut-off frequency, which can be ascribed to the stretching of the transmitted THz pulse. The higher frequencies travel at larger group velocities, thus arriving at the output earlier in time. Therefore, the THz pulse experiences a negative chirp [61].

The SWWG, shown in Figure 2.2(b), supports a transverse magnetic (TM) wave as its fundamental mode, i.e. TM_{01}. This structure shows remarkably low losses, as well as a low GVD. Even though this waveguide supports the propagation of high-order modes, such modes exhibit an attenuation coefficient so large that the SWWG quickly tends to become single mode. In spite of this, it still shows some significant drawbacks. First, its performance is very sensitive to any possible perturbation of the wire, such as bending, or even to perturbations close to its surface, i.e. within the region of the extended field, such as corrugations on the wire surface, thus resulting in a loose confinement of the fundamental mode around the wire. A solution that has been proposed is the coating of the metal wire with a dielectric material, which would eventually result in an enhancement of the field quality. Unfortunately, this would also lead to the introduction of frequency-dependent losses to the propagation of the SWWG fundamental mode [117]. Another major drawback is the low coupling efficiency, because of the mismatch between the polarization of a freely-propagating THz beam and that of the SWWG fundamental mode. In other words, the SWWG fundamental mode is radially-polarized, and exhibits ring-

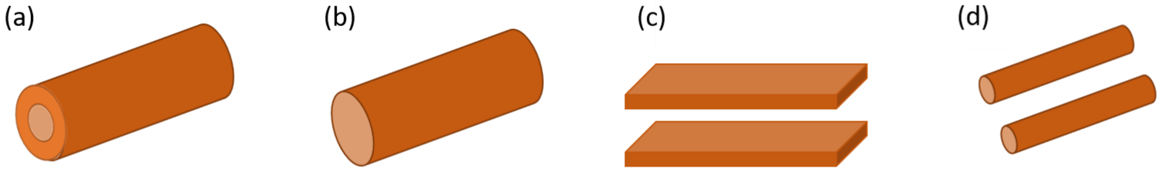

Figure 2.2. Schematics of commonly-employed metal-based waveguides for the confinement of THz radiation. (a) Hollow circular waveguide (HCWG), (b) Single-wire waveguide (SWWG), also known as "Sommerfeld wire", (c) Parallel-plate waveguide (PPWG), and (d) Two-wire waveguide (TWWG). To date, PPWGs and TWWGs are the commonly employed ones, because of their significant advantages over other configurations, in terms of field confinement, coupling efficiency, and transmission losses.

shaped coaxial modes around the wire. On the other hand, a THz beam propagating in free-space as generated by a THz source, exhibits a linear polarization, thus resulting in a strong polarization mismatch, which in turn implies a low coupling efficiency.

The PPWG, shown in Figure 2.2(c), supports the propagation of a single transverse electromagnetic (TEM) mode. More specifically, such a mode is the lowest-order TM mode (TM_0). Being a TEM mode, it exhibits no cut-off frequency and, therefore, unlike the HCWG, it is not affected by mode dispersion [126]. Furthermore, the PPWG fundamental mode exhibits a linear polarization, which is perpendicular to the plates, which allows for a higher coupling efficiency with respect to the SWWG. The main loss mechanism in this waveguide can be ascribed to divergence losses, related to the fact that the coupled THz beam is confined in the air gap between the two plates only along the direction perpendicular to the two plates. A summary of the properties of the metal-based waveguides reported in this section is listed in Table 2.2. In particular, we list the fundamental mode of each configuration, as well as their main drawbacks.

2.2.2.1. TWO-WIRE WAVEGUIDE

Almost a decade ago, a novel metal-based waveguide was theoretically investigated and experimentally demonstrated by Mbonye *et al.*, namely the two-wire waveguide (TWWG) [122], the sketch of which is illustrated in Figure 2.2(d). The design of the TWWG is very simple. It consists of two metal wires with an air gap between them, with the latter being

Waveguide typology	Fundamental mode	Main drawbacks
Hollow circular waveguide	Transverse electric (TE_{11})	Strong dispersion near cut-off frequency.
Single-wire waveguide	Transverse magnetic (TM_{01})	High radiation losses due to perturbations on the wire surface. Polarization mismatch between THz beam and fundamental mode.
Parallel-plate waveguide	Transverse electromagnetic (TM_0)	Fundamental mode spreads in the unguided direction, leading to divergence losses.

Table 2.2. Summary of the main properties of the fundamental mode of each of the investigated metal-based waveguides, i.e. hollow-circular waveguide (HCWG), single-wire waveguide (SWWG), and parallel-plate waveguide (PPWG). In the right-side column, we provide a summary of their main drawbacks.

constant along the direction of propagation of the coupled THz field. Even though for its first demonstration, the wires were made of stainless steel, to date the material of choice for this waveguide is copper, because of its excellent properties in the THz range, as well as, for instance, its good malleability [2]. Furthermore, a comparison between the behavior of copper and other commonly-employed metals at THz frequencies, such as gold, aluminum, stainless steel and silver, is reported in Table 2.3, in terms of both conductivity and skin depth (or penetration depth). The skin depth, in a conductor, is defined as the depth below the surface of the conductor at which the current density has fallen to *1/e* of that at the surface [127]. Under a mathematical point of view, the skin depth of a conductor can be evaluated as follows [128]:

$$\delta = \sqrt{\frac{2}{\omega\sigma_0\mu_0}} \tag{2.1}$$

Here, ω is the angular frequency, σ_0 is the static electrical conductivity, and μ_0 is the vacuum magnetic permeability. As it can be inferred from Eq. (2.1), the larger the electrical conductivity of the metal, the smaller its skin depth, being inversely proportional to the former.

Metal	Conductivity @ 1 THz [MS/m]	Skin depth @ 1 THz [nm]
Silver	63.0	63.4
Copper	59.6	65.2
Gold	45.2	74.9
Aluminum	37.8	81.9
Stainless steel	1.45	418.07

Table 2.3. Comparison between the performance of metals at THz frequencies, in terms of conductivity, measured in MS/m, and skin depth, measured in nm. The values illustrated in the table are evaluated at a frequency of f = 1 THz. Note how silver and copper show better properties in terms of both the parameters, thus implying smaller dissipation losses during the propagation of the waveguide fundamental mode. Even though silver shows the best properties, it is more expensive and less available in commerce. Data are taken from Ref. [2].

Furthermore, a smaller skin depth implies smaller dissipation losses, since the propagating EM wave cannot penetrate much inside the metal. From Table 2.3 we can observe how copper exhibits a good behavior at THz frequencies, with its static electrical conductivity (59.6 MS/m @ 1 THz) being one of the highest, resulting in one of the smallest values for the skin depth (65.2 nm @ 1 THz). Among the metals shown in Table 2.3, only silver has better properties in terms of both conductivity and skin depth (63.0 MS/m and 63.2 nm @ 1 THz, respectively). Even though silver shows slightly better properties than copper, silver wires are less available in commerce and are more expensive. For all these reasons, copper wires are usually employed for the realization of TWWGs.

In the initial design of the TWWG, the major issue to be addressed was to hold the two wires as close as possible in the free space, while maintaining, at the same time, a constant interspacing between them all along the waveguide length. The first approach proposed for the accomplishment of this task relied on the use of a dielectric support, which is as long as the whole waveguide length, with the metal wires being placed in a cavity drilled inside it. However, this approach eventually resulted in both large dispersion and absorption of the THz pulse, especially at higher frequencies, thus nullifying the low-dispersive and low-loss propagation characteristics of the fundamental mode. A second and more efficient design involves the use of a metallic base plate (aluminum), which acts as the backbone of the structure.

Then, two 3-mm-thick dielectric slabs (PMMA) are attached to both sides of the aluminum base, via two pairs of metallic screws. A small hole is fabricated at the center of the PMMA holders by means of a milling machine and a standard wire drill, the diameter of which is chosen based on the desired wire interspacing between the two wires. Each of the two metal wires passes through both holed and is then wrapped around two external screws at each side, so that it is possible to maintain a uniform interspacing between the wires, as well as to keep the wires in tension while suspended in air. A picture of the so-fabricated TWWG is illustrated in Figure 2.3(a), where its length is $L = 10$ cm, the wire radius is $R = 127$ μm, and the wire interspacing is $2g = 300$ μm. A sketch of the same waveguide, seen from one of the two sides, is shown in Figure 2.3(b), together with the main geometrical parameters, e.g. wire radius (R) and wire interspacing ($2g$). One of the peculiarities of the TWWG is that it features a double-connected cross section, which results in a double axial symmetry, similarly to what happens in a PPWG. Therefore, the propagation of the THz radiation is supported by a TEM mode, resulting in a relatively high coupling coefficient at both the input and output ends, with freely propagating THz waves. Indeed, both the TWWG fundamental mode and the THz beam emitted by a common source exhibit a linear polarization. The fact that the TWWG supports a TEM mode results also in the lack of cut-off frequencies in the spectral response, since the dispersion relation of the TWWG is essentially identical to that of the propagation of the same THz wave in free-space, usually referred to as light line. This prevents an excessive broadening of the THz pulse duration during the propagation. Finally, the symmetric structure of the TWWG ensures an effective confinement of the radiation in the air space between the two wires, resulting in the possibility of bending the structure and routing the coupled THz radiation along a desired direction, by only inducing moderate losses and without the need of employing bulky optical components. For all of these reasons, the TWWG is an excellent candidate for both broadband and ultra-broadband applications in the THz communication field. Such a structure shows a crucial advantage over the PPWG, i.e. it allows for a tight two-dimensional mode confinement of the propagating fundamental mode. This aspect can be better understood from the field intensity distribution of the waveguide fundamental mode, evaluated at $f = 1$ THz, shown in Figure 2.3(c). Therefore, the TWWG can be employed for guiding the THz radiation over longer distances, with respect to the other metal-based waveguides [123]. Because of the many

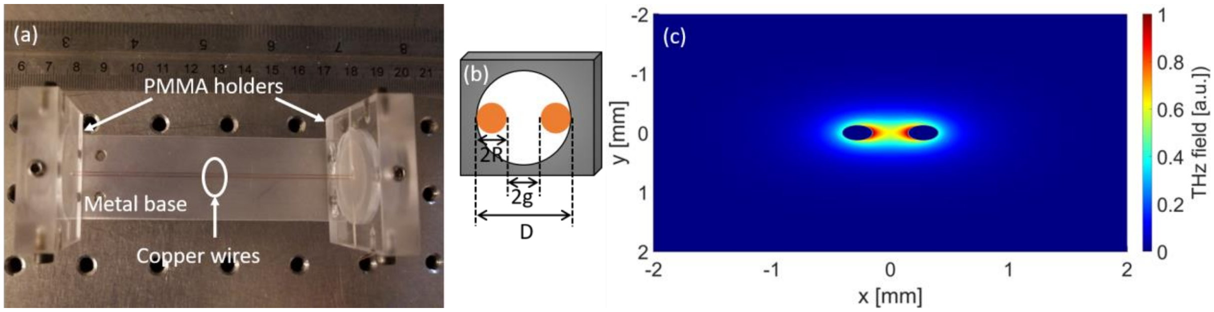

Figure 2.3. (a) Picture of a two-wire waveguide (TWWG), featuring a length of L = 10 cm, a wire gap of $2g$ = 300 μm, and a wire radius of R = 127 μm. Briefly, the metal base acts as the structure backbone, supporting the whole waveguide. Two dielectric (polymethyl methacrylate, PMMA) slabs are then attached to both ends of the metal base and have a hole drilled in their centers. Each of the copper wires passes through both holes and is then wrapped around a pair of external screws at each side of the holders, in order to allow for a uniform separation between the wires, as well as for maintaining them in tension while suspended in air. (b) Sketch of the dielectric holder for the copper wires, illustrating the main geometrical parameters, i.e. the wire diameter ($2R$), the wire interspacing ($2g$) and the diameter of the hole drilled on the slab surface (D), which ultimately determines the wire interspacing. (c) THz electric field intensity distribution of the TWWG fundamental mode, featuring the same geometrical parameters of that in (a). The fundamental mode is evaluated at a test frequency of f = 1 THz.

advantages of the TWWG over the other metal-based waveguides, this is an optimal configuration for the achievement of the goal of this doctoral project, i.e. the design and implementation of waveguide-embedded components aimed at carrying out signal-processing functionalities in the THz spectral region. As a matter of fact, as we explain in more detail in the following notes, the TWWG has already been employed for the implementation of band-rejection filters [123,129]. A more detailed overview of the most important properties of the TWWG is reported in Appendix A.

2.3. TERAHERTZ SIGNAL-PROCESSING

Generally speaking, signal-processing functionalities can be carried out according to either an analog (ASP) or digital (DSP) approach. In the first case, the processing is carried on continuous analog signals, with the term “analog” referring to something that, at least mathematically, can be represented as a set of continuous waves [130]. Typical ASP functionalities are passive and active filters, mixers, integrators and so on. On the other hand, DSP involves the use of digital circuit boards, which first sample the analog signal so to form a data bit stream and then process it digitally, with the aid of computers or embedded electronics [131,132]. In the THz domain, DSP is already exploited in different software-based solutions, which borrow algorithms and concepts similar to those employed in the optical domain, e.g. filtering, deconvolution, compression, and so on. On the other hand, even though the development of devices for carrying out ASP functionalities on a THz pulse, such as modulators, filters, and so on, has been widely investigated in the last decades, most of these works have addressed ASP operations in the low-frequency part of the THz spectrum, i.e. $f < 1$ THz [133,134]. We can still observe a lack of operating devices capable of manipulating wideband THz pulses, i.e. featuring FWHM bandwidths exceeding 1 THz. This has to be mainly ascribed to the fact that, unlike optical pulses, THz transients generated via optical down-conversion methods feature single or quasi-single cycle transients. This results in a spectral content featuring a carrier frequency (f_{THz}) comparable in value with their linewidth, i.e. $\left(\frac{\Delta f_{THz}}{f_{THz}} \sim 1\right)$ [35,59,135,136]. Among the signal-processing components that have been employed so far in the THz range, we can find band-rejection filters [74,76,142,77,123,129,137–141], modulators [143–147], frequency synthesizers [148–150], and a first-order temporal differentiator [151]. The temporal differentiation of broadband THz pulses has been demonstrated by adopting a free-space approach, which involved the use of a transmission grating with a very small (sub-wavelength) grating period. Band-rejection filters have been demonstrated by adopting one of the following three approaches:

1. The use of properly-designed metamaterial surfaces [137,140,152];
2. The insertion of material sheets or meshes in the air gap of a TWWG [123,129];
3. The processing of the plate surface of a PPWG, such as the engraving of periodic trenches on it [74,76].

As far as the insertion of materials within a TWWG is concerned, this relies on either the use of a polypropylene mesh [123], or on the realization of periodic engravings on a paper sheet, by means of a laser engraving technique [129], resulting in the implementation of notch filters. For instance, in Ref. [123] the mesh originally consisted of both vertical and horizontal sets of polymer rods woven together, as can be seen in Figure 2.4(a). In order to obtain a one-dimensional periodic structure, the horizontal set of rods was stripped away. The resulting structure, shown in Figure 2.4(b), exhibited an average rod diameter of ~ 110 μm, with an average air spacing between them of ~ 140 μm, thus resulting in a period of ~ 250 μm. This structure exhibits a behavior very similar to that of an FBG at telecom wavelengths. More specifically, the periodic structure causes a perturbation of the effective refractive index, n_{eff}, *seen* by the THz beam propagating within the TWWG, thus inducing a Bragg resonance in its spectral transfer function, the frequency position of which can be theoretically determined by using the following relationship:

$$f_{Bragg} = \frac{c}{2pn_{eff}} \tag{2.2}$$

Here, f_{Bragg} is the frequency position of the Bragg resonance, c is the speed of light in vacuum, p is the period of the structure. The effective refractive index, n_{eff}, *seen* by the propagating fundamental mode can be retrieved by employing an eigen-mode solver, starting from the value of the complex refractive index of the material making up the rods at the frequency of choice. From Figure 2.4(c), it is possible to notice that the presence of the polymer mesh results in a clear time delay between the peaks of the temporal waveforms recorded after the propagation in the TWWG with (green solid line) and without (blue solid line) the polymer mesh in the air gap between the two wires. The time delay must be increased to the increase of the effective optical path length traveled by the THz pulse propagating within the TWWG with and without the polymer mesh. Furthermore, from the spectral transfer function of the device, which is shown in Figure 2.4(d), it is possible to observe a Bragg resonance at f_{Bragg} ~ 0.6 THz, with a depth of ~ 25 dB, and a linewidth of ~ 16 GHz.

A similar approach has also been adopted for the design and implementation of another THz band-rejection filter. In more detail, for the achievement of the task, a metal sheet was inserted in the air gap between the two plates of a tapered PPWG (TPPWG) [77]. More specifically, several slits, equally distanced along the field propagation direction, are engraved on the metal sheet, with a periodic distance, P. As the THz beam propagates in the so-

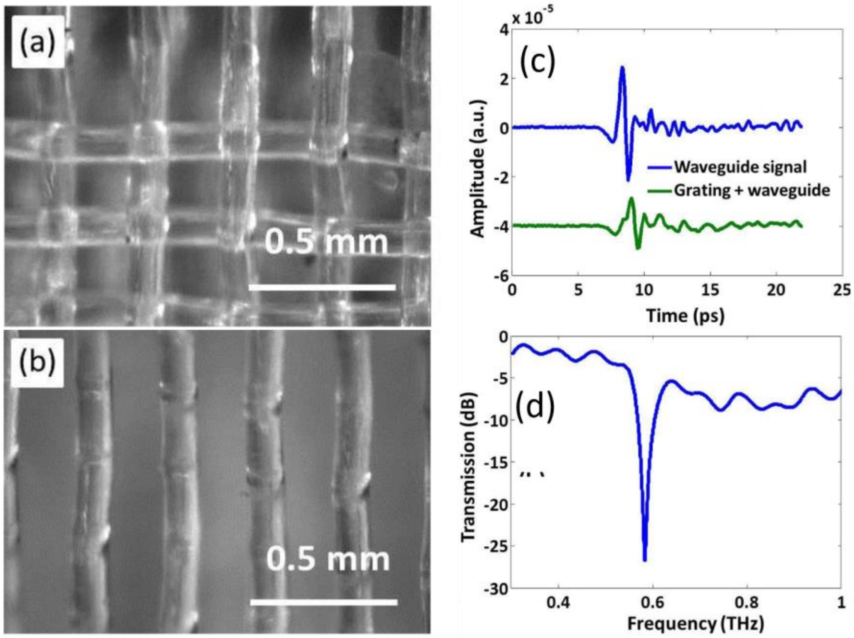

Figure 2.4. (a) Image, taken with an optical microscope, of the polypropylene mesh with both horizontal and vertical rods, and (b) of the same mesh after the horizontal rods were removed. (c) Experimentally-retrieved THz electric field temporal waveforms, via a THz-TDS setup, after propagation in a standard TWWG (blue solid line), and in the same waveguide with the polymer mesh placed in the air gap between the wires (green solid line). Note how the presence of the polymer mesh induces a delay between the peaks of the two waveforms, because of the increase in the THz beam effective path length. (d) Transmission spectrum, evaluated as the ratio of the spectra corresponding to the waveforms shown in (a). We can observe a strong resonance, due to the Bragg-like behavior of the structure, at ~ 0.6 THz, with a depth of ~ 25 dB, and a linewidth of ~ 16 GHz. The figures are adapted from Ref. [122].

implemented structure, a Bragg resonance is induced in its spectral response, the frequency position of which can be evaluated from Eq. (2.2). Furthermore, the linewidth of the induced resonance in the device spectral response increases as the period of the slits is decreased. Additionally, as the slit period decreases (increases) the frequency position of the Bragg resonance shifts towards higher (lower) values. The same concept has been exploited for the design and implementation of a low-pass filter. As a matter of fact, if slits with different periods are engraved on a metal sheet, then multiple Bragg resonances are induced in the spectral response, one for each different slit period. By choosing the slit periods so that the Bragg frequency positions are close enough to each other, a low-pass filter functionality is achieved at

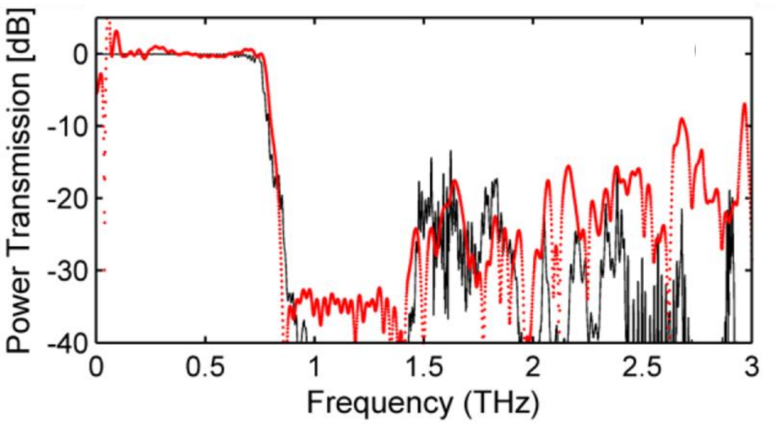

Figure 2.5. Comparison between the experimental (red dots) and simulated (black solid line) power transmission spectra, measured in dB, for the structure consisting of a metal sheet, which features slits with different periods. The metal sheet is placed in the air gap of a tapered parallel-plate waveguide (PPWG). A so-implemented structure induces a Bragg resonance for each period value in the spectral response. Due to the fact that the frequency positions of the induced Bragg resonances are very close to each other, this results in a low-pass filter functionality, with a cut-off frequency of around 0.8 THz. The figure is adapted from Ref. [76].

the output of the waveguide. In particular, in Ref. [77], the demonstrated low-pass filter exhibits a cut-off frequency, defined as the frequency value for which the amplitude of the transfer function is halved (~ 3 dB) compared to its absolute maximum value. In particular, Figure 2.5 shows a comparison between the device transfer function obtained from its numerical investigation (black solid line) and from its experimental characterization (red dots), where it is possible to observe that all the frequency components above ~ 0.9 THz are filtered out by the waveguide-embedded device.

Another approach that has been commonly adopted for achieving the stop-band frequency filtering in the THz spectral range, relied on the modification of the surface of a metallic THz waveguide. In particular, in Ref. [76] it has been proposed that the engraving of trenches on the plate surface of a PPWG results in the occurrence of resonances in the spectral response, the properties of which, such as the resonance frequency position and strength, are influenced by geometrical parameters of the trenches [45]. A sketch of the engraved structure is shown in Figure 2.6(a). The working principle behind this mechanism is the so-called Surface

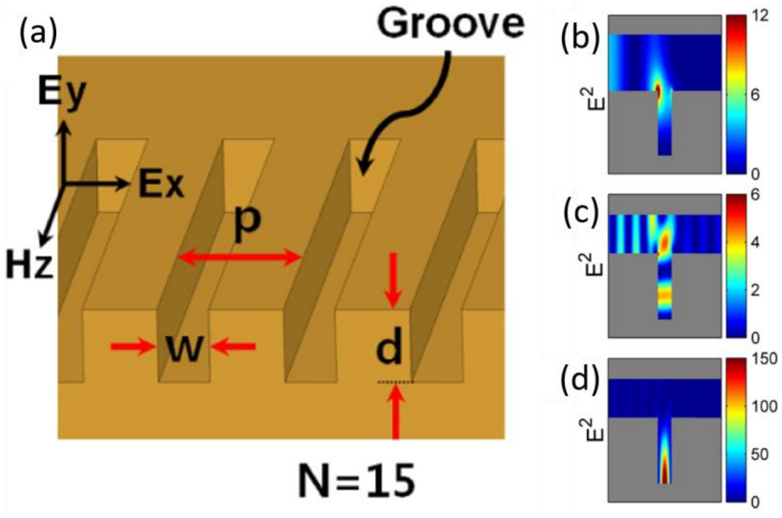

Figure 2.6. (a) Schematic of the grooves engraved on the surface of the plate of a tapered parallel-plate waveguide (TPPWG). Here, *p* is the grating period, i.e. the distance between two consecutive grooves, *w* is the groove width, *d* is the groove depth, and *N* is the number of grooves engraved on the plate surface. (b-d) THz electric field intensity distribution in the region close to the first groove, evaluated at the frequency positions corresponding to the different resonances induced in the device spectral response. The figure is adapted from Ref. [75].

Plasmon Resonance (SPR) [153], which is exhaustively explained in Chapter 3. As an example, the distribution of the THz electric field corresponding to the waveguide fundamental mode around the fabricated trenches is shown in Figure 2.6(b-d). These field distributions are evaluated at the frequencies corresponding to the resonances induced in the spectral response of the simulated device. Let us examine the nature of the resonances that can be triggered by this structure.

The resonance, the field distribution of which is shown in Figure 2.6(b) has to be attributed to the π-radians phase delay between the THz field component that propagates through the air gap in the proximity of the trenches and that trapped inside the first trench and then propagating towards the TPPWG output [76]. The resonance, the field distribution of which is shown in Figure 2.6(c), occurs only when the interspacing between the two plates becomes much smaller than the THz wavelength (sub-wavelength), with its frequency position depending on the values of both the plate interspacing and the groove depth. More specifically,

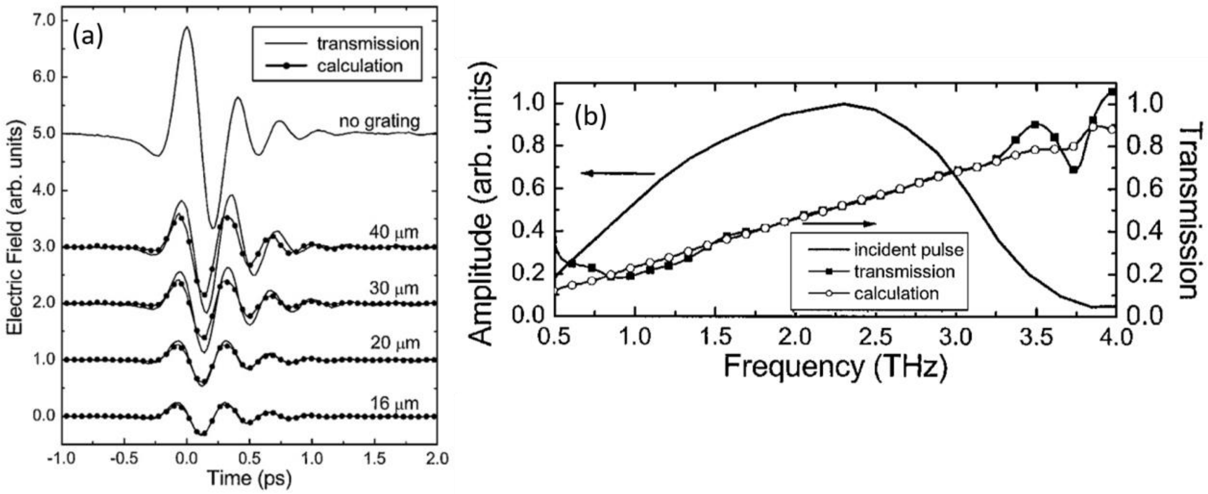

Figure 2.7. (a) Temporal profiles of the THz electric field measured after propagation through several metallic transmission gratings, featuring different periods. We show a comparison between the experimental (black solid line) and the numerically-evaluated (black dotted line) transmitted pulse, unveiling an improvement in the differentiation capability as the period is decreased down to sub-wavelength values. This enhancement is counterbalanced by a much smaller amplitude of the transmitted THz electric field. (b) Amplitude of the spectrum field (left axis) and transmission spectrum (right axis) of a transmission grating with a period of p = 10 μm. The operational bandwidth of the temporal differentiator ranges from 0.7 to 3.3 THz. The figures are adapted from Ref. [149].

this resonance is a vertically-localized standing wave (VLSW), the frequency position of which can be determined as follows:

$$f_{VLSW} = \frac{c}{d+g} \tag{2.3}$$

Here, c is the speed of light in vacuum, d is the groove depth, and g is the interspacing between the two plates. Finally, the resonance, the field distribution of which is shown in Figure 2.6(d), is a horizontally-localized standing wave (HLSW). In this case, the frequency position is dependent on the value of the trench width, and it shifts towards lower values as the trench width is increased, i.e. $f_{HLSW} \propto \frac{1}{2w}$. Therefore, the resonance frequency position is independent from the interspacing between the two plates.

Finally, in Ref. [151], Filin *et al.* proposed that a free-standing metallic transmission grating can be employed for the implementation of a broadband first-order temporal differentiator at THz frequencies. By properly setting the orientation of the grating grooves with respect to that of the incident THz field, it was demonstrated that the transmitted THz pulse is reshaped and closely resembles the first-order temporal derivative of the incident pulse. The necessary condition to be satisfied in order to achieve the differentiation functionality is that the orientation of the grooves must be parallel to the polarization of the incident THz pulse. If the latter condition is not satisfied, i.e. if the orientation of the grooves is perpendicular to the polarization of the incident pulse, the latter is mostly not affected by the propagation through the transmission grating. Furthermore, the differentiation capability of the grating is significantly improved as the grating period is decreased to values that are much smaller than the THz wavelength, as shown in Figure 2.7(a), yet at the expenses of the overall power transmission through the device. Remarkably, as one can also observe from the device transfer function, which is shown in Figure 2.7(b) (right-axis), the spectral range where the differentiation can be achieved is quite broad, i.e. from around 0.7 to 3.3 THz.

CHAPTER 3

FREQUENCY FILTERING VIA SURFACE PLASMON RESONANCE

In this chapter we report and discuss on the theoretical investigation and experimental demonstration of band-rejection filters for THz pulses, the working principle of which is based on the surface plasmon resonance (SPR) effect. In more detail, the phenomenon is triggered by the modification of the waveguide surface, achieved for instance by etching grooves and/or trenches on the surface of one of the wires in a TWWG. By properly choosing a set of values for their geometrical parameters, e.g. depth, width, and period, it is possible to filter out one or more frequency windows in the THz spectrum, featuring a narrow bandwidth. In other words, the etching of trenches on the wire surface results in the occurrence of resonances in the device spectral response at specific frequency positions, which are dependent on the values of the trenches geometrical parameters.

3.1. THEORETICAL ASPECTS

The aim of this introductory section is to provide an exhaustive theoretical background of several aspects that are strictly related to the simulation and experimental results reported and discussed in this chapter. In more detail, we start by introducing SPR and the dynamic behind the generation of Surface Plasmon Polaritons (SPPs) at optical frequencies and Spoof Surface Plasmon Polaritons (SSPPs) at THz frequencies. Moreover, we provide a comprehensive theoretical explanation of the generation and detection techniques employed for the retrieval of the experimental results discussed in this chapter. In particular, we discuss the THz generation via photoconductive antennas (PCAs) and detection via free-space electro-optic sampling (FS-EOS).

3.1.1. SURFACE PLASMON RESONANCE

Plasmonics is an interesting and attractive area of technology, where the propagation of EM waves can be controlled by exploiting sub-wavelength structures, which exhibit geometrical features that are much smaller (in size) than the central wavelength of the propagating EM wave [154]. With the rapid development of optical technology, systems for data transmission require a highly increasing degree of integration of the devices, which could potentially allow for higher data transmission rates [155,156]. Nonetheless, as the technology advances, it becomes more and more difficult to reduce the size of individual elements in optical devices, due to the well-known diffraction limit to about one-half of the optical wavelength [157]. The excitation of SPPs could result in a boost of the confinement of the propagating radiation in a volume size even smaller than that allowed by the diffraction limit. Therefore, it is a promising approach that can be employed for the control and manipulation of the light propagation, which at the same time allows for a remarkable enhancement of the near-field. Therefore, this phenomenon is nowadays exploited for sensing purposes in biochemistry [158–160], or applications where resolution is a crucial factor, such as imaging [161,162].

The mechanism behind the generation of SPPs has been investigated for many decades [163,164,173,165–172]. Finally, it was postulated that surface plasmons (SPs) are generated when a propagating EM wave interact with the free electrons present at the interface between a metal and a dielectric. In more detail, due to the opposite sign of the absolute dielectric permittivity of metals and dielectrics (the former being negative and the latter positive) at optical frequencies, the incident light combines with the SPs, leading to the generation of selfsustaining and propagating EM waves, known as SPPs [174]. Once excited, the SPPs travel along the direction parallel to the metal-dielectric interface. The SPP exhibits a plasma-like behavior inside the metal, while it simultaneously resembles a free EM wave inside the dielectric. One key aspect is that the SPPs are excited by the propagating EM wave only if they exhibit the same frequency and momentum. However, for a given frequency, a photon has a different momentum than a plasmon polariton, because they show different dispersion relations. As a direct result of this momentum mismatch, the freely-propagating light does not immediately interact with the SPP at the metal-dielectric interface. In order to overcome this issue, several techniques have been proposed, such as the coupling of the EM wave by means of prisms or sub-wavelength periodic structures, so that it is possible to boost the interaction.

Regarding the first approach, i.e. that involving the use of prisms, we can find two well-known configurations for the excitation of SPPs, namely the Kretschmann [172] and the Otto [173] configurations. Schematics of these coupling configurations are shown in Figure 3.1. More specifically, in the configuration proposed by Kretschmann *et al.*, the sketch of which is illustrated in Figure 3.1(a), a metal film is evaporated onto a glass block, typically a prism. The incident light illuminates the prism and then the evanescent wave penetrates through the metal film. The SPPs are excited at the outer side of the metal film. On the other hand, in the scheme proposed by Otto *et al.*, the sketch of which is illustrated in Figure 3.1(b), a thin metal film is placed close enough to the wall of the prism. As the incident light illuminates the edge of the prism, the evanescent wave interacts with the plasma waves on the metal surface closer to the prism wall, thus exciting the SPPs.

In order to gain a deeper insight about the dynamic of the SPR, in Figure 3.2 we show a sketch of the propagation of an SPP at the interface between a metal and a dielectric. From here, we can observe that the amplitude of the EM field related to the SPPs is maximum at the interface and then decays in both media, following an exponential trend with different decay rates. These rates are ultimately determined by the dielectric permittivity of the dielectric and metal, ε_d and ε_m, respectively, as follows [45]:

$$\delta_m = \frac{\lambda}{2\pi}\sqrt{\left|\frac{\varepsilon_m + \varepsilon_d}{\varepsilon_m^2}\right|} \tag{3.1}$$

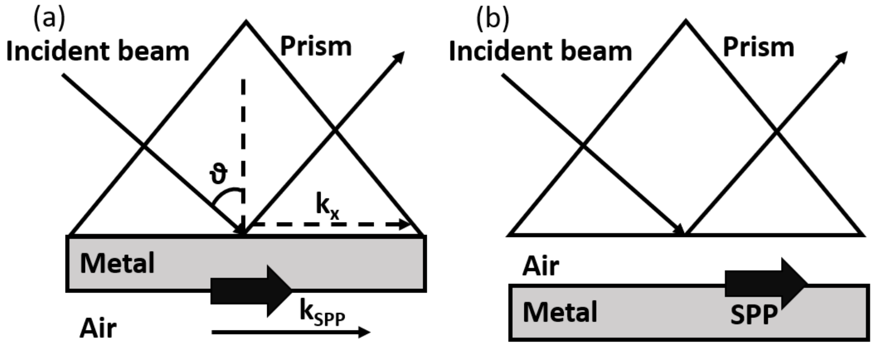

Figure 3.1. Schematics of the (a) Kretschmann and (b) Otto configurations for the excitation and coupling of Surface Plasmon Polaritons (SPPs) at optical frequencies. In (a), a metal film is evaporated onto a glass block, typically a prism. The light illuminates the prism and then the evanescent wave penetrates in the metal film. The SPPs are excited at the outer side of the metal film. In (b), the light illuminates the edge of a prism, being totally reflected within it. A thin metal film is placed close to the bottom prism wall, so that the evanescent wave eventually interacts with the plasma waves on the metal surface, thus exciting the SPPs.

$$\delta_d = \frac{\lambda}{2\pi}\sqrt{\left|\frac{\varepsilon_m + \varepsilon_d}{\varepsilon_d^2}\right|} \tag{3.2}$$

From Equations (3.1) and (3.2), we can observe that the SPP decay length is much shorter inside metals, while it tends to be much larger in dielectrics, since the dielectric permittivity of dielectric materials is usually much smaller than that of metals, i.e. $\varepsilon_d \ll \varepsilon_m$. At the very early stages of research in this field, the investigation of SPPs was mostly focused in the visible and IR spectral regions, where noble metals were employed for this task [174,175]. The dielectric permittivity of metals can be retrieved via the Drude model, and it is related to the metal plasma frequency, ω_p, as follows [45]:

$$\varepsilon_m(\omega) = \varepsilon_l - \frac{\omega_p^2}{\omega^2 + i\Gamma\omega} \tag{3.3}$$

where

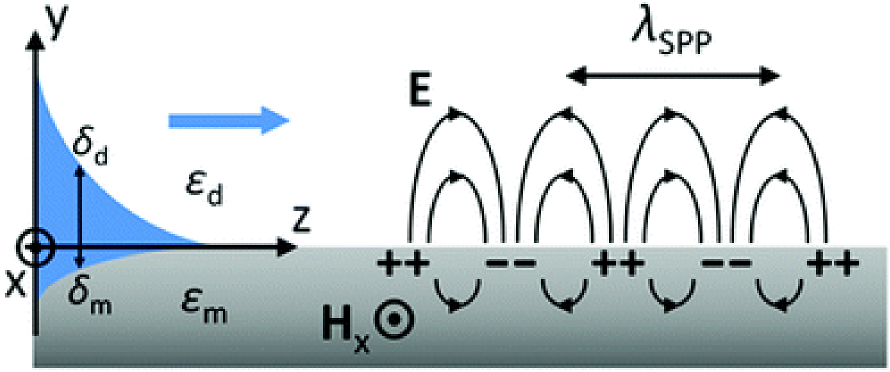

Figure 3.2. Schematic illustration of the propagation of surface plasmon polaritons (SPPs) at the interface between a metal and a dielectric, and of its field components. The surface wave shows a Transverse Magnetic (TM) fundamental mode, thus featuring electric field components normal to the interface (y-axis) and parallel to the field propagation direction (z-axis). The blue shaded area represents the magnitude of the corresponding magnetic field, which is oriented along the x-axis, together with the decay lengths in both media, i.e. δ_d for the dielectric and δ_m for the metal. The figure is adapted from Ref. [174].

$$\omega_p = \sqrt{\frac{Ne^2}{m\varepsilon_0}} \quad ; \quad \Gamma = \frac{1}{\tau_s} = \frac{e}{m^*\mu} \tag{3.4}$$

In Equation (3.3), ε_l is the contribution of the bound charges to the permittivity, while the parameter Γ, defined in Eq. (3.4), represents the scattering rate of the free charge carriers, which corresponds to the inverse of the mean free time between carrier collisions, τ_s. In Equation (3.4), e is the elementary charge, N the free charge carrier concentration, ε_0 the vacuum dielectric permittivity, while m^* and μ are the effective mass and mobility of the free charge carriers, respectively. It is worth recalling that, generally speaking, the dielectric permittivity for both metals and dielectrics is complex-valued, i.e. $\varepsilon = \varepsilon_r + i\varepsilon_i$, with ε_r and ε_i being its real and imaginary part, respectively. Specifically, the real part is related to the strength of the polarization induced by an external electric field, while the imaginary one is related to the absorption and scattering losses experienced by an EM wave as it interacts with a material [45]. Since the plasma frequency of metals typically falls in either the visible or ultra-violet (UV) regions of the EM spectrum (~ 10^{14}-10^{15} Hz), their dielectric permittivity becomes very small at these frequencies, thus implying a significant enhancement of the coupling between the freely propagating light and the free charge carriers. For several years, it has not been very clear whether SPPs actually exist at lower frequencies, such as in the THz domain. In order to better explain the reason, let us consider the expression of the in-plane wave-vector, alternatively defined as momentum of SPPs:

$$k_x(\omega) = k_x'(\omega) + ik_x''(\omega) = k_0(\omega)\sqrt{\frac{\varepsilon_m(\omega)\varepsilon_d(\omega)}{\varepsilon_m(\omega) + \varepsilon_d(\omega)}} \tag{3.5}$$

Here, k_0 is the wave-vector of the EM wave propagating in free space, while k_x is that in the plane along which the SPPs propagate, i.e. at the metal-dielectric interface, with k_x' and k_x'' being its real and imaginary part, respectively. Both the free-space wave-vector and the SPP momentum are function of the angular frequency, ω [166]. Both at THz and optical frequencies, the relative dielectric permittivity of dielectrics is much smaller than that of metals, so that the latter play a more significant role in the excitation of SPPs. Nonetheless, at THz frequencies, the dielectric permittivity of metals is much larger than that at optical frequencies (of about two orders of magnitude), as it can also be inferred from Eq. (3.3). Moreover, the penetration depth, or decay rate, of the SPPs in the metal is strongly reduced, as it can be inferred from Eq. (3.1). A direct consequence is that both the real and imaginary part of the SPP momentum, indicated in Eq. (3.5), become smaller, thus resulting in a larger value of the propagation length. This parameter is defined as the distance, along the metal-dielectric interface, after which the intensity of the surface mode decreases by a factor *1/e* [45]. Under a mathematical point of view, it is defined as follows:

$$L_x = \frac{1}{2k_x''} \tag{3.6}$$

Moreover, since the frequencies in the THz domain are much smaller than the plasma frequency of metals, which falls in the UV or visible regions of the EM spectrum, the dispersion curve exhibited by the SPPs is very close to the light line. This is defined as the edge of the light cone, i.e. the range of frequencies for which the EM radiation can propagate in the dielectric material. In more detail, the light line exhibits a dispersion relation given by:

$$k_{light} = k_0 n_d \tag{3.7}$$

Here, n_d is the refractive index of the dielectric material. The fact that the SPP dispersion curve is close in value to the light line results in a poor confinement of the SPP field at the metal-dielectric interface. However, for several applications, a strong confinement of the SPP mode is a key factor. For the accomplishment of this task, two main approaches have been proposed at THz frequencies so far, i.e. the periodic perforation of metal surfaces [176] or the excitation of SPPs on semiconductor surfaces [177]. The overall effect of adopting these approaches is a shift of the metal *effective* plasma frequency towards lower values. This implies a reduction of the metal dielectric permittivity and, therefore, a stronger confinement of the SPP field at the metal-dielectric interface, because the surface modes can penetrate deeper in the metal. The surface modes generated at THz frequencies by following one of these two approaches feature dispersion relations very close to those of the SPPs in the optical domain, hence they have been named "spoof" surface plasmon polaritons (SSPPs) [176]. The occurrence of SSPPs at THz frequencies by means of structured surfaces has been first investigated and demonstrated in thin meshes of metallic wires [178,179], and then extended to infinitely thick perfect conductors perforated with arrays of sub-wavelength holes [176]. The perforation of the metal structure allows for the SPP field to penetrate deeper in the effective medium defined by the holes on the metal surface. This approach has been widely adopted for the implementation of a large variety of devices in the THz domain, such as transmission lines [180], dipole antenna detectors [181], optoelectronic devices [182], and many others [183,184].

A crucial difference between SPPs and SSPPs concerns their resonance frequency. On the one hand, the SPP frequency (at optical frequencies) depends on the material properties, such as the material dielectric permittivity. On the other hand, the SSPP frequency (at THz or lower frequencies) shows a dependence on the geometrical parameters of the fabricated grooves, which can be exploited, for instance, for the implementation of band-rejection filters in the frequency domain at THz frequencies. In the following notes, we show that by properly choosing the values for the trench geometrical parameters, it is possible to control the number of resonances induced in the device spectral response, as well as their fundamental properties, such as the frequency position, strength and linewidth. Before doing so, we provide a background on the THz generation and detection techniques employed for the experimental characterization of the fabricated samples reported and discussed in this chapter, i.e. the generation via photoconductive antennas (PCAs) and the detection via free-space electro-optic sampling (FS-EOS), respectively.

3.1.2. TERAHERTZ GENERATION VIA PHOTOCONDUCTIVE ANTENNAS

Photoconductive antennas (PCAs) have been one of the most frequently employed components for both the generation and detection of THz pulses [2]. Usually, a PCA consists of two metal electrodes deposited on a semiconductor substrate, with a micron-sized gap between them. Such a configuration of the metal electrodes is typically referred to as dipole configuration [2]. In order to generate THz pulses, a bias voltage is applied across the metal electrodes [35]. Since the material making up the PCA substrate is semi-insulating, under dark condition, i.e. in the absence of illumination, the electric energy is stored in the gap between the two electrodes. A schematic of the PCA is shown in Figure 3.3(a). As a laser optical pulse, with a temporal duration in the sub-picosecond scale, is focused into the gap between the two electrodes, it triggers an ultrashort photocurrent transient, which is drifted by the bias voltage. As a result of this mechanism, there is a release of the electric energy, previously stored in the gap, in the form of THz pulses, which are emitted from the gap volume. The polarization of the emitted THz pulses is parallel to that of the bias electric field, which in turn is perpendicular to the orientation of the metal electrodes. For the generation of photo-induced free carriers in the substrate, the incident photon energy must be larger than the band gap energy of the semiconductor employed for the PCA, i.e. $h\nu > E_g$, where h is the Planck constant, ν is the frequency, and E_g is the semiconductor band gap energy. If this condition is satisfied, the electrons can be excited from the valence to the conduction band [1,36]. In this case, the free carriers are driven by the bias electric field across the gap, thus generating a photocurrent. Since electrons usually exhibit a much higher mobility than holes, the latter provide a negligible contribution to the total photocurrent, with respect to the electrons [45]. Therefore, the current density can be expressed as follows:

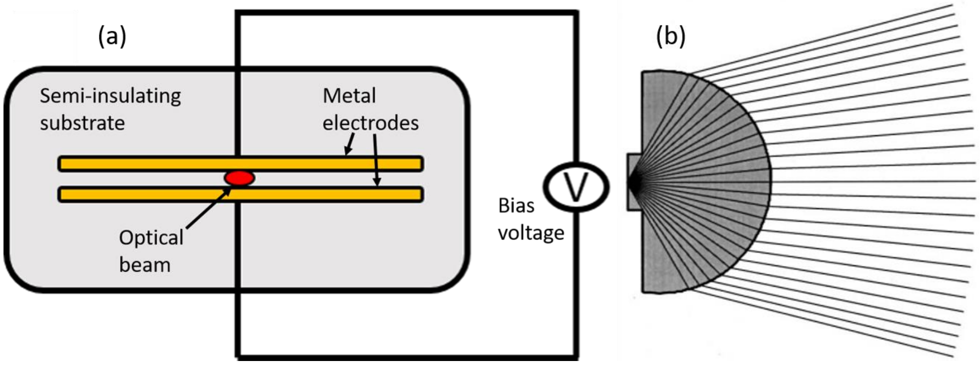

Figure 3.3. (a) Schematic of the structure of a photoconductive antenna (PCA). The laser beam (red spot) is focused on the gap between the two metal electrodes (orange stripes), in what is known as a dipole configuration. The electrodes are fabricated on top of a semi-insulating substrate. For the generation of THz pulses, a bias voltage, V_{bias}, is applied to the metal electrodes. The polarization of the emitted pulses is parallel to that of the applied bias electric field. (b) Sketch of the working principle of a hyper-hemispherical lens. The beam emitted by the PCA is partially collimated by the lens, resulting in a significant decrease of the emission angle, which would be otherwise too large. Figure (b) is adapted from Ref. [2].

$$J(t) = N(t)e\mu E_b \tag{3.8}$$

In Equation (3.8), N is the density of photocarriers, e is the elementary charge, μ is the mobility of the electrons, and E_b is the bias electric field applied to the metal electrodes of the PCA. As one can infer from Eq. (3.8), the photocarrier density, N, is time-dependent, and is determined by both the laser pulse shape and the carrier lifetime of the charge carriers in the substrate material. The immediate consequence of the photocurrent being time-dependent is that it generates an EM pulse, the electric field of which can be estimated as follows:

$$E_{THz}(t) = \frac{1}{4\pi\varepsilon_0}\frac{A}{c^2 z}\frac{\partial J(t)}{\partial t} = \frac{Ae\mu E_b}{4\pi\varepsilon_0 c^2 z}\frac{\partial N(t)}{\partial t} \tag{3.9}$$

Here, A is the active area of the PCA, i.e. the gap area illuminated by the incident laser beam, ε_0 is the vacuum dielectric permittivity, c is the speed of light in vacuum, and z is the propagation direction of the emitted THz beam. The higher the number of photocarriers, the larger the fraction of energy in the gap converted into THz power. The performance of a PCA mainly depends on several factors, such as the material chosen for the substrate, geometry of both the active area and the antenna, as well as the excitation laser pulse [1]. Typical materials employed for the PCA substrate are those exhibiting a short carrier lifetime, such as Low-Temperature-Grown GaAs (LTG-GaAs), so that the response of the PCA can be decreased [36]. A significantly short carrier lifetime is a crucial aspect for both the generation and detection of particularly short THz pulses, i.e. exhibiting a very short temporal duration. Another desired feature for the substrate material is a high carrier mobility, because it leads to a high THz generation efficiency.

The photocurrent of a PCA is located just below the interface between the substrate and the metal electrodes. The portion of THz power directly radiating into the substrate material is usually stronger than that in free space, by a factor that depends on the dielectric permittivity of the substrate material. For instance, the relative dielectric permittivity of LTG-GaAs is ~ 12, so that a major portion of the THz radiation is not actually emitted in air, rather in the opposite direction, i.e. towards the substrate. Additionally, the radiation emitted by a PCA would be highly divergent, because of the gap size (between the electrodes) being much smaller than the central wavelength of the generated THz beam (sub-wavelength). This would result in a very large impedance mismatch between substrate and air, as well as in a large emission angle, which would not allow for the collection of the whole beam emitted by the PCA. Therefore, a hyper-hemispherical lens, a sketch of which is shown in Figure 3.3(b), is usually attached to the backside of the PCA [2]. By doing so, the divergence angle of the emitted THz radiation is significantly decreased (down to ~ 17°), resulting as well in a much larger fraction of the THz power being coupled in air. The material of choice for the hyper-hemispherical lens is silicon, since its refractive index (~ 3.4) [2] matches well with that of the semiconductors commonly employed for the PCA substrate.

3.1.3. TERAHERTZ DETECTION VIA FREE-SPACE ELECTRO-OPTIC SAMPLING

The phenomenon behind the working principle of FS-EOS is the Pockels effect in electro-optic (EO) crystals [1]. Briefly, the Pockels effect causes a change in the refractive index, in an optical medium, which is induced by an external electric field [114]. The change in the refractive index is proportional to the strength of the applied electric field. This effect can be defined by the following relationship for the polarization vector [114]:

$$P_i^2(\omega) = 2\sum_{j,k} \varepsilon_0 \chi_{i,j,k}^2(\omega,\omega,0) E_j(\omega) E_k(0) \tag{3.10}$$

Here, $\chi_{i,j,k}^2$ is the field-induced susceptibility tensor, of the second-order, with ω being the angular frequency. Equation (3.10) implies that a static electric field induces a birefringence, in a second-order nonlinear medium, proportional to its strength. Ideally, as the group velocity of the optical beam matches with the phase velocity of the THz pulse in an EO crystal, i.e. $v_{g,opt} = v_{ph,THz}$, the optical pulse interacts with a static electric field associated to the THz pulse. This is because the frequency of the THz pulse is much smaller than the fast oscillations associated to the electric field of the optical pulse.

As the linearly-polarized optical and THz pulses collinearly propagate through the EO crystal, the birefringence induced by the THz field results in a slightly elliptical polarization of the optical beam, which is then split into two components by a Wollaston prism and sent to a balanced photodetector. A sketch illustrating the whole process is shown in Figure 3.4. In particular, in Figure 3.4(a) we illustrate the main components allowing to perform the FS-EOS, while in Figure 3.4(b) we show the evolution of the optical probe beam polarization as it travels from the EO crystal to the balanced photodetector, in the cases where a THz beam is focused on the EO crystal (bottom plot) and where it is not (upper plot). The balanced photodetector measures the difference between the intensities of the two components of the optical beam. This intensity difference is, at a first approximation, proportional to the applied THz electric field amplitude. Moreover, the differential phase delay, $\Delta\phi$, experienced by the two components of the optical probe beam is given by the following relationship [114]:

$$\Delta\phi = \frac{\omega L}{c} n_O^3 r_{41} E_{THz} \tag{3.11}$$

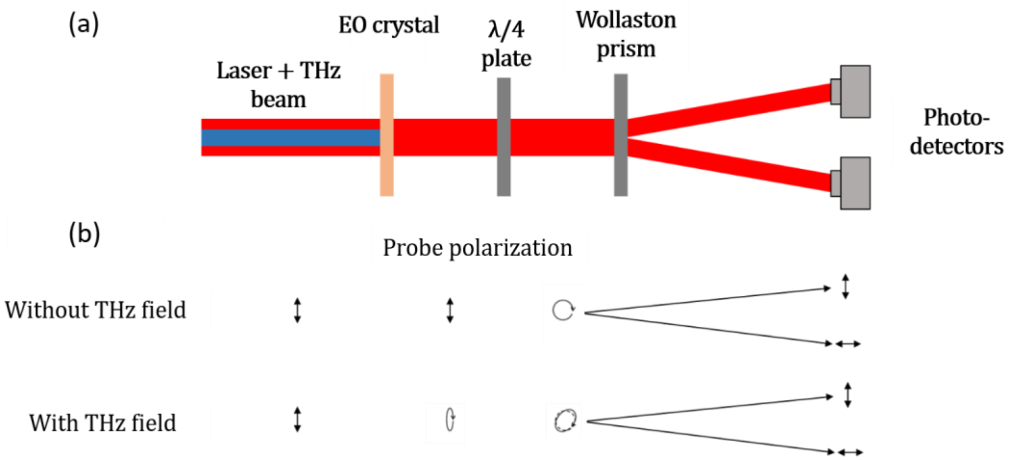

Figure 3.4. (a) Schematic of the detection part of a setup carrying out the free-space electro-optic sampling (FS-EOS) method in the THz domain. (b) Evolution of the optical probe beam polarization, with and without a THz beam focused on the electro-optic (EO) crystal, as it propagates from the crystal to the balanced photodetector, through the quarter-wave plate and the Wollaston prism. Figure (b) is adapted from Ref. [2].

Here, n_O is the refractive index of the material making up the EO crystal at the optical frequency, and E_{THz} is the amplitude of the measured THz electric field. The intensities of the two probe beams, measured by the balanced photodetector, can be expressed as follows [2]:

$$\begin{cases} \mathrm{I_x} = \frac{I_0}{2}(1-\sin(\Delta\phi)) \approx \frac{I_0}{2}(1-\Delta\phi) \\ I_y = \frac{I_0}{2}(1+\sin(\Delta\phi)) \approx \frac{I_0}{2}(1+\Delta\phi) \end{cases} \tag{3.12}$$

Here, I_0 is the intensity of the incident probe beam, and the differential phase delay, $\Delta\phi$, is assumed to be smaller than 1. Finally, the balanced photodetector determines the THz field amplitude as the difference between the intensities of the two components in Eq. (3.12), i.e.:

$$\mathrm{I_s} = I_x - I_y = I_0\Delta\phi = \frac{I_0\omega L}{c} n_O^3 r_{41} E_{THz} \tag{3.13}$$

In a realistic situation, the temporal resolution of the FS-EOS technique is limited by three factors: the finite pulse duration of the optical probe, the dispersion of the nonlinear susceptibility, and the mismatch between the optical group velocity and the THz phase velocity.

The detection sensitivity increases with the crystal thickness, *L*, yet at the expenses of a shrinkage in the detected bandwidth, because of the phase mismatch.

3.2. DESIGN OF TERAHERTZ BAND-REJECTION FILTERS VIA TRENCH FABRICATION ON A BARE COPPER WIRE

As mentioned before, band-rejection frequency filters have already been proposed and demonstrated at THz frequencies by following several approaches, such as the design of specific metasurfaces [138,183], the insertion of materials in the air gap of a TWWG [123,129] or by properly processing the surface of metal plates in a TPPWG [74,76]. In particular, the engineering of a metallic surface seems to be the most promising approach, which results in the occurrence of several resonances across the whole THz spectrum. The properties of these so-induced resonances, such as frequency position, strength, and linewidth, are strongly dependent on the groove geometrical parameters [45]. In what follows, we show that, by choosing a suitable set of values for the geometrical parameters of the fabricated trenches, it is possible to control the number of resonances induced in the spectral response. In particular, the main goal is to achieve a configuration whereby only one resonance is induced across the spectral transfer function, i.e. the SSPP fundamental mode. Also, for the design and implementation of the structure, we employ the TWWG configuration, because of the aforementioned advantages over other metal-based waveguides (see Section 2.2.2.1). Furthermore, it is worth pointing out that all the results (both theoretical and experimental) reported and discussed in this chapter, refer to the fabrication of trenches on just one of the copper wires forming the TWWG. As a matter of fact, in the case where both wires would feature trenches on their surfaces, one would have to guarantee, at the same time, a perfect overlap between the starting and ending point of the structure, but also, they would have to perfectly face each other. If these conditions are not satisfied, undesired effects might occur in the spectral response of the investigated device, such as the occurrence of spurious resonances, or the modification of the resonance properties, such as a different resonance strength and/or linewidth, or a change in its frequency position. For a deeper insight on the trenches geometrical parameters that play a role in the definition of the

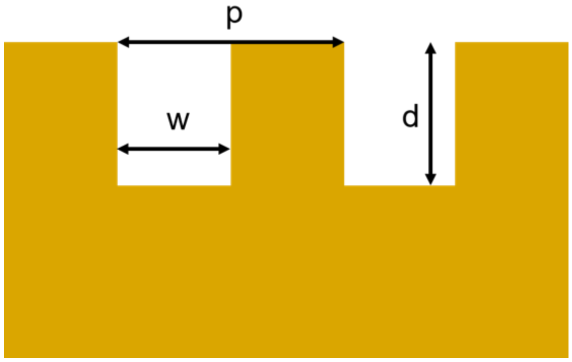

Figure 3.5. Cross-section of a copper wire that exhibits the trenches fabricated on its surface. Here, we show the main geometrical parameters of the fabricated trenches that influence the spectral response of the frequency filter, i.e. the trench depth (*d*), the trench width (*w*), and the grating period (*p*).

SSPP resonance properties, in Figure 3.5 we show a cross-section of the trenches fabricated on the surface of the copper wire. In particular, these parameters are the following: the trench depth (*d*), the trench width (*w*), and the grating period (*p*). Considering the number of geometrical parameters involved, we performed a parametric study. This study was performed by varying the value of one of the parameters per time, while keeping the other ones fixed. In this way, it was possible to better analyze the effect of the individual geometrical parameters on the spectral response. Moreover, this numerical investigation allowed us to choose a suitable set of values, for the geometrical parameters, for which only one SSPP resonance is induced across the whole spectral transfer function.

All the numerical investigations reported and discussed in this section were performed by employing a simulation software that exploits the Finite-Difference in the Time-Domain (FDTD) algorithm [185]. This algorithm enabled the solving of the Maxwell's equations describing the EM wave propagation within the structure, thus allowing us to retrieve the temporal waveform of the THz electric field at the targeted position inside the waveguide-embedded component, e.g. its input or output. Each of the theoretical studies was performed as follows. First, we simulated the propagation of a THz beam focused at the input of a standard TWWG, i.e. two bare copper wires, and retrieved the temporal profile of the THz electric field at its output. Subsequently, we simulated the propagation of the same input THz pulse within a TWWG where one of the copper wires carries the trenches, retrieving the temporal waveform at its output. For all the theoretical investigations, we considered the copper as a perfect electric conductor (PEC), due to the fact that the behavior of this metal at THz frequencies is very close to the ideal case. Moreover, this approximation allowed us to use a significantly reduced amount of physical memory for a pseudo-3D simulation, in contrast to the case of a real lossy metal. As a matter of fact, if we were to use the real material, then the size of the mesh cells in the simulation region, which are necessary for the retrieval of the information corresponding to the THz pulse propagation within the investigated structure, would have to set to be very small values, i.e. $\Delta x < \frac{\lambda_0}{\sqrt{\varepsilon_{copper}}}$, with Δx being the size of the mesh cell. In particular, this would have to be set to values in the nanometer scale, in order to achieve accurate results, thus resulting in a too large amount of required physical memory. We note that this kind of approximation is not valid for other structures, such as the SWWG, since in that case the propagation of the THz pulse is explained in terms of the electric field penetrating the metal by its skin depth (Sommerfeld mode). However, a PEC does not allow the electric field to penetrate its surface, since its electrical conductivity, σ, is ideally infinitive and could not sustain the propagation of a THz pulse in an ideal scenario. As such, the PEC model cannot be applied to the case of an SWWG. This represents another valuable advantage of the TWWG against non-symmetric waveguide geometries, such as SWWGs and HCWGs. Once both the temporal waveforms were retrieved, we computed the corresponding spectra via a Fast Fourier Transform (FFT) algorithm and, finally, evaluated the transfer function as follows:

$$T(f) = \frac{E_{grating}(f)}{E_{TWWG}(f)} \tag{3.14}$$

Here, $E_{grating}(f)$ is the FFT-evaluated spectrum corresponding to the temporal waveform retrieved after the propagation in the grating structure, and $E_{TWWG}(f)$ is that corresponding to the temporal waveform retrieved after the propagation in a plain TWWG, i.e. two bare copper wires. As far as the input THz source employed for the numerical investigation is concerned, we considered a THz beam exhibiting a spatial Gaussian profile with a waist radius of 600 μm, a central frequency of f_c = 0.7 THz and a bandwidth of B_W ~ 2 THz. The temporal waveform and the FFT-evaluated field spectrum of the THz impulse used as input in the numerical

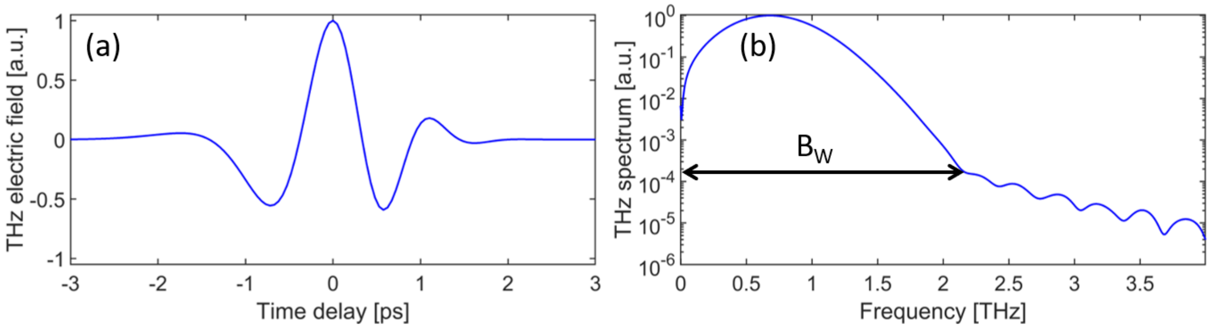

Figure 3.6. Temporal profile of the THz electric field (a) and corresponding FFT-evaluated spectrum (b), of the THz pulse employed as input source in the numerical investigation of the designed structure via Finite Difference in the Time Domain (FDTD) algorithm. The central frequency of the employed pulse is f_c ~ 0,7 THz, while its full bandwidth, i.e. the full width up to the noise floor, is B_W ~ 2 THz, as also indicated by the black arrow in (b). All the curves are normalized to their own maxima.

Wire interspacing [μm]	Trench width [μm]	Grating period [μm]	Number of trenches
800	100	200	20

Table 3.1. Initial set of values chosen for the trenches' geometrical parameters for the numerical investigation of the THz band-rejection filter functionality, achieved by etching an array of periodic trenches on the surface of a bare copper wire.

investigation are shown in Figure 3.6(a) and (b), respectively. Here, B_W refers to the full width of the THz spectrum, i.e. up to the noise floor level, as also highlighted in Figure 3.6(b), where this parameter is represented with a black arrow indicating its extension.

3.2.1. INVESTIGATION ON THE TRENCH DEPTH

We started the numerical investigation by studying the effect of changing the value of trench depth, d, on the grating spectral transfer function, $T(f)$. For the purposes of the numerical investigation, we chose an initial set of values for the trenches fabricated on the copper wire. These values are listed in Table 3.1. Note that the value of the wire radius was set at R = 127 μm. For the investigation of the trench depth, we varied its value from 10 to 200 μm, with a step of 5 μm. For each investigated value, we retrieved the spectral transfer function, as indicated in Eq. (3.14). In order to gain a deeper understanding on the way a change in the trench depth affects the spectral response of the grating, we plot all the transfer functions, corresponding to

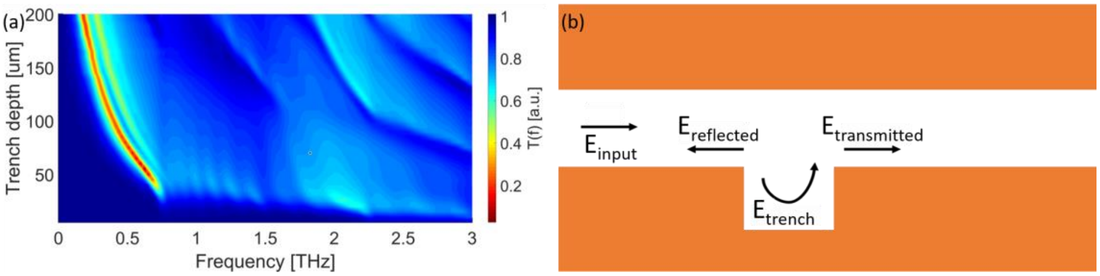

Figure 3.7. (a) Two-dimensional map, retrieved in the frequency domain, displaying the spectral transfer function, calculated as indicated in Eq. (3.14), of the investigated structure. Here, the trench depth value, d, is varied from 10 to 200 μm, with a step of 5 μm. The color bar on the right side indicates the values exhibited by the spectral transfer function. (b) Dynamic of the propagation of the waveguide fundamental mode in the region close to the trenches fabricated on the wire surface. As it reaches the left edge of the first trench, it separates into three components: that reflected back towards the TWWG input ($E_{reflected}$), that transmitted through the air gap ($E_{transmitted}$), and that trapped within the trench (E_{trench}). The last two components exhibit a π radians phase delay at the frequency corresponding to the spoof SPP (SSPP) fundamental mode.

each of the investigated trench depth values, in a two-dimensional color map, which is shown in Figure 3.7(a). In this plot, the frequency, f, is plotted on the x-axis and the trench depth, d, on the y-axis. The first aspect that can be observed from the plot is that, for a rather shallow trench on the wire surface, i.e. $d < 30$ μm, the trenches do not exhibit a significant influence on the device spectral response. Indeed, for this range of values, the device spectral transfer function is quite smooth and exhibits a lack of resonances. However, as the trench depth is increased, i.e. $d > 30$ μm, we can observe a resonance occurring at frequencies below 1 THz. Moreover, the frequency position of such a resonance shows an inverse proportionality to the trench depth, d. Let us examine in more detail such a resonance. As reported in Ref. [76], this surface mode is commonly referred to as the fundamental mode of the perforated structure. In more detail, this resonance has to be ascribed to a π radians phase delay between the THz electric field component (associated to the waveguide fundamental mode) propagating through the air gap, in the region close to the trenches, and that trapped inside the trench. To better understand this point, let us take into consideration the propagation of the waveguide fundamental mode inside the structure. To this end, in Figure 3.7(b) we show a sketch of the dynamic within the TWWG.

As the waveguide fundamental mode reaches the left edge of the first trench, it is split into three components:

- The component that is transmitted through the air gap and travels towards the TWWG output ($E_{transmitted}$);
- The component that is reflected at the left edge of the trench and travels back towards the TWWG input ($E_{reflected}$);
- The component that is trapped inside the trench on the wire surface (E_{trench}).

In particular, the last component travels down to the bottom end of the trench and is then reflected. Subsequently, it propagates towards the right edge of the trench, where it is split again in the same fashion. After propagation through the first trench, this THz field component keeps traveling towards the second trench, together with the component of the THz field initially propagating through the air gap ($E_{transmitted}$). Therefore, there is a difference in the length of the optical paths followed by the two field components, which results in a phase delay between them. The phase delay is directly proportional to the trench depth value, d, and depends as well on the wavelength. In particular, this can be expressed as follows:

$$\Delta\varphi \propto k\Delta l = \frac{2\pi\Delta l}{\lambda} = \frac{2\pi\Delta l}{\lambda_0} n_{eff}(d) = \frac{2\pi\Delta l f_0}{c} n_{eff}(d) \tag{3.15}$$

Here, k is the THz field wave-vector, λ is the wavelength of the field propagating within the TWWG, λ_0 and f_0 are the wavelength and frequency in vacuum, c is the speed of light in vacuum, Δl is the difference in the optical path lengths of the two field components, i.e. $E_{transmitted}$ and E_{trench}, which is equal to twice the trench depth, d. Moreover, $n_{eff}(d)$ is the effective refractive index of the mode propagating within the TWWG in the region where the trench is fabricated. This effective refractive index shows a dependence on the trench depth, so that it changes for each study case. The frequency for which $\Delta\varphi = \pi$ is indeed the SSPP mode. This leads to an out-of-phase condition between the two components, which in turn results in a gradual disappearance of the THz electric field while moving towards the TWWG output. Such a dynamic is represented in Figure 3.8(a), where we show the THz electric field intensity distribution in the section of the TWWG where the trenches are fabricated. The field distribution

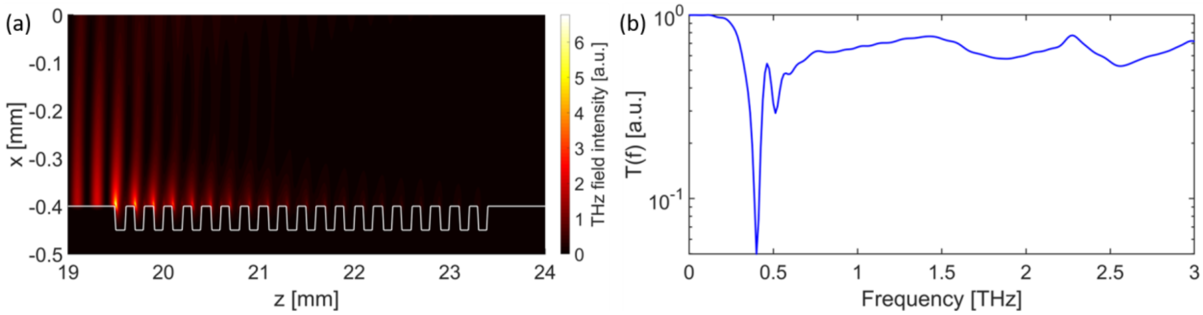

Figure 3.8. (a) THz electric field intensity distribution in the simulated structure, where the trench depth is $d = 50$ µm, and the other geometrical parameters values are fixed to those listed in Table 3.1. The field distribution is evaluated at the corresponding frequency of the SSPP mode, i.e. $f_{SSPP} \sim 0.65$ THz. Note how the THz field intensity is gradually decreasing while propagating from the TWWG input to its output. (b) Transfer function, *T(f)*, evaluated as indicated in Eq. (3.14), for a trench depth of $d = 100$ µm. We can observe the presence of the SSPP fundamental mode at around 0.4 THz, and of a high-order SSPP mode at around 0.5 THz.

has been evaluated for the case where the trench depth value of $d = 50$ µm, and at the frequency corresponding to the SSPP mode, i.e. ~ 0.65 THz. From here, we can observe that the propagation of the SSPP causes a gradual decrease in the THz field intensity while propagating towards the device output, while at the same time inducing an enhancement of the field at the left edge of the first trench. These simulations also demonstrate that the SSPP mode frequency decreases as the trench depth value is increased. The reason behind this behavior can be inferred from Eq. (3.15), from which we can observe that the condition to achieve the out-of-phase condition is obtained at even-lower frequencies, as the trench depth (and, accordingly, the difference between the optical paths of the two field components) becomes larger.

Additionally, a second resonance can be observed in the 2D colormap shown in Figure 3.7(a), as $d > 50$ µm. The origin of such a resonance has been thoroughly investigated in Ref. [186], and it is attributed to the fact that, as the trench depth value is increased and becomes closer to that of the trench width (w), the structure supports the propagation of high-order SSPP modes. On one hand, the fundamental SSPP mode does not show any cut-off frequency on any metal surface (planar or cylindrical), as reported in Refs [187,188]. On the other hand, high-order SSPP modes do exhibit cut-off frequencies, occurring only when certain conditions are satisfied. In this particular case, the occurrence of the high-order SSPP modes, as well as their number, seems to be directly related to the relationship between the trench depth and width, as reported in Ref. [186]. Furthermore, the frequency position of the high-order SSPP mode seems to follow a trend similar to that of the SSPP fundamental mode, i.e. decreasing as the trench depth is increased, as also indicated in Eq. (3.15). As an example, in Figure 3.8(b) we show the simulated transfer function, evaluated as in Eq. (3.14), of a sample where the trench depth is $d = 100$ μm, with the values of the other geometrical parameters fixed to those listed in Table 3.1. We can immediately observe the presence of the SSPP fundamental mode at around 0.4 THz, as well as the second-order SSPP mode being at around 0.5 THz.

Summarizing, since our targeted spectral response has to exhibit only one resonance, i.e. the SSPP fundamental mode, the main goal here is to ensure that no high-order modes are induced in the spectral response. Therefore, a trench depth value of $d > 50$ μm cannot be chosen. On the other hand, a trench depth value of $d < 30$ μm would not induce any SSPP resonance in the spectral response. Therefore, the trench depth value has to be chosen in the range between 30 and 50 μm. Four our case, we chose a value of $d = 50$ μm, since it allows to induce only one SSPP resonance in the spectral response, which also exhibits a large depth.

3.2.2. INVESTIGATION ON THE TRENCH WIDTH

From the previous theoretical study, we determined that a trench depth of $d = 50$ μm is an optimal value, due to the fact that it induces only one SSPP resonance, i.e. the SSPP fundamental mode, across the whole spectral response of the simulated structure. For the second parametric study, we analyzed the effect of another trench geometrical parameter, i.e. the trench width (w) on the device spectral response. For the task, we used the trench depth value found from the previous investigation, and varied the trench width from 5 to 200 μm, with a step of 5 μm, while the values of the grating period and the number of trenches were fixed at those listed in Table 3.1. We point out here that, varying the trench width in a similar fashion, i.e. by keeping the value of the grating period fixed, induced a simultaneous variation of the duty cycle, which is a typical parameter of periodic structures. In our particular case, it is defined as the radio between the trench width, w, and the grating period, p. Furthermore, we anticipate here that varying the trench width does not cause any significant effect the properties of the SSPP

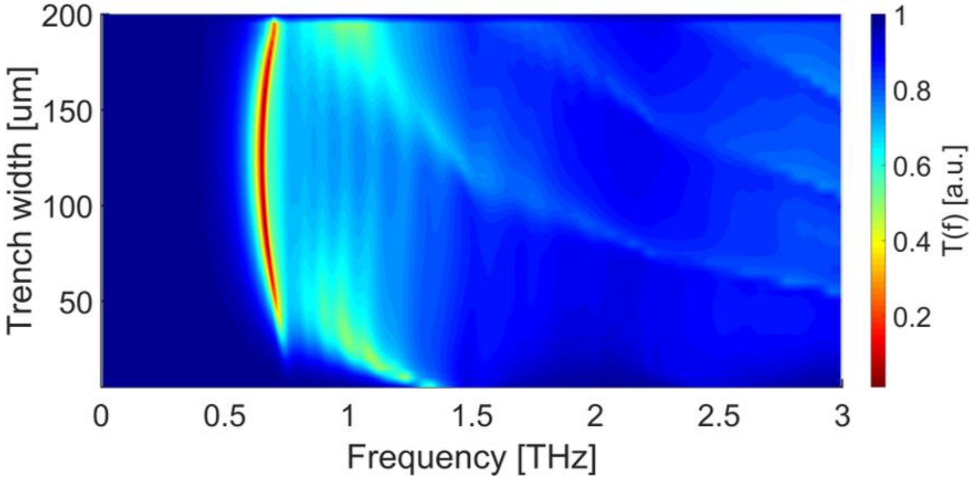

Figure 3.9. Two-dimensional map, retrieved in the frequency domain, illustrating the spectral transfer functions, evaluated as indicated in Eq. (3.14), as the trench width, *w*, is varied from 5 to 200 μm, with a step of 5 μm, while keeping the grating period fixed at the value indicated in Table 3.1. By doing so, also the duty cycle of the periodic structure is varied. The duty cycle is defined as the ratio between the trench width, *w*, and the grating period, *p*. Note how the frequency position of the SSPP fundamental mode is not significantly affected by a change in the trench width value.

fundamental mode, as also reported in literature. As a matter of fact, the effect of varying the trench width has been investigated in Ref. [189], for the case where a metal planar surface exhibits an array of periodic grooves. In this case, it has been demonstrated that only a slight change in the asymptotic frequency, i.e. the maximum frequency at which the specific SSPP mode can propagate, has been observed (in the order of a few GHz).

The results obtained from this numerical investigation are shown in Figure 3.9. In particular, here we plot the two-dimensional map of the simulated transfer functions, as the trench width is varied within the aforementioned range. A first aspect we can notice is that, for narrow trenches, i.e. for $w < 40$ μm, only a weak resonance is produced in the spectral response. This could be attributed to the weaker confinement of the SSPPs to the structure [189]. Additionally, we can observe the presence of a resonance at higher frequencies. This resonance has the same origin as that seen in the previous investigation for depth values of $d > 50$ μm, i.e. it is a high-order SSPP mode. As the trench width is increased to become larger than 40 μm, the SSPP fundamental mode becomes stronger. In this case, as the trench width is changed, we can notice only a slight change in its frequency position, while its strength seems to be unaffected.

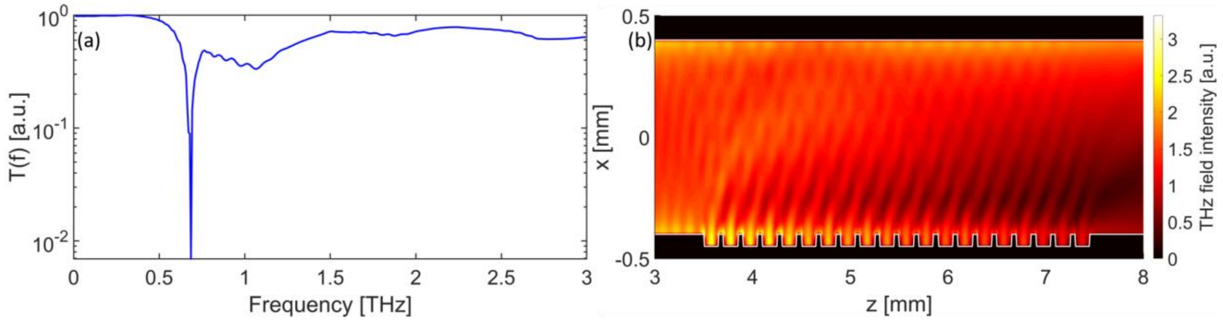

Figure 3.10. (a) Simulated transfer function, evaluated as indicated in Eq. (3.14), for a trench width of *w* = 150 μm. We can observe the presence of the SSPP fundamental mode at f_{SSPP} ~ 0.65 THz, together with a horizontally-localized standing wave (HLSW) at f_{HLSW} ~ 1.1 THz, the frequency position of which is ultimately determined by the trench width value. (b) THz electric field intensity distribution at *f* ~ 1.1 THz, illustrating how the propagating THz field is trapped inside the fabricated trenches, as well as being enhanced in the fabricated cavity.

This is in good agreement with previous reported numerical investigations, performed by employing several structures [186,189]. It has also been reported that a larger trench width value would result in a stronger confinement of the SSPPs [189]. Even though changing the trench width exhibits a weak, if not negligible, influence on the properties of the SSPP fundamental mode, we can also observe, in the 2D map in Figure 3.9, that the high-frequency portion of the spectral response is affected. In particular, for widths in the range between 50 and 150 μm, we can notice the introduction of losses at frequencies between 0.7 and 1.4 THz, which might be ascribed to radiative losses of the THz radiation due to the discontinuity of the trenches. On the other hand, as the trench width is increased beyond 150 μm, another weak resonance is triggered in the device spectral response at *f* ~ 1.1 THz. For a better understanding of the origin of this resonance, in Figure 3.10(a) we plot the transfer function, *T(f)*, evaluated as in Eq. (3.14), of the simulated structure with a trench width of *w* = 150 μm. From this plot, we can observe a weak resonance (~ 3 dB) at around 1.1 THz, which can be ascribed to the presence of a horizontally-localized standing wave (HLSW) within the fabricated trenches [76]. For the sake of completeness, in Figure 3.10(b) we show also the THz electric field intensity distribution in the region close to the trenches, evaluated at *f* = 1.1 THz. From this plot, we can observe that the THz field is confined inside the first few trenches of the structure, giving rise to an enhancement of its intensity. Moreover, as reported in Ref. [76], its frequency position is inversely proportional to the value of the trench width. Such a trend can also be observed in Figure 3.9.

Summarizing, the trench width seems to have a negligible effect on the SSPP fundamental mode, whereas high-order SSPP modes can be observed in the device spectral response for small trench widths, i.e. $w < 40$ μm. On the other hand, HLSWs are induced in the spectral response as their width is increased. In order to avoid the occurrence of multiple resonances in the spectral response, while at the same time obtaining a single and strong resonance, these values cannot be chosen. Finally, we determined that an optimum width value allowing us to obtain the targeted spectral response is $w = 100$ μm.

3.2.3. INVESTIGATION ON THE GRATING PERIOD

The values retrieved so far from the previous numerical investigations involving the trench depth and width, i.e. $d = 50$ μm and $w = 100$ μm, were then used for the third theoretical study. In particular, here we investigated the effect of varying the grating period on the device spectral transfer function. More specifically, we kept the number of periods fixed at 20, and varied the grating period from 110 to 500 μm, with a step of 10 μm. In a similar way to the previous numerical study, varying the grating period while, at the same time, keeping the trench width fixed, implies a simultaneous variation of the duty cycle of the periodic structure. The results obtained from the numerical investigation are shown in Figure 3.11. Here, we display a two-dimensional color map that encloses all the simulated transfer functions as the grating period, p, was varied within the aforementioned range. A first detail that can be observed from this plot is that the frequency position of the SSPP fundamental mode shifts towards lower values as the grating period is increased. This behavior is in total agreement with that of general resonating structures, including both FBGs and SSPPs in different waveguide configurations [189]. Furthermore, from the numerical results we observed that the behavior of the simulated structure changed depending on the grating period value. In other words, for grating periods smaller than 250 μm, the behavior of the structure was in good agreement with that of SSPPs in perforated metal structures. Nevertheless, as the grating period is increased beyond this value, thus becoming comparable in value with the central wavelength of the propagating THz field

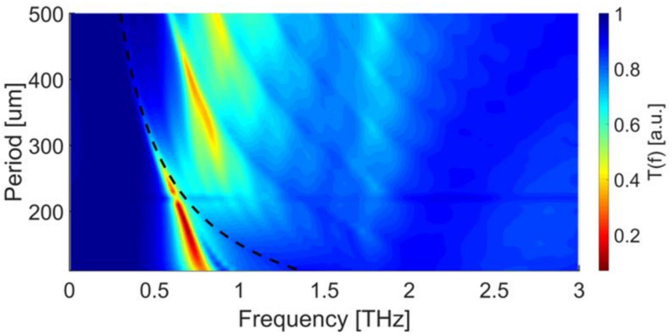

Figure 3.11. Two-dimensional color map, retrieved in the frequency domain, illustrating the simulated spectral transfer functions, as evaluated in Eq. (3.14). Here, the grating period, *p*, is varied from 110 to 500 µm, with the trench width fixed at *w* = 100 µm, thus resulting in a simultaneous variation of the duty cycle of the periodic structure. The black dashed line represents the typical trend of the frequency position of a Bragg resonance, evaluated as in Eq. (3.16), as the grating period is changed. We can observe a good agreement between the black line and the simulated results, for grating periods of *p* > 250 µm.

(λ_c = 500 µm), the structure behavior became very similar to that of a Bragg Grating (BG) structure. This aspect has been investigated in previous works [190,191], where it was demonstrated that, for a grating period much smaller than the central wavelength of the propagating EM wave, the structure can be regarded as an effective medium (as it happens in the case of photonic crystals). On the other hand, as $p \sim \lambda_c$ the structure can be treated as a Bragg-like periodic structure. In this particular case, the frequency position of the resonance induced in the device spectral response, i.e. the Bragg resonance, obeys to a mathematical law that is very similar to that shown in Eq. (2.2). We highlight here that, in the case of trenches fabricated on a metal surface, the effective refractive index (n_{eff}) *seen* by the fundamental mode propagating within the modified TWWG is very close to that of the fundamental mode of a plain TWWG, i.e. ~ 1. This implies that a so-implemented structure causes only a weak perturbation of the THz field propagation constant and, in turn, of its effective refractive index. Therefore, Eq. (2.2) can be simplified as follows:

$$f_{Bragg} = \frac{mc}{2pn_{eff}} \approx \frac{mc}{2p} \tag{3.16}$$

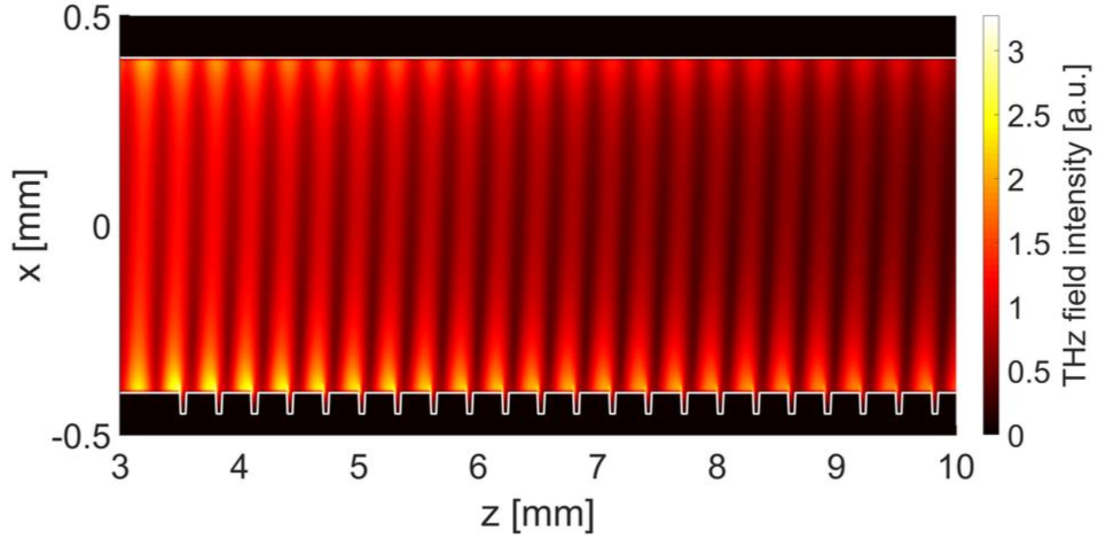

Figure 3.12. THz field intensity distribution in the simulated structure, for the case where the grating period is p = 300 μm. The field distribution is evaluated at the Bragg resonance frequency of the structure, i.e. f_{Bragg} = 0.5 THz. Note that the amplitude of the THz field slowly decreases while moving towards the TWWG output, because of the weak perturbation of the THz field propagation constant induced by the periodic structure.

Here, m is an integer indicating the order of the Bragg resonance, c is the speed of light in vacuum, and p is the period of the structure. In order to qualitatively demonstrate the different behavior of the structure as the grating period is changed, we overlapped the trend corresponding to Eq. (3.16) to the two-dimensional map shown in Figure 3.11, where it is shown as a black dashed line. We can immediately observe that there is a good agreement between the trend of Eq. (3.16) and that followed by the frequency position of the SSPP fundamental mode, at least as the grating period is $p > 250$ μm. On the other hand, as the grating period is $p < 250$ μm, the trend obtained from the numerical investigation strongly deviates from that indicated in Eq. (3.16).

In order to gain a deeper insight about the THz field propagation in such a structure, in Figure 3.12 we illustrate the THz field intensity distribution for the case where the grating period of the structure is p = 300 μm. The field distribution shown in Figure 3.12 was evaluated at the Bragg resonance frequency of the structure, i.e. f_{Bragg} = 0.5 THz. We can notice that there are some significant differences between the field distribution in Figure 3.12 and that of the SSPP fundamental mode shown in Figure 3.8(a). First, the SSPP field is mostly confined at the edges of the first trenches, with the amplitude of the THz field decreasing while propagating towards the TWWG output, with a very short spatial decay rate, as shown in Figure 3.8(a). Conversely, from the field distribution plotted in Figure 3.12 we can observe that the propagating field is mostly trapped in the region between two consecutive trenches, on a wide area. Furthermore, even though the amplitude of the propagating THz field is also decreasing while propagating towards the TWWG output, it does with a slower spatial decay rate. This has to be ascribed to the weaker perturbation of the field propagation constant in the so-implemented structure.

Additionally, another aspect we can notice from Figure 3.11 is that the strength of the Bragg resonance, i.e. its depth, decreases as the grating period, p, is further increased. This might be ascribed to the fact that the larger the period, the weaker the perturbation of the THz field propagation constant, since the distance between two consecutive trenches gradually increase. As discussed in more detail in the following notes, a possible approach to increase the strength of the induced Bragg resonance strength is to significantly increase the number of periods, e.g. from 20 to more than 100. In this way, it is possible to strengthen the perturbation of the field propagation constant, which in turn results in a stronger case, as well as in a narrower resonance linewidth. Finally, high-order Bragg resonances can be observed across the device spectral response, with their frequency position being close to multiples of that of the first-order Bragg resonance.

In conclusion, taking into account the effects of the grating period on the spectral response, a grating period of $p < 250$ μm is an optimal choice for the realization of our device, since a larger value would induce multiple resonances, thus hindering the targeted goal. While this phenomenon may be exploited for other purposes, as discussed in more detail in what follows, for the goal of these numerical investigations, we chose a period of $p = 200$ μm, so that it is possible to trigger a single resonance across the device spectral response, which also exhibits a larger depth.

Summarizing, from the results obtained via the performed numerical investigations, we were able to retrieve an optimal set of values for each of the investigated geometrical parameters. Additionally, we summarize the main results retrieved from each numerical investigation in Table 3.2, where we show the main effects observed in each parametric study, as well as the value chosen for the parameter under study.

Parameter	Main effects	Chosen value
Depth (*d*)	No resonances for shallow trenches ($d < 30$ µm). High-order SSPP modes as $d > w/2$.	50 µm
Width (*w*)	No significant effect on the SSPP fundamental mode. High-order SSPP modes as $w < 2d$. HLSWs triggered for trench width approaching the period value.	100 µm
Period (*p*)	Frequency position shifting towards lower values as *p* is increased. Structure behaves as effective medium as $p << \lambda_{c,THz}$ and as a Bragg Grating for $p \sim \lambda_{c,THz}$	200 µm

Table 3.2. Summary of the main findings from the performed parametric studies via Finite Difference in the Time Domain algorithm, with a brief explanation of the main effects induced by each geometrical parameter on the device spectral response, as well as the value that was chosen for each of them.

3.3. SAMPLE FABRICATION AND CHARACTERIZATION

3.3.1. SAMPLE FABRICATION PROCESS

Once the numerical investigations were performed, with the consequent retrieval of the optimal values for the trench geometrical parameters, we proceeded with the fabrication of the targeted samples. The fabrication process on the bare copper wires was performed at the Laboratory of Micro- and Nanofabrication (LMN) at INRS, Canada. A schematic of the fabrication process is illustrated in Figure 3.13. In more detail, the fabrication process of the samples involved several steps:

1. Etching of a silicon wafer. Multiple grooves were etched on its surface, as shown in Figure 3.13(a), with the goal of hosting the copper wires. In this way, multiple samples could be processed and fabricated at once. The depth of the groove etched on the silicon wafer ultimately determined the depth of the trenches on the copper wire surface.
2. The copper wires were then placed in the grooves etched on the silicon wafer, as displayed in Figure 3.13(b), and kept in tension so to straighten them. In this way, it was possible to guarantee that the trench depth value was relatively uniform along the whole length of the structure. Moreover, by doing so it was also possible to maintain a constant value of the grating period across the whole structure.

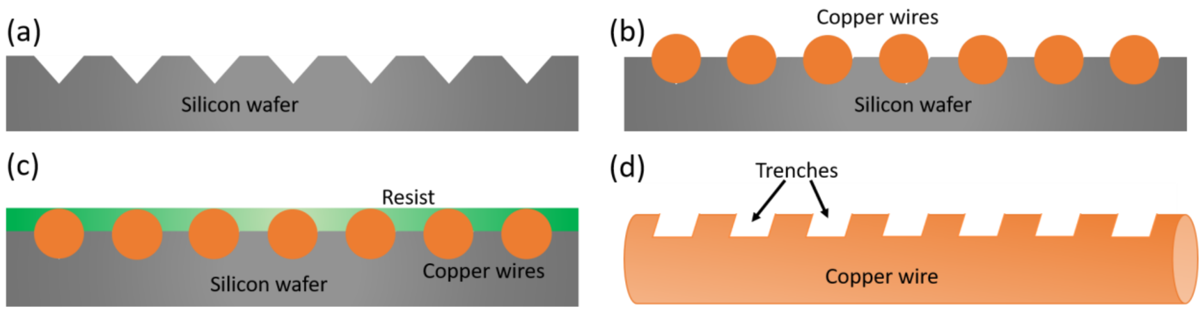

Figure 3.13. Schematic of the fabrication process of the trenches on the copper wire surface. Multiple grooves were etched on the surface of a silicon wafer (a), where the copper wires were then placed (b), after being kept in tension so to straighten them. The depth of the groove etched on the silicon wafer ultimately determined the depth of the trenches on the copper wire surface. A resist material was put on top of the copper wires (c) to avoid any undesired movement of the copper wire, which could affect the uniformity of the structure periodicity. The trenches were then etched on the wires surface by means of a saw equipped with a disc-shaped diamond blade. A sketch of the processed wire is shown in (d).

3. A resist material was then placed on top of the copper wires, as illustrated in Figure 3.13(c), so that it was possible to prevent any possible movement of the copper wires during the fabrication process. In this way, we were able to minimize possible perturbations of the structure periodicity.
4. In order to realize the trenches on the copper wires, a saw was employed, which was equipped with a disc-shaped diamond blade. The blade was available with multiple widths, in the 10-500 μm range, so that samples with different trench widths could be fabricated. The saw was mounted on a micro-machining tool, equipped with a three-dimensional motor control. By employing such a system, it was possible to move the blade in all three directions with a good degree of accuracy. A sketch illustrating the fabricated copper wire is illustrated in Figure 3.13(d).

By following the aforementioned steps of the fabrication process, two different samples have been fabricated, featuring different geometrical parameters. The specifications for each sample are listed in Table 3.3. Furthermore, in Figure 3.14 we show pictures of the sample #1 taken via an optical microscope. In more detail, in Figure 3.14(a) we show a side-view of the sample, while in Figure 3.14(b) we show a top-view of the same sample. Both the images were

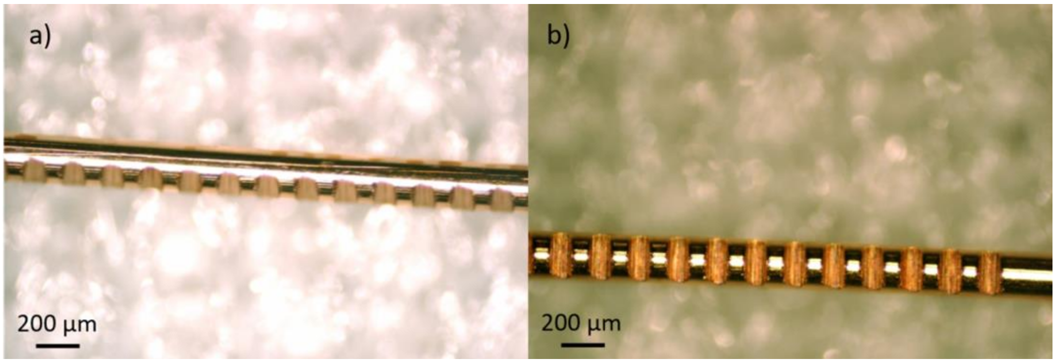

Figure 3.14. Side-view (a) and top-view (b) of Sample #1, taken via an optical microscope. The trench geometrical parameters of the fabricated sample are shown in Table 3.3. In both the pictures, we can observe (at this scale) a good degree of uniformity in the structure periodicity, with no noticeable deviation in the values of both the trench width and depth.

Sample #	Depth [µm]	Air gap [µm]	Width [µm]	Period [µm]	No. of trenches
1	50	800	100	200	20
2	70	800	100	200	20

Table 3.3. Values of the trench geometrical parameters employed for the fabrication of the samples, following the procedure shown in Figure 3.13. The samples were fabricated at the Laboratory of Micro- and Nanofabrication (LMN) in Canada.

taken via an optical microscope. The sample illustrated in the pictures exhibits a good degree of uniformity in terms of periodicity of the structure, as well as no noticeable deviation in the values of both the trench depth and width. The second sample listed in Table 3.3 has been fabricated to experimentally validate the effect observed during the numerical investigation on the trench depth, i.e. the occurrence of a high-order SSPP mode as the trench depth is increased beyond 50 µm.

3.3.2. EXPERIMENTAL SETUP

The experimental investigation of the samples fabricated with the procedure reported in the previous notes has been performed by employing a typical THz-TDS setup [105,192]. In this setup, we used a broadband THz source, with a full-bandwidth of $B_W < 4$ THz, as illustrated in Figure 3.15(a), where we show a sketch of the experimental setup. In more detail, the experimental investigation involved the use of a short near infrared (NIR) optical pulse (800 nm, 150 fs, 80 MHz), generated by a Ti:Sapphire laser. The pump and probe beams are obtained by employing a 90/10 beam splitter. On one arm, THz pulses are generated by feeding a PCA [9] with the pump beam, which features an average optical power of 50 mW. Moreover, a bias voltage is applied to the PCA by means of an external power supply (40V @ 10 kHz). On the other arm, the detection of THz pulses is carried out via an FS-EOS technique [30], employing a 3-mm-thick ZnTe <110> EO crystal. The use of an EO crystal with a large thickness [31] allows to achieve a higher peak amplitude of the THz electric field, as well as a larger separation between echoes in the entire temporal scan window (> 60 ps, taking into account the refractive index of ZnTe at THz frequencies, ~ 3.2 [193]). However, employing such a thick EO crystal comes at the expenses of a narrower spectral bandwidth of the detected signal. In more detail, the detected THz pulse exhibits a central frequency of f_c ~ 0.7 THz and a full spectral bandwidth of B_W ~ 2.5 THz. Nonetheless, this is not a significant issue in our specific case, since we are mainly interested in detecting the properties of the SSPP resonances in the device spectral response, the position of which falls in a frequency window narrower than 2 THz. The TWWG is placed between two off-axis mirrors with a focal length of 2 inches (~ 5 cm), as shown in Figure 3.15(a). In our setup, two hyper-hemispherical silicon lenses are employed for the coupling of the THz beam inside and outside the TWWG, resulting in an enhancement of the efficiency of both the in- and out-coupling [194]. A picture of the TWWG with the attached hyper-hemispherical silicon lenses is shown in Figure 3.15(b). Since the lenses feature a 1-inch diameter, a hole with the same diameter is drilled into the PMMA holders, so to place them as close as possible to both the input and output of the TWWG. In more detail, the 1-inch diameter hole hosting the lens is drilled first, by means of an end mill. Subsequently, the smaller hole, which determines the wire interspacing, is made by employing a wire drill. The TWWG is mounted on a three-dimensional translation stage, as illustrated in Figure 3.15(b), which allows for the optimization of the coupling of the THz radiation into the TWWG, as well as for its correct routing towards the output lens. The optical probe beam propagates through a mechanical delay line, and is then focused into the EO crystal surface by means of a lens. The out-coupled THz beam from the TWWG is then focused on the EO crystal, at the same focal point of the optical probe beam, by means of an off-axis mirror with a 2-inch focal length. The

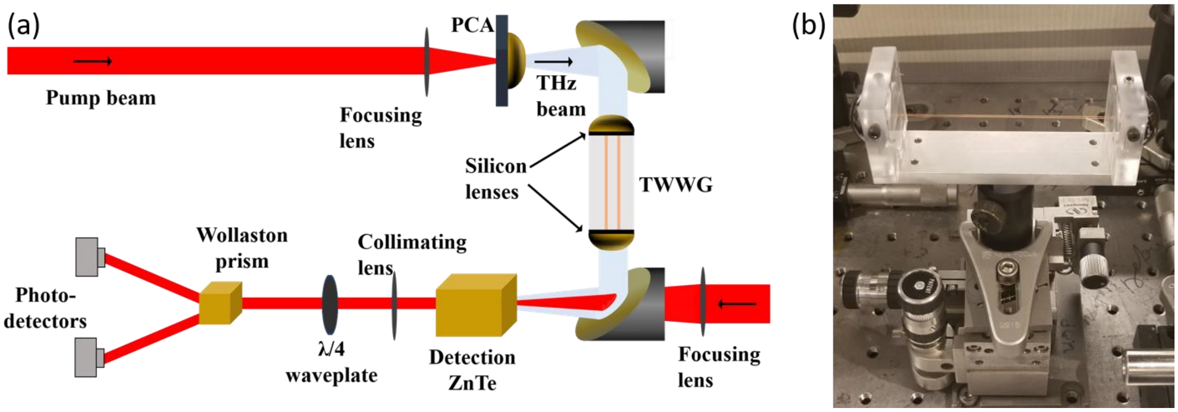

Figure 3.15. (a) Schematic of the THz time-domain spectroscopy (THz-TDS) setup employed for the experimental characterization of the samples, with the trench geometrical parameters listed in Table 3.3. The THz pulses are generated by the laser excitation of a photoconductive antenna (PCA). Two hyper-hemispherical silicon lenses are attached to both the PMMA holders, so to enhance the in- and out-coupling efficiency. The out-coupled THz beam is then focused onto a ZnTe <110> electro-optic (EO) crystal, together with the optical probe beam, by means of an off-axis parabolic mirror, to carry out electro-optic sampling (EOS). The signal collected by the photodetectors is then acquired by means of a lock-in amplifier, which is synchronized with the bias modulation frequency, i.e. 10 kHz. (b) Picture showing the TWWG mounted on a three-dimensional stage, which allows for the correct positioning of the TWWG along the THz beam path.

off-axis mirror exhibits a hole drilled at its center, so that the probe beam can be collinearly focused onto the EO crystal surface, together with the THz beam. The optical probe beam is then sent through a quarter-wave plate, which induces a change in its polarization, from linear to elliptical (because of the presence of the THz field, see Section 3.1.3), and then through a Wollaston prism, which separates the two polarizations that are then sent to a balanced photodetector. The differential signal collected by the photodetector is acquired by means of a lock-in amplifier, which is synchronized to the bias modulation frequency, i.e. 5 kHz. It is worth highlighting that, all the experimental characterizations reported and discussed in the following notes, have been carried out by enclosing the setup in a box purged with nitrogen, so to avoid the occurrence of the water vapor absorption peaks (see Section 1.3).

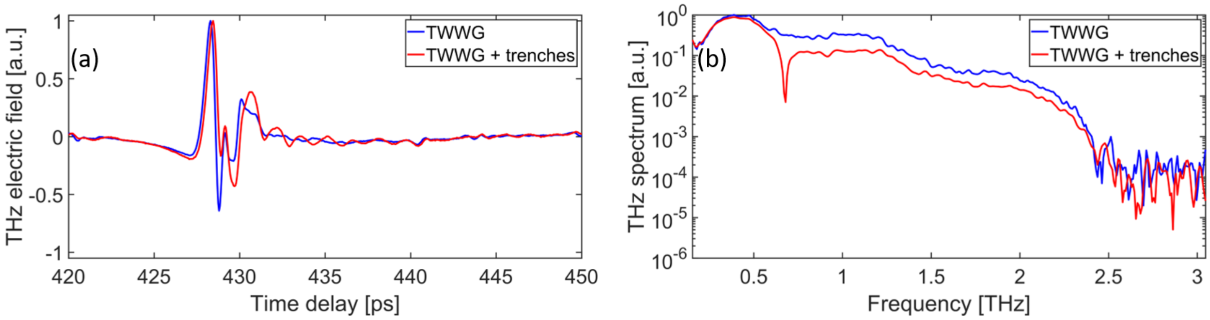

Figure 3.16. Temporal profiles of the THz electric field (a) and corresponding spectra (b) retrieved after propagation in a standard TWWG (blue solid line), i.e. two bare copper wires, and in the TWWG where one of the wires is replaced with the fabricated sample (Sample #1, red solid line). Note the reshaping of the main THz pulse, as well as the ringing following it, which is a typical effect of an electromagnetic wave propagating through a resonating structure. Both the temporal waveforms and the corresponding spectra are normalized to their own maxima.

3.3.3. EXPERIMENTAL CHARACTERIZATION

In a very similar way to the theoretical investigations discussed in the previous notes (see Section 3.2), for the retrieval of the experimental transfer function of the sample, we proceeded as follows. We considered the temporal waveform recorded after the propagation in a conventional TWWG, i.e. two bare copper wires, as the THz pulse reference. Subsequently, we replaced one of the copper wires in the TWWG with one of the fabricated samples, thus retrieving the corresponding temporal waveform of the THz electric field in the same fashion. In this way, the spectral response returns the effects caused only by the presence of the trenches. Finally, we reconstructed the FFT-evaluated spectra corresponding to the retrieved temporal waveforms, and we calculated the transfer function of the sample under study as indicated in Eq. (3.14). The results obtained from the experimental characterization of the first sample (Sample #1 in Table 3.3) are shown in Figure 3.16. In particular, in Figure 3.16(a) we show the temporal waveforms recorded after propagation within the standard TWWG (blue solid line) and within that the waveguide carrying the fabricated sample (red solid line). The FFT-evaluated spectra corresponding to the waveforms are shown in Figure 3.16(b).

From Figure 3.16(a), we can observe a reshaping of the temporal waveform after the propagation of the THz beam in the TWWG comprising the fabricated sample. For instance, we

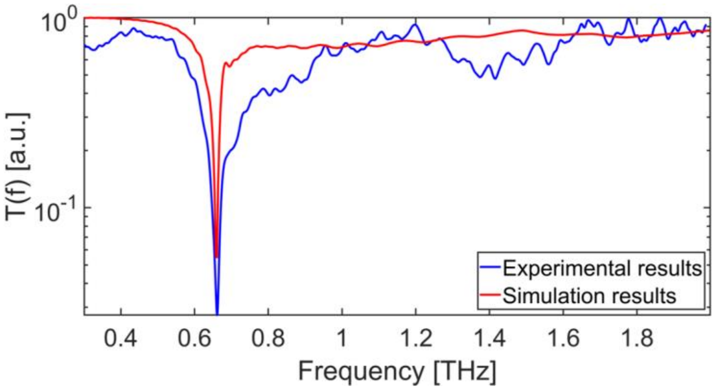

Figure 3.17. Comparison between the experimental (blue solid line) and simulated (red solid line) transfer functions, evaluated as indicated in Eq. (3.14), for the Sample #1, the geometrical parameter values of which are listed in Table 3.3. We can observe a good agreement between the two curves, with the frequency position of the SSPP fundamental mode being the same, i.e. f_{SSPP} ~ 0.65 THz. Moreover, in both curves, we can notice that the trenches fabricated on the wire surface cause the introduction of losses in the high-frequency portion of the spectral response.

can observe a ringing following the main THz pulse, which is a typical effect of an EM wave propagating through a resonating periodic structure. Moreover, in Figure 3.16(b), we can see that the ringing seen in the red curve in Figure 3.16(a) has to be attributed to a resonance, the frequency position of which is ~ 0.65 THz, with a depth larger than 1 order of magnitude (~ 10 dB). Furthermore, the low-frequency portion of the spectrum, i.e. $f < 0.6$ THz, does not seem to be significantly affected by the resonating structure, as it can be inferred by the overlap between the two curves. On the other hand, we can observe that the trenches fabricated on the wire surface cause an effect on the high-frequency portion, i.e. the introduction of frequency-dependent losses (< 2 dB for $f > 1$ THz). Moreover, in Figure 3.17 we show a comparison between the simulated (red solid line) and experimental (blue solid line) spectral responses of the sample under study, *T(f)*, evaluated as indicated in Eq. (3.14). We can immediately observe a good agreement between the two transfer functions, which both exhibit a single resonance due to the presence of the resonating structure, i.e. what we previously referred to as the SSPP fundamental mode. Furthermore, the frequency position of this resonance, f_{SSPP} ~ 0.65 THz, is identical in both the curves, with only a slight difference in their depth (~ 12 dB in the red curve, and ~ 14 dB in the blue curve). As it can be inferred from the comparison in Figure 3.17, the

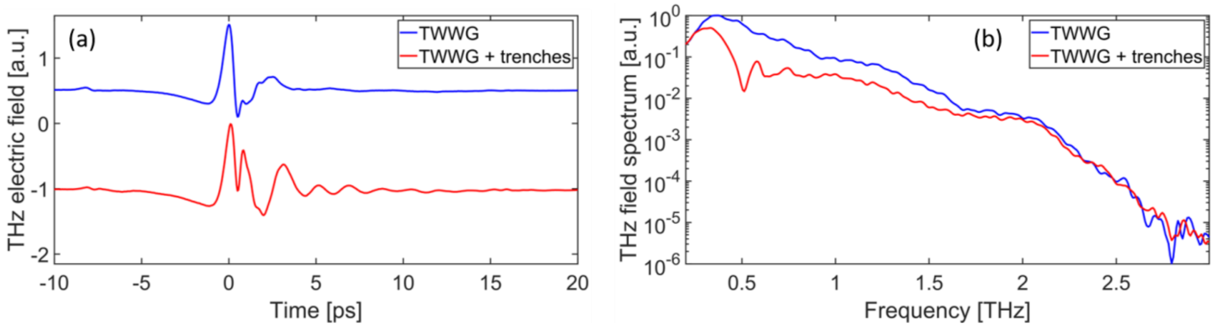

Figure 3.18. Temporal profiles of the THz electric field (a) and corresponding field spectra (b) retrieved from the experimental characterization of sample #2, where the trench depth is increased from 50 to 70 μm, with the values of the other parameters fixed at those listed in Table 3.3. We can notice the presence of two SSPP resonances, i.e. the SSPP fundamental mode at ~ 0.5 THz, and a high-order SSPP resonance at ~ 0.65 THz. Both the temporal waveforms and the corresponding spectra are normalized to their own maxima.

experimental and simulated transfer functions are very similar, especially in terms of the properties of the SSPP resonance, thus validating the findings from the numerical investigation (see Section 3.2). Moreover, we fabricated one more sample (Sample #2 in Table 3.3) to experimentally confirm the effects observed in the numerical investigation of the trench depth. In particular, we observed the occurrence of a high-order SSPP resonance as the trench depth is increased and exhibits values close to the trench width. To confirm this effect, we fabricated a sample where the trench depth has been increased from 50 to 70 μm (see Table 3.3). We then proceeded with the experimental characterization of this second sample, by employing the same experimental setup and following the same steps reported the beginning of this section.

The experimental results are illustrated in Figure 3.18. In particular, in Figure 3.18(a) we show the temporal waveforms retrieved either after propagation in a plain TWWG (blue solid line) or after propagation in a TWWG comprising the fabricated sample (red solid line). Additionally, in Figure 3.18(b) we plot the FFT-evaluated spectra corresponding to the temporal waveforms shown in (a). From Figure 3.18(a), we can observe a profound reshaping of the THz electric field waveform after its propagation in the TWWG comprising the fabricated sample, with a residual ringing after the main pulse that can be ascribed to the reflections at each edge of the trenches, as explained in Section 3.2.1. In the frequency domain, the effects seen on the temporal waveforms cause the occurrence of two SSPP resonance in the corresponding

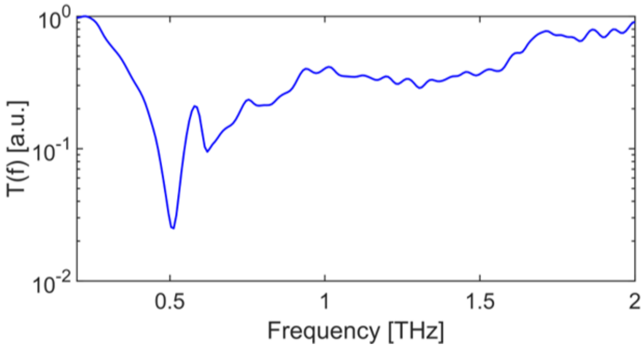

Figure 3.19. Experimentally-retrieved transfer function of Sample #2, *T(f)*, evaluated as indicated in Eq. (3.14). Here, the values of the trench parameters are those listed in Table 3.3. We can observe two resonances. The first is the SSPP fundamental mode, at ~ 0.5 THz, with a depth of ~ 17 dB, while the second, i.e. the high-order SSPP mode, is at ~ 0.65 THz, with a depth of ~ 10 dB, as predicted by the numerical investigation results discussed in Section 3.2.1.

spectrum, as shown in Figure 3.18(b). The first resonance, i.e. the SSPP fundamental mode, appears at around 0.5 THz, while the high-order mode occurs at around 0.6 THz. Moreover, in Figure 3.19 we show the experimentally-retrieved transfer function, *T(f)*, evaluated as indicated in Eq. (3.14). From here, we can observe that the resonance caused by the SSPP fundamental mode is strong, with its depth being almost two orders of magnitude (~ 17 dB). This depth value is slightly higher than that obtained from the characterization of the first sample (~ 14 dB), the transfer function of which is shown in Figure 3.17. This seems to imply that an increase in the trench depth translates in a slight increase of the resonance strength. On the other hand, the high-order SSPP resonance is weaker (~ 10 dB). These results are in good agreement with the findings from the numerical investigation reported in Section 3.2.1 and illustrated in Figure 3.7(a). We can also observe the introduction of additional losses in the frequency range from 0.7 to 1.5 THz (~ 4 dB). These losses may be ascribed to the radiative losses of the THz radiation due to the discontinuity introduced by the trenches fabricated on the wire surface. Summarizing, the reported results from the experimental characterization performed via the THz-TDS setup shown in Figure 3.15(a) are in good agreement with the findings from the numerical investigations discussed in Section 3.2. In what follows, we discuss on the implementation of a THz-Bragg Grating by exploiting the Bragg-like behavior of the designed structure as the period exhibits values comparable with the central wavelength of the THz field.

3.4. DESIGN OF A TERAHERTZ BRAGG GRATING

From the numerical investigations on the grating period, which are discussed in Section 3.2.3, we found out that, depending on the size of the grating period, the simulated structure can be treated in different ways. In more detail, if the period is in the sub-wavelength scale, i.e. $p \ll \lambda_{THz}$ (as it happens, for instance, in the case of photonic crystals), then the structure can be treated as an effective medium. On the other hand, if the grating period is comparable in size with the central wavelength of the propagating THz field, i.e. $p \sim \lambda_{THz}$, then it can be treated as a Bragg Grating (BG) structure [190,191]. In more detail, by choosing a grating period of p > 250 μm, with a small trench width value (~ 40 μm), induces Bragg-like resonances in the device spectral response, thus mimicking the behavior of Bragg Gratings. Therefore, the frequency position of the Bragg-like resonances induced by the so-implemented structure, can be determined from Eq. (3.16), by replacing the corresponding order of the Bragg resonance (m = 1, 2, 3, …). Nonetheless, we also observed that the Bragg resonances induced by a so-designed structure are quite weak (< 10 dB), because it induces only a weak perturbation of the propagation constant of the THz field inside the TWWG. Moreover, the larger the grating period, the weaker the aforementioned perturbation, thus resulting in even weaker Bragg resonances. A possible approach to obtain stronger resonance, similar to that employed in the case of FBGs, is to increase the number of fabricated trenches on the copper wire, so to increase the perturbation of the THz field propagation constant.

In what follows, we show that, with a proper design of the structure, it is possible not only to induce a strong Bragg resonance (> 20 dB) in the spectral transfer function, but also to remove the high-order Bragg modes by filtering out the high-frequency portion of the THz spectrum. Let us discuss the design process of the structure. The first step was the numerical investigation of a TWWG featuring a periodic array of trenches, exhibiting sub-wavelength widths ($w \ll \lambda_{THz}$), the sketch of which is shown in Figure 3.20(a). In this particular case, the trenches geometrical parameters are set as follows: trench depth of d = 40 μm, trench width of w = 35 μm, and grating period of p = 80 μm. In Figure 3.20(b) we show the simulated dispersion relation of the standard TWWG, i.e. two bare copper wires (green line), which exhibits a linear dependence upon the frequency, thus indicating a dispersion-free propagation in the waveguide.

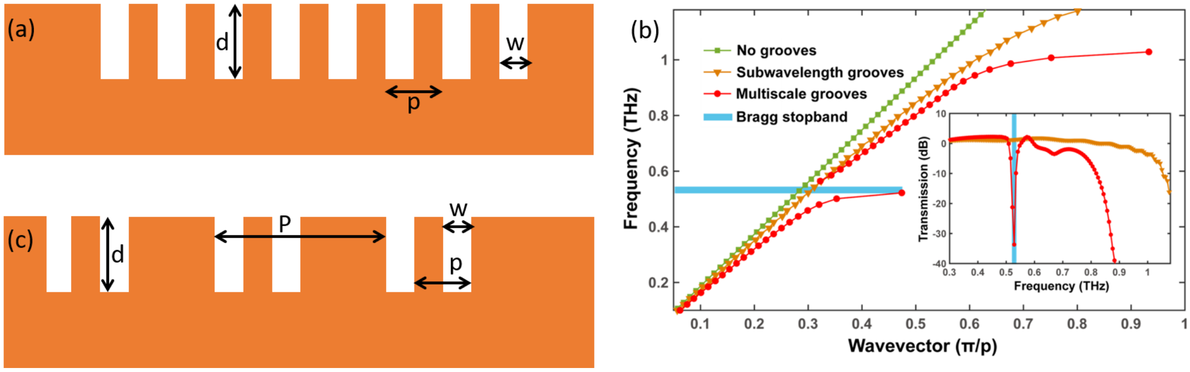

Figure 3.20. (a) Schematic of the TWWG with an array of sub-wavelength-scale trenches etched on the wire surface. Here, *d* is the trench depth, *w* is the trench width, and *p* is the grating period. (b) Simulated dispersion relations for the standard TWWG (green line), the TWWG with sub-wavelength-scale (orange line) and multiscale (red line) trenches. The inset in (b) shows the simulated transfer functions, evaluated as indicated in Eq. (3.14), after propagation through the TWWG with the sub-wavelength-scale (orange line) and multiscale (red line) trenches. (c) Schematic of the TWWG with an array of multiscale trenches, obtained by superimposing a wavelength-scale spatial periodic modulation, with period *P*, to the structure shown in (a).

Nonetheless, the dispersion relation of the TWWG with the sub-wavelength trenches (orange line) is not linear, with the group velocity, v_g, of the SSPPs decreasing as the frequency increases. In particular, we can observe a cut-off frequency at ~ 1.2 THz, showing that the SSPPs are stopped [195] and that the THz radiation above this frequency cannot be guided within the TWWG.

A possible way to lower the value of the cut-off frequency is to increase the value of the trench depth, *d*. However, a deep cut on the copper wire surface would significantly lower the robustness of the wire itself, which in turn could lead to its fracture when the tension is applied during the mounting of the TWWG. An alternative approach is the superimposition of a wavelength-scale modulation to the structure, i.e. $P \sim \lambda_{THz}$). A sketch of the novel design is shown in Figure 3.20(c) where, with respect to the structure shown in Figure 3.20(a), we can observe the introduction of a periodic spatial modulation of P = 280 μm. The simulated dispersion relation of the TWWG with the multiscale trenches, shown as a red line in Figure 3.20(b), illustrates the existence of a Bragg resonance at f_{Bragg} = 0.53 THz, as evaluated from Eq. (3.16), while the cut-off frequency of the structure is shifted from 1.2 THz to 1 THz.

Moreover, by changing the value of the spatial modulation, *P*, the frequency position of the Bragg resonance can be tuned over a broad range of frequencies. Additionally, we retrieved the simulated transfer functions for both the TWWG structures, i.e. the one sub-wavelength-scale trenches and that with the multiscale ones. For the accomplishment of this task, we considered a THz beam exhibiting a central frequency of f_c = 0.7 THz and a full-bandwidth of B_W ~ 2.5 THz, which exhibits a Gaussian spatial profile with a waist radius of 600 μm. The temporal waveform and the corresponding FFT-evaluated spectrum of the input THz pulse are those shown in Figure 3.6(a-b). The simulated transfer functions shown in the inset of Figure 3.20(b) were retrieved by following the same procedure reported in Section 3.2 for the numerical investigations, i.e. by reconstructing the simulated temporal waveforms that propagate through either a plain TWWG (two bare copper wires), or one with the sub-wavelength and multiscale trenches. The corresponding spectra were then evaluated via an FFT algorithm, the ratio of which returns, as indicated in Eq. (3.14), the transfer functions, *T(f)*.

From the inset in Figure 3.20(b), we can observe a profound difference between the two transfer functions. In more detail, the TWWG featuring the sub-wavelength-scale trenches (orange line) exhibits a smooth transfer function, with negligible losses, and a cut-off frequency of ~ 1.2 THz. On the other hand, the TWWG with the multiscale trenches (red line) shows a lower cut-off frequency (~ 0.8 THz), and a Bragg resonance at ~ 0.5 THz, which exhibits a large depth (~ 35 dB). Moreover, we can observe another resonance occurring at ~ 0.65 THz. This non-Bragg resonance could be ascribed to the asymmetry of the structure, i.e. the fact that the multiscale trenches are fabricated on the surface of only one wire. Therefore, the non-Bragg resonance could arise from an out-of-phase condition, similar to that observed in the theoretical investigation of the trench depth, discussed in Section 3.2.1. Therefore, a structure featuring the trenches on both the copper wires should results in the disappearance of such a resonance. To validate this point, we simulated the propagation of the same input THz pulse in a TWWG featuring the multiscale trenches on both the copper wires, via FDTD algorithm, and retrieved the corresponding transfer function as indicated in Eq. (3.14).

The results from the numerical investigation are shown in Figure 3.21. In this plot, we illustrate a comparison between the simulated transfer functions retrieved from the propagation

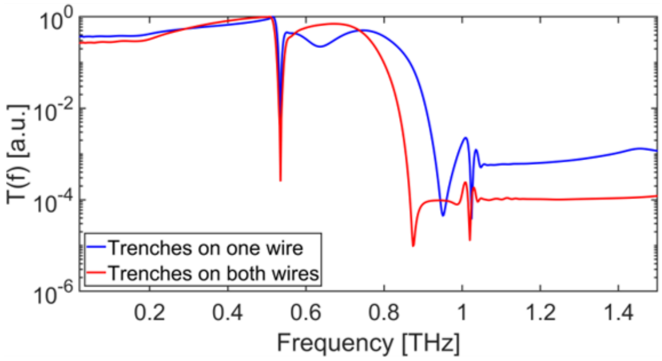

Figure 3.21. Comparison between the simulated transfer functions, evaluated as indicated in Eq. (3.14), of the multiscale trenches etched on either one (blue solid line) or both (red solid line) copper wires. Note the differences between the two transfer functions. The cut-off frequency of the red curve is shifted towards lower values (from ~0.9 to ~0.8 THz). Moreover, the non-Bragg stop-band in the blue curve does not occur in the case where the trenches are etched on both the wires in the TWWG, thus implying that its origin must be ascribed to the structure asymmetry.

of the same input THz pulse in two different TWWGs, featuring the multiscale trenches on either one (blue solid line) or both (red solid line) copper wires. From this comparison, we can immediately observe that the symmetry of the designed structure significantly changes the spectral response of the samples under study. In more detail, a first aspect that we can observe is that the cut-off frequency is shifted towards lower values, i.e. from ~0.9 to ~0.8 THz, as both the wires in the TWWG exhibit the multiscale trenches. This might be ascribed to the stronger perturbation induced by the sub-wavelength scale trenches, i.e. by the parameter p = 80 μm, which we recall is that responsible for the occurrence of the cut-off frequency in the spectral response. Moreover, the symmetry does not influence the position of the Bragg resonance, even though it produces a stronger resonance (~40 dB instead of 35 dB) in the case where the multiscale trenches are on both the copper wires, as we can see from the plot. Finally, the non-Bragg stop-band at ~ 0.65 THz is not induced in the spectral response if the multiscale trenches are present on both the copper wires.

To better investigate the latter two aspects, in Figure 3.22 we illustrate the THz field distributions for a TWWG where the multiscale trenches are on either just one (a, c) or both (b, d) copper wires. In particular, the field distributions are evaluated at the Bragg resonance frequency (~ 0.53 THz), shown in Figure 3.22(a-b), and at the non-Bragg resonance frequency

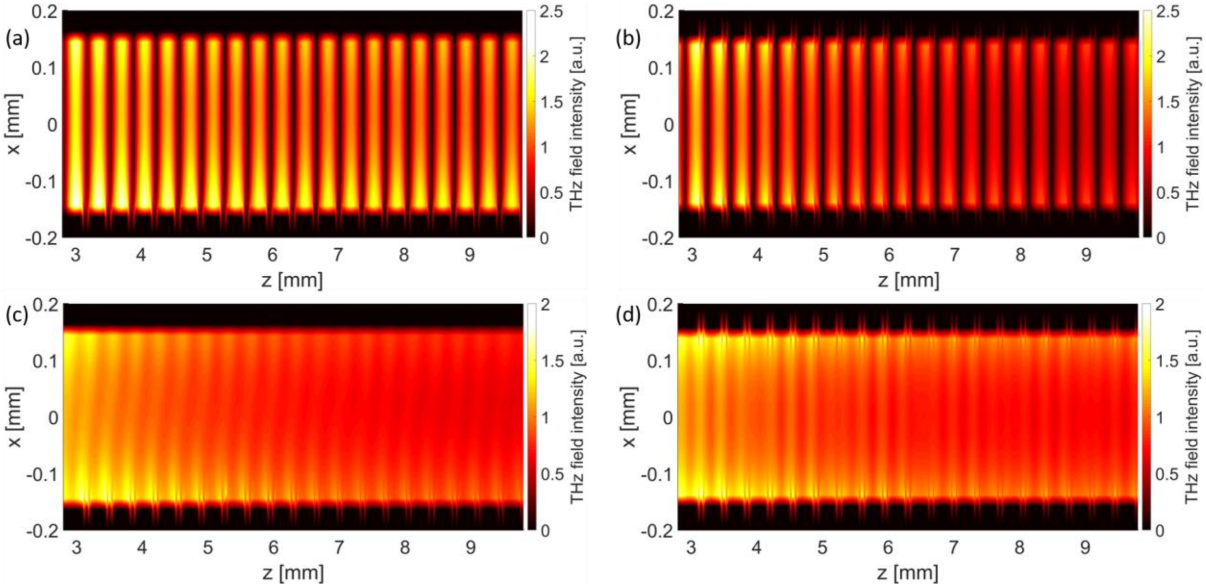

Figure 3.22. Simulated THz field intensity distributions within the TWWG, for the case where the trenches are fabricated on either one (a, c) or both (b, d) the copper wires. In particular, in (a-b) we show the distributions at the Bragg frequency (~ 0.53 THz), while in (c-d) w show those at the non-Bragg stop-band frequency (~ 0.65 THz). Note the differences between the distributions in (c) and (d). In (c), the THz field exhibits a slight tilt along the *y*-axis because of the phase shift introduced by the structure asymmetry.

(~ 0.65 THz), shown in Figure 3.22(c-d). Let us start by analyzing the field distribution at the Bragg frequency for the cases where the trenches are fabricated on either one, Figure 3.22(a), or both the copper wires, Figure 3.22(b). The main difference we can observe is in the amplitude of the THz field intensity close to the TWWG output, which appears to be larger for the case where the multiscale trenches are etched on just one wire, because of the weaker perturbation induced by the periodic structure. This, in turn, would result in a weaker Bragg resonance, which is in agreement with the plot in Figure 3.21.

A more significant difference can be observed for the field intensity distributions evaluated at the non-Bragg stop-band frequency (~ 0.65 THz). In particular, we can observe that the THz field within the TWWG shows a slightly tilted wave-front, with respect to the vertical direction (*y*-axis), for the case where the multiscale trenches are present on just one wire, as shown in Figure 3.22(c). Conversely, the field distribution in Figure 3.22(d), is much different, with the THz field being parallel to the axis hosting the centers of both the copper wires. As such, no extra phase shift occurs within the TWWG, resulting in the disappearing of the non-Bragg stop-band in its transfer function. Even though the fabrication of the multiscale trenches on both the copper wires in the TWWG could allow us to avoid the occurrence of this spurious non-Bragg resonance, as well as achieve a larger attenuation of the high-frequency components in the spectral response, the physical alignment of the two processed wires during the mounting of the TWWG is not trivial. As a matter of fact, not only one would have to guarantee a perfect spatial overlap of the whole structure, i.e. same start and ending points, yet the two wires would also have to perfectly face each other, so that it would be possible to avoid any undesired effects on the spectral response, as mentioned in the previous notes. As a result, we characterized a TWWG with only one wire featuring the multiscale trenches. The so-designed structure features the following geometrical parameters: a trench depth of d = 40 µm, a trench width of w = 35 µm, a period of p = 80 µm, a spatial periodic modulation of P = 280 µm, with the total number of periods in the sample being N = 150, and a total length of the structure of L = 4.2 cm.

3.5. FABRICATION AND CHARACTERIZATION OF THE TERAHERTZ BRAGG GRATINGS

3.5.1. EXPERIMENTAL SETUP

The fabrication process of the multiscale sample is identical to that reported in Section 3.3.1 and shown in Figure 3.13. A picture of the fabricated sample, taken by means of an optical microscope, is illustrated in Figure 3.23. After the fabrication process, the sample was characterized by employing a THz-TDS setup that, for many aspects, is similar to the one shown in Figure 3.15(a) and discussed in Section 3.3.2. As in the previous setup, the experimental setup employed for the characterization of the structure designed in Section 3.4, exploits the laser excitation of PCAs for the generation of THz radiation, and the FS-EOS technique for its detection. The main differences between the two experimental setups concern the scheme employed for the in- and out-coupling of the THz beam in and out of the TWWG, as well as the use of a different PCA for the generation of the THz pulses. Let us address the individual changes in more detail. In the setup shown in Figure 3.15(a), the THz pulses were generated by

Figure 3.23. Picture, taken via an optical microscope, of the sample featuring the multiscale trenches, the procedure of which is shown in Figure 3.13. Note that, at this scale, the sample shows a good uniformity in the structure periodicity.

means of a PCA where the metal electrodes exhibited a dipole configuration. In our case, we employed another PCA with a different topology for the metal electrodes, which allows to lower the necessary bias voltage to apply across them. The novel PCA is equipped with an array of lenses, which focus the incident collimated optical beam on the substrate material, in the volume between the metal electrodes. Such a configuration shows several advantages, such as an easier alignment of the optical pump beam, as well as for a higher electric field emitted by the source. Additionally, the metal electrodes in the novel PCA exhibit an interdigitated structure, with a 5 μm gap between the electrodes. Therefore, it is possible to lower the bias voltage to be applied to the PCA itself (from 40 to 10 V).

Moreover, in the setup illustrated in Figure 3.15(a), both the in- and out-coupling of the THz beam were performed by employing hyper-hemispherical silicon lenses. A so-implemented scheme allows for the enhancement of the coupling efficiency if compared to other previously demonstrated schemes [123,194], because of the smaller spot size of the focused THz beam at the TWWG input. Nonetheless, employing silicon lenses also results in an increase in the losses. In more detail, in spite of the very low absorption coefficient intrinsic to silicon (< 0.2 cm^{-1}) at THz frequencies, it also exhibits a high refractive index (~ 3.4), both at optical and THz frequencies, which in turn leads to a high contrast between the air and silicon refractive indices (1 and ~3.4, respectively, leading to a contrast of Δn ~ 2.4). Therefore, at each air-lens interface, a large fraction of the THz beam is reflected back. By taking into account the refractive indices of air and silicon, the field reflection coefficient can be evaluated as $\rho =$

$\frac{n_{Si}-n_{air}}{n_{Si}+n_{air}} \sim 54\%$. Moreover, since the coupling scheme involves the use of two silicon lenses, it results in the introduction of almost an order of magnitude of additional losses.

These losses can be significantly lowered by employing a different coupling scheme. More specifically, we replaced the hyper-hemispherical lenses with polymethylpentene (also known as TPX) ones. This material exhibits a significantly lower refractive index at THz frequencies (n_{TPX} = 1.5) [196], thus resulting in a better matching with the refractive index of air (Δn ~ 0.5), which in turn results in a strong reduction of the reflection coefficient at each air-lens interface, i.e. $\rho = 20\%$. Moreover, TPX features low absorption losses (< 0.5 cm^{-1}) at THz frequencies [196], and it allows for the transmission in both the visible and IR spectral regions, hence making the alignment of the THz-TDS setup easier. A sketch of the experimental setup employed for the characterization of the sample with the multiscale trenches designed in Section 3.4 is shown in Figure 3.24. In particular, the collimated optical pump beam is sent on the array of lenses embedded in the PCA, and is then focused in the gap volume between the metal electrodes. Subsequently, a 5-cm-focal-length TPX lens allows for the collimation of the THz beam emitted by the PCA. At this point, a 1-cm-focal-length aspherical TPX lens is employed to strongly focus the THz beam at the TWWG input. After propagation within the TWWG, the beam is coupled outside the waveguide and is then collimated via a third TPX lens, the focal length of which is 10 cm. Both the probe and THz beams are then focused on the 3-mm-thick ZnTe EO crystal to carry out the FS-EOS detection, as discussed in Section 3.3.2.

3.5.2. EXPERIMENTAL RESULTS

The experimental characterization of the sample with the multiscale trenches shown in Figure 3.23 was performed as follows. After a proper alignment of the optical setup, the plain TWWG is mounted on the same three-dimensional stage employed in the previous investigation, a picture of which is shown in Figure 3.15(b). We then carried out the FS-EOS technique to retrieve the THz electric field temporal waveform at the photodetector. Subsequently, one of the copper wires in the TWWG is replaced with the fabricated sample featuring the multiscale trenches, and then we recorded the temporal waveform of the THz electric field in the same fashion. By means of an FFT algorithm, we then evaluated the field

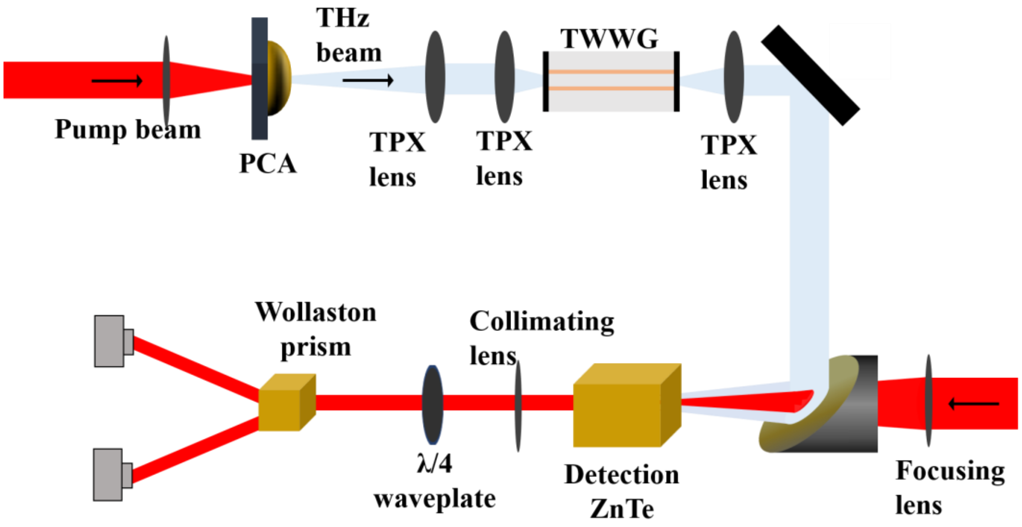

Figure 3.24. Sketch of the experimental setup (THz-TDS) employed for the characterization of the sample shown in Figure 3.23. This setup employs a different coupling scheme with respect to the setup shown in Figure 3.15(a). Briefly, a TPX lens with a focal length of 5 cm is used for the collimation of the beam emitted by the PCA, while an aspherical TPX lens is used for the coupling of the beam within the TWWG. The out-coupled beam is then collimated via a third TPX lens, with a focal length of 10 cm. Finally, the FS-EOS is carried out, in the same way as reported in Section 3.3.2.

spectra corresponding to the retrieved temporal waveforms, and, finally, we determined the device spectral transfer function, as indicated in Eq. (3.14). The results obtained from the experimental characterization with the experimental setup discussed in Section 3.5.1, are shown in Figure 3.25. In more detail, in Figure 3.25(a) we show the temporal waveforms retrieved after propagation in a plain TWWG, i.e. two bare copper wires (blue solid line), and that after propagation in the TWWG with the multiscale trenches (red solid line). From the comparison between the two temporal waveforms we can immediately notice the profound reshaping of the red curve, with respect to the blue one. In particular, a first aspect we can notice is that the temporal duration of the THz pulse propagating in the TWWG with the trenches has significantly increased, as a result of the narrowing of the spectral bandwidth, which is in turn caused by the multiscale trenches. More specifically, while the temporal duration of the reference THz pulse, i.e. after propagation in the plain TWWG, is $\tau_{ref}\sim$ 0.8 ps, that of the THz pulse after propagation through the TWWG with the multiscale trenches is $\tau_{sam}\sim$ 3.1 ps. Both

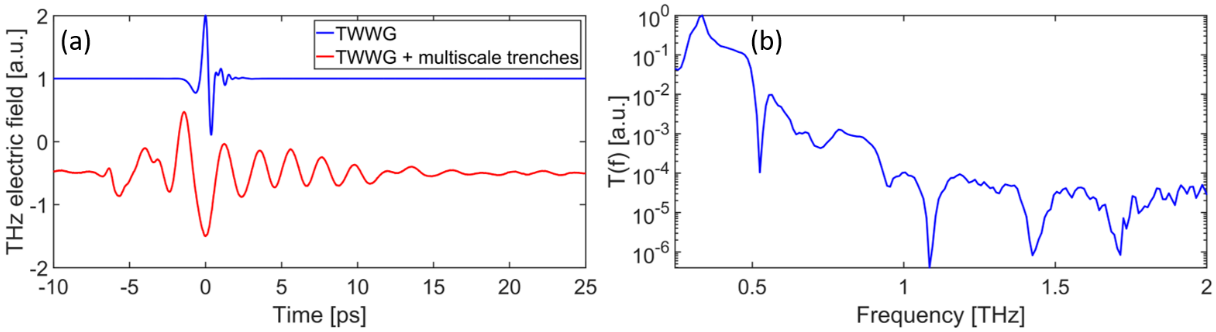

Figure 3.25. (a) Temporal profiles of the THz electric field retrieved after propagation in a plain TWWG (blue solid line), and in a TWWG where one wire is replaced with the fabricated sample (red solid line). Note the deep reshaping of the red curve, with a ringing after the main pulse, which is a typical effect of a periodic resonating structure on a propagating electromagnetic wave. (b) Experimentally-retrieved transfer function, evaluated as in Eq. (3.14). Note the Bragg resonance at ~ 0.53 THz, with a depth of ~ 40 dB. Moreover, there is a cut-off frequency at ~ 0.8 THz, which can be ascribed to the sub-wavelength-scales trenches in the sample. Both the waveforms are normalized to their own maxima, and are shifted along the *y*-axis for a better visualization.

the temporal durations were measured as the FWHM of the THz pulse. This phenomenon must be ascribed to the dispersion induced by the multiscale trenches, which is also highlighted in the dispersion relation shown in Figure 3.20(b). Moreover, we can notice a long-lasting ringing immediately after the main temporal pulse, which features a gradual amplitude damping of the residual oscillations. This ringing has to be attributed to the multiple reflections experienced by the THz pulse propagating within the TWWG with the multiscale trenches. Notably, the amplitude of the ringing in the red curve is larger with respect to that produced by the previously-investigated frequency filters, which are reported and discussed in Section 3.3.3. This implies a stronger effect induced by the resonating structure on the propagating THz field. For a qualitative investigation of the device performance in the frequency domain, in Figure 3.25(b) we also illustrate the spectral transfer function of the investigated sample, which was evaluated as indicated in Eq. (3.14). We can immediately notice the presence of the Bragg resonance at ~ 0.53 THz, as evaluated from Eq. (3.16), with a depth of around 4 orders of magnitude, i.e. ~ 40 dB, as predicted from the numerical investigation (see Section 3.4). Furthermore, we can observe a strong attenuation of all the frequency components above the Bragg resonance, which is consistent with the cut-off effect observed in the numerical investigations. In more detail, the filtering of the high frequency components must be ascribed to the sub-wavelength interspacing between two consecutive trenches, which we recall being $p = 80$ μm, which stops the propagation of the THz field, as also illustrated in Figure 3.20(b), in both the dispersion relation and the simulated transfer function. Moreover, also in the experimentally-retrieved spectral response, we can observe the presence of the non-Bragg resonance at the same frequency position predicted from the numerical investigation, i.e. ~ 0.65 THz. We recall here that this resonance has to be ascribed to the asymmetry of the structure, i.e. the fact that the multiscale trenches are present on only one of the two copper wires. This effect was also confirmed by the THz field intensity distributions shown in Figure 3.21(c-d). Overall, the results retrieved from the experimental characterization confirm the achievement of the targeted spectral response, with a strong Bragg resonance at the predicted frequency position, thus also validating the findings from the previously-discussed theoretical investigations.

CHAPTER 4

TIME-DOMAIN INTEGRATION OF TERAHERTZ PULSES

4.1. INTRODUCTION

The design and development of devices capable of efficiently perform analog signal-processing functionalities in the THz domain, i.e. the manipulation of time-varying signals, has been intensively and increasingly explored much more in the recent past. Nonetheless, we still observe a lack of operating devices for the manipulation of broadband THz pulses, i.e. with continuum bandwidths (f_{THz}) covering a large portion of the THz range. This lack of devices must be attributed to the single or quasi-single cycle nature of the THz pulses, which leads to spectra exhibiting carrier frequencies, f_{THz}, comparable with their linewidth, i.e. $f_{THz} \sim \Delta f_{THz}$ [35,59,135,136]. Due to this strict constraint, the approaches utilized in the optical range [64,70,91,197,198] cannot be borrowed to realize similar signal-processing functionalities in the THz range. Therefore, it is necessary to exploit other effects and/or phenomena featuring particularly wide and smooth, i.e. gap-free, spectral responses in order to design devices able to manipulate broadband THz signals. In what follows, we present and discuss on the design and investigation of a device able to perform the first-order temporal integration of both broad- and ultra-broadband THz pulses [2]. In order to accomplish this task, we exploit the peculiar dependence of the THz beam confinement on the frequency, occurring in a two-wire waveguide

(TWWG) with a sub-wavelength wire interspacing, i.e. the air gap between the two wires. In more detail, we show that, by properly choosing the TWWG geometrical parameters, such as the wire interspacing and radius, it is possible to achieve the targeted spectral response over a broad spectral window, i.e. $B_W > 2$ THz.

4.2. THEORETICAL ASPECTS

Generally speaking, a first-order integrator in the time domain is a device that gives at its output a temporal waveform that is the first-order integral of the input, i.e.:

$$E_{out}(t) = \int E_{in}(t)\, dt \tag{4.1}$$

In Equation (4.1), $E_{in}(t)$ and $E_{out}(t)$ are the temporal waveforms retrieved at the device input and output, respectively, with t being the time. In the frequency domain, such a device features a spectral transfer function, $H(f)$, where f is the frequency, that can be written as follows:

$$H(f) = \frac{E_{out}(f)}{E_{in}(f)} = \frac{1}{j2\pi f} = -\frac{j}{2\pi f} \tag{4.2}$$

Here, $E_{in}(f)$ and $E_{out}(f)$ are the FFT-evaluated spectra corresponding to the temporal waveforms retrieved at the device input, $E_{in}(t)$, and output, $E_{out}(t)$, respectively. For a better understanding of the effects of a first-order temporal integrator on the input signal, in Figure 4.1 we plot the ideal transfer function, in the frequency domain, of a first-order temporal integrator, in terms of both its amplitude (blue solid line) and phase (orange solid line). Briefly, Eq. (4.2) implies that a first-order temporal integrator possesses a purely imaginary hyperbolic frequency response, as well as a fixed phase delay contribution equal to -90° (or -π/2 radians) over the whole frequency spectrum. Another feature of the first-order temporal integrator, which can be inferred from both Eq. (4.2) and Figure 4.1, is a significant enhancement of the output signal, if compared to that sent at the input, in the low-frequency portion of the spectral response (≤ 1 THz in the plot). A similar behavior, in the frequency domain, has been observed by Kang *et al.* in Ref. [199], and by Seo *et al.* in Ref. [200], in the case where a propagating THz beam

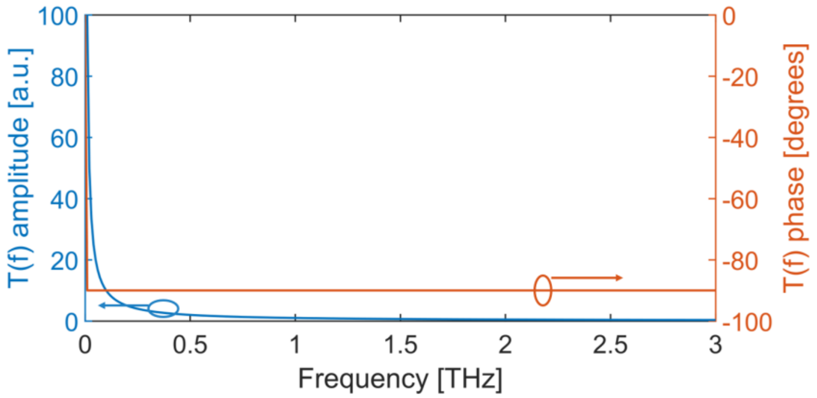

Figure 4.1. Ideal transfer function, *T(f)*, in the frequency domain, of a first-order temporal integrator. On the left axis, we plot its amplitude as a blue solid line, while on the right axis, we plot its phase as an orange solid line. The transfer function exhibits a purely imaginary hyperbolic behavior, which ideally induces a -90° (or -π/2 radians) phase-shift across the whole spectral response.

impinges on either a single or an array of slit(s) realized in between thin-film metal pads. The size of the slits, *w*, is much smaller than the central wavelength, λ_{THz}, of the input THz pulse (sub-wavelength). As the THz electric field interacts with the structure, the charge carriers surrounding the slit are forced to drift towards the gap and accumulate at its edges. In this way, the slit acts like a capacitance, which is loaded by the incident THz field. This leads to a local field enhancement (FE) of the THz electric field, which linearly scales with the wavelength. In more detail, it has been demonstrated that the THz near field (E_{slit}) confined within a slit featuring a width *w*, can be related to the incident THz electric field (E_{inc}) as follows [199]:

$$FE(f) = \left|\frac{E_{slit}(f)}{E_{inc}(f)}\right| \propto \frac{\lambda}{\pi h} = \frac{c}{\pi h f} \tag{4.3}$$

$$w \ll (h, \lambda_{THz}) \tag{4.4}$$

Here, λ and f are the wavelength and frequency of the incident THz electric field, respectively, *c* is the speed of light in vacuum, *h* is the thickness of the metal pads, and *w* is the size of the gap between the two metal pads. Moreover, as one can infer from Eq. (4.4), only if the size of the slit, i.e. the gap between the metal pads, *w*, is much smaller than both the pad thickness, *h*, and the THz wavelength, λ, Eq. (4.3) is valid. If this condition is satisfied, the field enhancement shows an exact inverse proportionality with the metal pad thickness, that is the field enhancement increases as the metal pad thickness decreases, and vice versa. Notably, the trend shown in Eq. (4.3) resembles the transfer function of a first-order temporal integrator. In what follows, we demonstrate that a similar condition can also occur in a THz waveguide, such as a TWWG, by satisfying specific conditions on the values of their geometrical parameters, such as the wire radius and wire interspacing. In other words, the frequency response of this waveguide can be properly tailored so to exhibit the behavior of a first-order temporal integrator, with a very good approximation.

We recall here that a waveguide is generally employed for the confinement of an EM wave and force it to propagate in a smaller volume than that it would otherwise occupy in free-space. However, this type of confinement of the travelling wave is wavelength-dependent and can be quantified in terms of a so-called field enhancement factor. We stress the fact that the FE is not just a plain amplification of the radiation strength, since a waveguide is a purely passive device. Rather, it is the result of the distribution of the energy associated to each frequency component, as some of them are favored against others by their confinement. The field enhancement of THz waves has been observed and reported also in a TPPWG, where not only the gap between the two plates is gradually decreased down to sub-wavelength values, while moving from its input to its output, but also their widths [98,201], forming a sandwich-like structure. In the particular case described in this chapter, we exploit a design based on the TWWG, which is reshaped so that it is possible to fulfill the conditions for the achievement of the time-domain integration. As the THz radiation is focused at the TWWG input, its fundamental TEM mode is excited. If the wire interspacing is comparable in value with the THz beam central wavelength, i.e. $2g \sim \lambda_{THz}$, then the THz electric field remains confined in the area between the two wires, symmetrically distributed between the two wires. Under certain conditions, it is possible to make an analogy between the sub-wavelength slit reported in [199] and the TWWG. In Figure 4.2 we show the sketches of both structures, i.e. the nanoscale slit in (a) and the TWWG with a sub-wavelength wire interspacing in (b). On each of them, we highlight the geometrical parameters that play similar roles. It is possible to infer that the role played by the wire interspacing, $2g$, and the wire diameter, $2R$, in the TWWG is very similar to that of the slit width, w, and the metal pad thickness, h, in the nano-slit, respectively. At first glance, considering the analogy illustrated in Figure 4.2, we can ascertain that the THz field

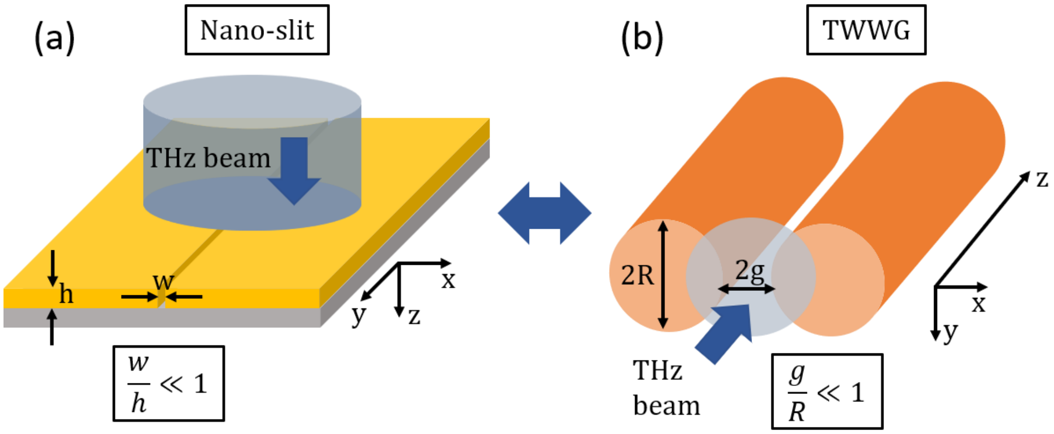

Figure 4.2. Comparison between the enhancement of the THz field between (a) a sub-wavelength slit (nanoscale) and (b) a TWWG with a sub-wavelength wire interspacing. Under certain conditions, it is possible to make an analogy between the two structures. The slit width (*w*) and the metal pad thickness (*h*) in (a) play an analogous role to that of the wire interspacing (*2g*) and the wire diameter (*2R*) in (b), respectively. Regarding the TWWG, if the condition $\boldsymbol{\frac{g}{R} \ll 1}$ is satisfied, it exhibits a field enhancement factor that is inversely proportional to the frequency, in the sub-wavelength regime, i.e. when $\boldsymbol{w, g \ll \lambda_{THz}}$.

propagating within the TWWG experiences a significant field enhancement whether the TWWG parameters fulfill the following condition:

$$g \ll (\lambda_c, R) \tag{4.5}$$

Here, g is the half-value of the wire interspacing, R is the wire radius, and λ_c is the central wavelength of the confined THz beam. Generally speaking, broadband THz pulses exhibit a central wavelength in the order of hundreds of microns. Therefore, the condition imposed by Eq. (4.5) can be satisfied by using relatively small values for the wire interspacing, e.g. $2g \sim 10$ µm. As a matter of fact, the operativity of a TWWG featuring such a tiny wire interspacing, $2g \ll \lambda_{THz}$, is different from that of a TWWG featuring a wire interspacing comparable in value with the central wavelength of the input THz pulse, $2g \sim \lambda_{THz}$. In order to gain a deeper insight on this different behavior, in Figure 4.3 we show the two-dimensional electric field distribution of the TWWG fundamental TEM mode (a, c) and its transverse profile (b, d) retrieved on the plane containing the wire centers, indicated with a white dashed line in (a, c). To accomplish

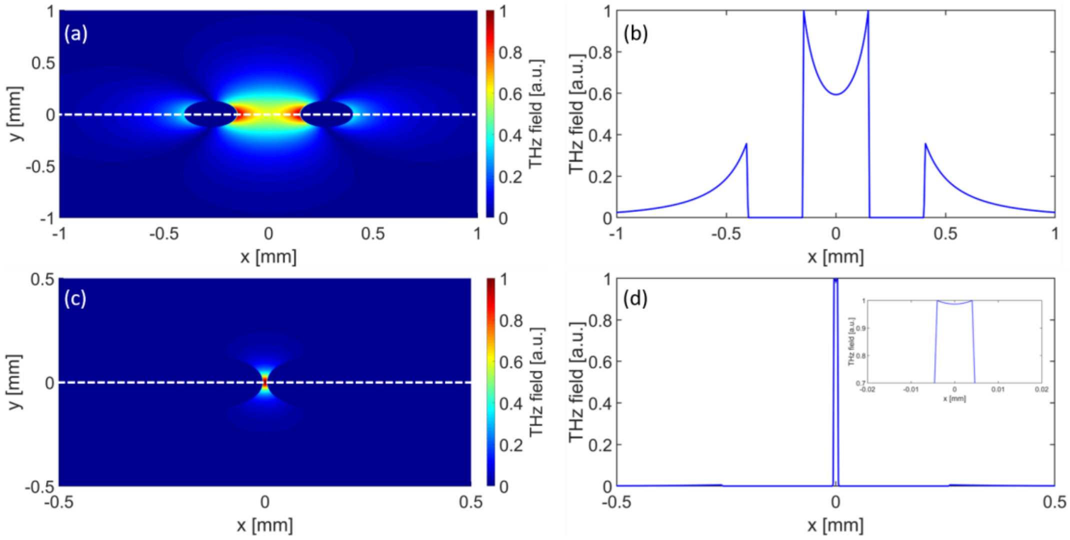

Figure 4.3. Two-dimensional color map (a, c) showing the distribution of the THz electric field related to the TWWG fundamental mode, and its transverse profile (b, d), which are calculated on the line hosting the wire centers (white dashed line). The results are shown for a TWWG with (a-b) a wire interspacing of $2g$ = 300 μm, and (c-d) $2g$ = 10 μm, respectively. For the task, we set a wire radius of R = 127 μm and a test propagating frequency of f_c = 1 THz. The inset in (d) shows a zoom of the electric field transverse profile in the sub-wavelength TWWG, for a better visualization.

this task, we considered a wire radius of R = 127 μm and a test frequency of f_c = 1 THz, corresponding to a test wavelength of λ_c = 300 μm. We then investigated the behavior of two TWWGs having different values of the wire interspacing, i.e. $2g$ = 300 μm, shown in Figure 4.3(a-b) and $2g$ = 10 μm, shown in Figure 4.3(c-d). In the first case, i.e. when $2g \sim \lambda_{THz}$, we can observe that the THz electric field exhibits two identical maxima very close to the wire surface, as also shown in Figure 4.3(b), with its amplitude decreasing while moving from the wire surface towards the center of the air gap. This implies that the TWWG fundamental mode is mostly confined in the region close to the wire surface in this case. Moreover, we can observe two external evanescent tails, on the outer side of the wires. If the wire interspacing is decreased to $2g$ = 10 μm, so that $2g \ll \lambda_{THz}$, the distribution of the THz electric field is significantly different, as we can observe in Figure 4.3(c). Indeed, we can notice that the amplitude of the field distribution seems to be uniform in the air gap, which can be observed in more detail in Figure 4.3(d) and, in particular, its inset, where we show the transverse profile of the THz electric field in the plane containing the centers of both wires. Furthermore, the evanescent tails that could be observed in the previous case, exhibit a negligible amplitude. These aspects indicate a strong confinement of the incoming THz electric field, as also shown in Figure 4.3(c), which is induced by the sub-wavelength wire interspacing, *2g*. This effect is responsible for the enhancement of the coupled THz electric field. In particular, the FE exhibits larger values as the wire interspacing is decreased to values much smaller than both the wire radius and the THz wavelength, since the coupled THz electric field would be squeezed in an ever-smaller volume.

4.3. DESIGN OF THE TEMPORAL INTEGRATOR

4.3.1. TWO-WIRE WAVEGUIDE NUMERICAL INVESTIGATION

Considering the aforementioned constraints on the values of the TWWG geometrical parameters, i.e. the wire radius (R) and the wire interspacing (*2g*), it is crucial to properly choose their values. Therefore, we performed a numerical investigation of the TWWG to be designed, by simulating the propagation of an input THz pulse that is coupled at the waveguide input and then propagates within it towards its output. Such a numerical study was carried out by employing an FDTD algorithm to solve the Maxwell's equations for the case of a THz beam propagating within the TWWG. This strategy allowed us, on one hand, to investigate the effect of the wire interspacing on the TWWG spectral transfer function, while, on the other hand, to choose the suitable values for the parameter under study. Therefore, it was possible to achieve the targeted spectral response, i.e. that shown in Eq. (4.2), over a broad spectral window, e.g. B_W > 2 THz. Additionally, as also previously highlighted (see Section 2.2.2.1), the wire interspacing is ultimately determined by the size of the hole drilled on the PMMA holders that are attached at the ends of the aluminum bar. Therefore, the optimum value for the wire interspacing must be compatible with the fabrication technique adopted for the TWWG.

For the theoretical investigation, the value of the wire radius is chosen as R = 127 μm. This choice was made in order to balance two counteracting effects, which can be inferred from Equations. (4.3) and (4.5). On one hand, from the condition imposed by Eq. (4.5), the THz beam propagating in the sub-wavelength structure experiences a *1/f* field enhancement only if $R \gg g$. Conversely, from Eq. (4.3) we can observe that the enhancement factor inversely scales with the wire radius, i.e. $FE \propto \frac{1}{R}$, so that a larger wire implies a smaller field enhancement. Therefore, we chose a value for the wire radius that would allow for a trade-off between these two counteracting effects. Regarding the wire interspacing, *2g*, the range of values to investigate has to be chosen depending on the spectral content of the input THz pulse, since according to Eq. (4.5), its value must be much smaller than the THz central wavelength. We stress the fact that this condition refers to the shortest wavelength in the THz pulse spectrum. Taking into account that most of the broadband THz sources, such as PCAs or second-order crystals, typically feature a central wavelength of λ_c ~ 400 μm, i.e. f_c ~ 0.8 THz, and a full-bandwidth of B_W ~ 3 THz [7,30], the shortest wavelength in their spectra is usually around λ_{min} = 100 μm (f_{max} = 3 THz). Therefore, we varied the wire interspacing in a range from 10 to 50 μm, with a step of 10 μm. By doing so, we could guarantee that the shortest wavelength was always longer than the chosen wire interspacing value. As for the waveguide length, while for the experimental characterization we employ a TWWG with L = 9 cm, for the numerical investigation we set a shorter length, i.e. L = 3.5 cm, since the investigation of such a long structure with an FDTD algorithm would require an unreasonable amount of computer physical memory, as well as too long of running times. Additionally, we want to highlight here that the main goal of this study was the retrieval of the shape of the temporal profile of the THz electric field at the TWWG output, which is usually achieved after a propagation distance that is as long as 10 times the central wavelength, i.e. ~ 4 mm for our study case. Therefore, the chosen waveguide length is an optimal value for a proper quantitative investigation of its spectral response. Furthermore, we set a central frequency of f_c ~ 0.8 THz and a full-bandwidth of B_W ~ 3 THz.

In order to investigate the role of the wire interspacing on the structure integration capability, we retrieved the TWWG transfer functions for all the simulated samples, so to compare them with the ideal behavior of a first-order temporal integrator, and establish how to obtain a better resemblance between the simulated and ideal curves. To this end, for each value of *2g*, we performed two simulations. In the first, we simulated the propagation of the input THz pulse in air. In more detail, we considered a Gaussian beam focused in air into a spot size of around 600 μm (waist radius), as dictated by the experimental conditions. The temporal waveform of the THz electric field was then retrieved at the focal plane of the Gaussian beam. Subsequently, we simulated the propagation of the same input THz pulse within the TWWG, and retrieved the temporal waveform at its output. This last step was carried out for each value of the wire interspacing. Finally, we retrieved the field spectra corresponding to the THz electric field waveforms, by using an FFT algorithm, and retrieved the TWWG spectral transfer function as follows:

$$T(f) = \frac{E_{TWWG}^{sub-\lambda}(f)}{E_{air}(f)} \tag{4.6}$$

Here, $E_{TWWG}^{sub-\lambda}(f)$ is the FFT-evaluated field spectrum corresponding to the waveform recorded at the TWWG output, and $E_{air}(f)$ is that corresponding to the waveform retrieved after propagation in air. From the comparison between the simulated transfer function and the ideal behavior of a first-order temporal integrator, not only we were able to properly investigate the influence of the wire interspacing on the TWWG spectral response, but also to choose an optimal value for the design of the structure. In particular, we anticipate here that, considering the condition imposed by Eq. (4.5), the behavior of the simulated structure tends to closely resemble that of an ideal first-order temporal integrator as the wire interspacing exhibits smaller values.

The results from the numerical investigation are shown in Figure 4.4. In particular, in Figure 4.4(a) we show the comparison between the amplitude of the simulated transfer functions (open circles) and the amplitude of the ideal transfer function of a first-order integrator (solid lines). In order to qualitatively evaluate the overlap between the two curves, i.e. how good the simulated transfer function follows the ideal *1/f* trend, we employed a statistical parameter, namely the coefficient of determination (CoD) [202]. Usually, this parameter is employed when a measured curve has to be compared with a predicted fitting function (in our case, *1/f*). Generally speaking, the CoD features non-negative values, in the range from 0 to 1, with the maximum value indicating a perfect overlap between the measured data and the fitting function. From this comparison, shown in Figure 4.4(a), we can observe that, overall, there is a good overlap between the simulated transfer function and the fitting function, as also highlighted by the high values of the CoD (> 0.96). Therefore, a TWWG with $2g < 50$ μm is suitable for the achievement of the temporal integration functionality. Nonetheless, it is worth to stress the fact that the smaller the wire interspacing, the larger the CoD, which reaches a value > 0.99 for the

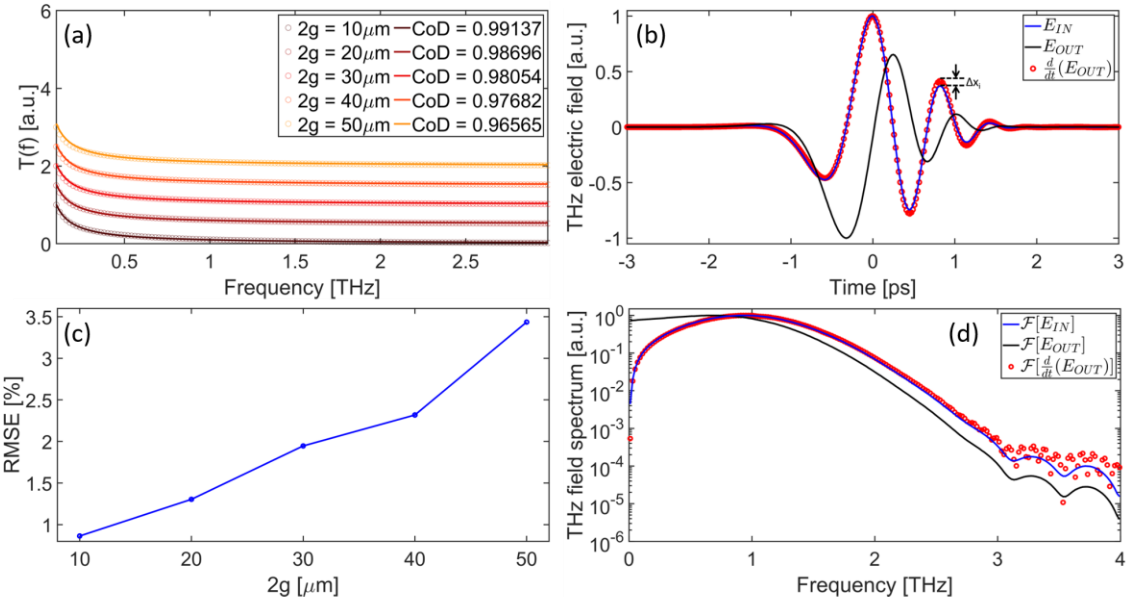

Figure 4.4. (a) Comparison between the simulated (open circles), evaluated as indicated in Eq. (4.6) and ideal transfer functions evaluated for different wire interspacing values, *2g*. The narrower the wire interspacing, the better the overlap between the simulated and the ideal curves, as also highlighted by the higher value of the coefficient of determination (CoD). (b) Simulated temporal waveforms recorded in air (blue line) and at the TWWG output (black line) for the case where *2g* = 24 μm. We also numerically-evaluated of the black curve and plot it in the same panel as red open circles. (c) Trend of the RMSE, evaluated as indicated in Eq. (4.7) as a function of *2g*, which is varied from 10 to 50 μm. The RMSE scales as a function of *2g*, further validating the data retrieved in the frequency domain and shown in (a). (d) Field spectra corresponding to the temporal waveforms shown in (b), where we can observe that the frequency components below 1 THz (black curve) experience a field enhancement caused by the sub-wavelength wire interspacing.

smallest value under study, i.e. *2g* = 10 μm, thus implying an almost perfect overlap between the simulated and the ideal transfer functions.

Summarizing, these preliminary results seem to confirm the validity of the condition imposed by Eq. (4.5). Even though a smaller wire interspacing results in a better integration capability of the TWWG, we must take into account the compatibility with the fabrication technique adopted for the TWWG. More specifically, the smallest wire interspacing, *2g*, that can be achieved depends on the smallest hole that is made on the surface of the PMMA holder, *D*, that at the same time allows to fit both the copper wires, with radius *R*, within it. In particular, we have that $2g = D - 4R$. We found that the diameter of such a hole is D ~ 530 μm, resulting in a wire interspacing of *2g* ~ 20 μm, since the wire radius is *R* = 127 μm. As a further step, we qualitatively evaluated the integration capability in the temporal domain. To accomplish this task, we numerically-evaluated the first-order temporal derivative of the waveform recorded at the TWWG output and analyzed its overlap with that retrieved after propagation in air. The quality of the overlap is evaluated by calculating the root-mean squared error (RMSE) between the two waveforms [203,204]. This statistical parameter is calculated by taking the square root of the mean squared discrepancy between the measured and expected data, that is [205]:

$$RMSE(x, \hat{x}) = \sqrt{\frac{1}{n}\sum_{i=1}^{n}(x_i - \hat{x_i})^2} = \sqrt{\frac{1}{n}\sum_{i=1}^{n}(\Delta x_i)^2} \qquad (4.7)$$

Here, *n* is the number of data points in the temporal waveforms, x_i are the observed values, and $\hat{x_i}$ are the expected ones, with Δx_i being the difference between them. The RMSE is the mean of the squares of the errors, and it always features non-negative values. Additionally, the lower the RMSE value, the better the resemblance between the two data plots. In our case, this implies a better integration capability of the designed TWWG. Moreover, in the ideal case, i.e. when the two curves are perfectly overlapped, the RMSE value is equal to 0. As an example, in Figure 4.4(b) we plot the simulated temporal waveforms after propagation in air (blue solid line) and at the TWWG output (black solid line), in the case where the wire interspacing is *2g* = 20 μm. We can observe a profound reshaping of the THz transients, due to the intrinsic response of the sub-wavelength TWWG. In the same plot, Δx_i defines the difference in the values of the temporal waveforms, in correspondence of the same temporal position, as also indicated in Eq. (4.7). We calculated this parameter for each investigated value of the wire interspacing, *2g*, and we show the obtained results in Figure 4.4(c). We can see that the RMSE value increases as a function of the wire interspacing. For the specific case illustrated in Figure 4.4(b), the retrieved RMSE value is low, i.e. around 2.7%, indicating a very good agreement between the measured and predicted data, as well as the possibility of employing the designed TWWG for the demonstration of the time-domain integration functionality. Finally, in Figure

4.4(d), we show the FFT-evaluated field spectra corresponding to the waveforms illustrated in Figure 4.4(b). We can observe an enhancement of the frequency components below 1 THz, as expected from the ideal transfer function of a first-order temporal integrator. We also show the spectrum of the numerically-evaluated first-order derivative as red open circles. By comparing the red and blue curves, i.e. the evaluated derivative and input spectra, we note a good overlap between them, in spite of the slight and expected discrepancies for frequencies above 2.5 THz. These preliminary results confirm the potential for the designed TWWG to perform the temporal integration of a broadband THz pulse sent at its input. Unfortunately, there are two crucial issues arising when employing the designed TWWG configuration with a sub-wavelength wire interspacing. First, it is impractical to efficiently couple the THz beam at the input of a waveguide featuring such a tiny wire interspacing. As a matter of fact, this would result in a very low coupling efficiency of the incoming THz field. Second, because of the sub-wavelength value of the wire interspacing at the TWWG output, the collection of the whole THz beam coupled from the TWWG in air is not trivial, due to the particularly strong diffraction of the THz beam, which ultimately results in a large divergence angle. These issues are addressed in more detail in the following notes.

4.3.2. COUPLING EFFICIENCY OF A SUB-WAVELENGTH TWO-WIRE WAVEGUIDE

In spite of the peculiar properties exhibited by a TWWG with a sub-wavelength wire interspacing, both at its input and output, such as the very tight confinement of the THz field in the air volume between the two wires, as also shown in Figure 4.3(c), it also suffers from a main drawback. More specifically, it hinders the efficient coupling of the incoming THz beam. This must be ascribed to the strong impedance mismatch existent between free-space, the characteristic impedance of which is $Z_0 = \sqrt{\frac{\mu}{\varepsilon}} \sim 377\ \Omega$ (typical value in air) and the TWWG input, the characteristic impedance of which, Z_{TTWWG}, changes as a function of both the wire interspacing and radius. In the latter expression, μ is the absolute vacuum magnetic permeability, and ε is the absolute vacuum dielectric permittivity. The coupling efficiency, which determines the amount of the incident electromagnetic energy coupled within a waveguide, is usually evaluated as follows [206]:

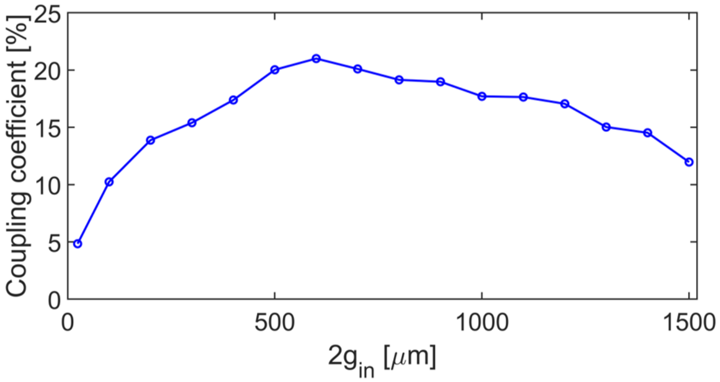

Figure 4.5. Coupling coefficient evaluated for the investigated waveguide, where the wire interspacing at the TWWG input is varied from $2g_n$ = 24 µm to $2g_{in}$ = 1.5 mm, with the wire radius being R = 127 µm, and the THz beam waist at the waveguide input being w_{THz} = 600 µm. Note that the coefficient is maximum when the wire interspacing, $2g_{in}$, is comparable with the THz beam waist. Also, its value is very low (~ 5%) for a sub-wavelength wire-interspacing.

$$C = \frac{4\beta_g \beta_m}{\left(\beta_g + \beta_m\right)^2} \frac{\left(\iint E_g(x,y) E_m(x,y)\, dxdy\right)^2}{\iint E_g(x,y) E_g(x,y)\, dxdy \iint E_m(x,y) E_m(x,y)\, dxdy} \tag{4.8}$$

Here, β_g and β_m are the propagation constants of the Gaussian beam (associated to the input THz beam) and the TWWG fundamental mode, respectively, E_g is the spatial distribution of the input THz beam, i.e. a Gaussian distribution, and E_m is that of the TWWG fundamental mode. The parameter defined in Eq. (4.8) indicates that the coupling coefficient is determined by the overlap between the spatial profiles of the THz beam propagating in free-space and that of the TWWG fundamental mode. Therefore, we can expect that it reaches a maximum when the wire interspacing is comparable in value with the waist of the THz beam focused at the TWWG input, as also reported in Refs. [124,206]. In our specific case, the waist of the focused THz beam at the TWWG input is around 600 µm, which is much larger than the wire interspacing at the TWWG input, i.e. $2g_{in}$ = 24 µm. As a consequence, we can expect that the coupling coefficient exhibits a very small value in the case under study. To further investigate this aspect and confirm this assert, we evaluated the coupling efficiency of the THz beam propagating in free-space to the TWWG input. Moreover, we set a test frequency of f_c = 1 THz, and a wire radius of R = 127 µm. We investigated the behavior of the coupling coefficient as the wire interspacing is increased from $2g_{in}$ = 24 µm to $2g_{in}$ = 1.5 mm. The results obtained from this numerical investigation are shown in Figure 4.5. From here, we can immediately observe that the value of the coupling coefficient (C), is maximum when the input wire interspacing ($2g$), is comparable with the beam waist of the input THz beam (w_{THz} = 600 μm). Moreover, for the case where $2g_{in}$ = 24 μm at the TWWG input, the coupling coefficient is around 5%, implying that most of the incident THz field would not be coupled in the waveguide. Furthermore, this issue would also affect the THz beam out-coupling, i.e. when the THz beam is coupled in air from the TWWG (see Section 4.3.3). A possible approach to partially overcome this issue is to employ a different waveguide configuration. In more detail, instead of using a "straight" geometry, i.e. the two parallel copper wires introduced in Chapter 2 and shown in Figure 2.2(d), we employed a tapered TWWG structure (hereinafter simply TTWWG), where the wire interspacing gradually decreases from its input to its output, thus forming a V-shape. A schematic of this revised configuration is shown in Figure 4.6. Let us explain in more detail why such a configuration would allow to overcome the aforementioned issue.

The THz beam propagating in free-space is coupled at the TTWWG input, which features a relatively wide wire interspacing, $2g_{in}$. Its value is either comparable or larger than the THz beam waist, w_{THz}. While propagating within the TTWWG, the THz field experiences an enhancement due to the fact that it is squeezed in an area that gradually decreases while propagating towards the waveguide output. For the design of the structure, we must choose carefully the proper value for the wire interspacing at the TTWWG input, so that $2g_{in} \gg 2g_{out}$, where $2g_{out}$ is the wire interspacing at the waveguide output. In this way, the designed structure would exhibit a much higher coupling efficiency at its input, as well as an enhanced impedance matching between free-space and TTWWG input. In order to explain this in more detail, let us take into consideration the theory of the transmission lines applied to the parallel wires' configuration. More specifically, let us consider the case of a variable wire interspacing, as it happens in our case, along the field propagation direction, i.e. z-axis in our case, to properly address this point. According to this theory, the waveguide exhibits a capacitance, $C(z)$, an external inductance, $L(z)$, and a characteristic impedance, $Z_{TTWWG}(z)$, per unit length, that can be analytically determined as follows [207]:

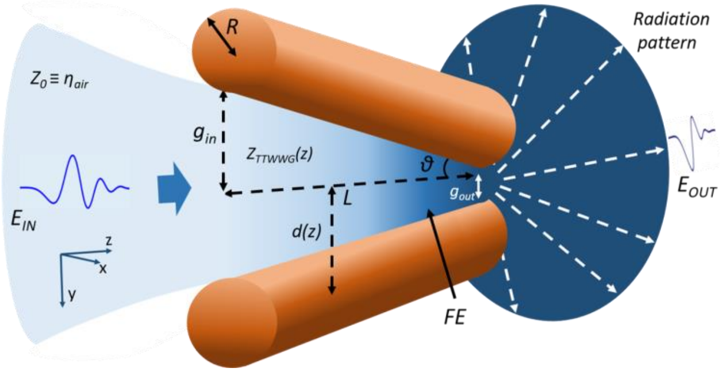

Figure 4.6. Schematic of the tapered two-wire waveguide (TTWWG) geometry. The THz beam is focused at the waveguide input featuring a relatively large wire interspacing (g_{in}). In this way, the impedance matching between free-space (Z_0) and the TTWWG [$Z_{TTWWG}(z=0)$] is greatly improved. While propagating towards the output, which exhibits a sub-wavelength wire-interspacing (g_{out}), the THz field experiences a significant field enhancement caused by its confinement in an ever-decreasing wire interspacing. The THz beam is then irradiated outside the TTWWG, with an extremely large emission angle, according to Bethe's diffraction.

$$C(z) = \frac{\pi\varepsilon}{cosh^{-1}\left(\frac{d(z)}{R}\right)} = \frac{\pi\varepsilon}{cosh^{-1}\left(\frac{g(z)+R}{R}\right)} \tag{4.9}$$

$$L(z) = \frac{\mu}{\pi} cosh^{-1}\left(\frac{d(z)}{R}\right) = \frac{\mu}{\pi} cosh^{-1}\left(\frac{g(z)+R}{R}\right) \tag{4.10}$$

$$Z_{TTWWG}(z) = \sqrt{\frac{L(z)}{C(z)}} = \frac{\eta}{\pi} cosh^{-1}\left(\frac{d(z)}{R}\right) = \frac{\eta}{\pi} cosh^{-1}\left(\frac{g(z)+R}{R}\right) \tag{4.11}$$

Here, $d(z) = g(z) + R$ is the semi-distance between the centers of the copper wires, with $g(z)$ being the half-value of the wire-interspacing at the coordinate z, as shown in Figure 4.6, $cosh^{-1}$ is the inverse function of the hyperbolic cosine, while ε, μ, and $\eta^2 = \frac{\mu}{\varepsilon}$ are the absolute dielectric permittivity and magnetic permeability, and the vacuum impedance, i.e. 377 Ω, respectively. From Equations (4.9) and (4.10) we can infer that, as the semi-wire interspacing, $g(z)$, tends to exhibit smaller values, $d(z)$ tends to R, thus implying that $\frac{d(z)}{R} \rightarrow 1$. In this case, the TTWWG impedance, $Z_{TTWWG}(z)$, exhibits a purely capacitive behavior, since $C(z) \gg L(z)$. Such a situation identifies the typical behavior of a device featuring an integration capability. As a matter of fact, we recall that the impedance associated to a capacitance is in the form $Z_C = \frac{1}{j\omega C} = \frac{1}{j2\pi f C}$, where ω is the angular frequency, and f is the frequency. Such an expression is indeed very similar to the transfer function of an ideal first-order temporal integrator, shown in Eq. (4.2). Moreover, in Figure 4.7 we plot the behavior of the TTWWG characteristic impedance as a function of the wire interspacing at its input, $2g_{in}$, as evaluated from Eq. (4.11). The black dashed line in the plot represents the value of the characteristic impedance in air, i.e. 377 Ω. From the plot, we can observe that the larger the wire interspacing at the TTWWG input, $2g_{in}$, the larger the impedance *seen* by the THz field propagating within the waveguide.

Additionally, a larger impedance implies a better matching between air and TTWWG input, so that a larger fraction of the THz field is actually coupled within the waveguide. In other words, if the mismatch between the two impedances (the difference between that in air and that at the TTWWG input) is large, there is an increase in the field reflection coefficient at the interface between air and waveguide input, since it is directly proportional to the difference between their characteristic impedances. In the case of a straight TWWG with a sub-wavelength wire interspacing, we can observe that the impedance mismatch would be too large, as it can also be inferred from the large difference in the values of the blue solid curve and black dashed line in Figure 4.7. Therefore, only a very small fraction of this transmitted field would be coupled in the waveguide, because of the low coupling coefficient (see Figure 4.5). The wire interspacing value, $2g_{in}$, chosen from Eq. (4.10), ultimately determines the TTWWG aperture angle, which is defined as follows:

$$\vartheta = tan^{-1}\left(\frac{g_{in} - g_{out}}{L}\right) \approx tan^{-1}\left(\frac{g_{in}}{L}\right) \qquad (4.12)$$

Here, tan^{-1} is the inverse tangent function, g_{in} and g_{out} are the semi-values of the wire interspacing at the TTWWG input and output, respectively, and L is the waveguide length. In Eq. (4.12) we can neglect the $2g_{out}$ value, because its value is much smaller than that at the input, i.e. $g_{out} \ll g_{in}$. From the plots in Figure 4.5 and Figure 4.7, we can infer that we have to choose a g_{in} value that is larger or equal to the THz beam spot size, i.e. twice its beam waist, i.e. $g_{in} \geq$

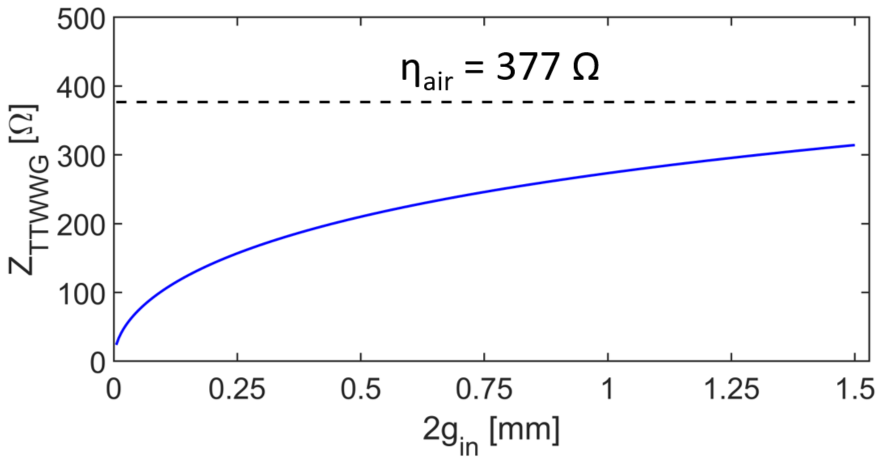

Figure 4.7. Trend of the characteristic impedance of the TTWWG, as evaluated from Eq. (4.11), as the wire interspacing at the TTWWG input is varied from $2g_{in}$ = 24 µm to $2g_{in}$ = 1.5 mm. The black dashed line represents the typical value of the air characteristic impedance, i.e. 377 Ω. Note that the impedance mismatch, i.e. the difference between the blue and black curves, worsens as the wire interspacing is decreased, thus implying that an ever-decreasing fraction of the THz field is actually coupled within the waveguide. As a consequence, a large value of the wire interspacing has to be chosen for the TTWWG input, so to enhance both the impedance matching between air and waveguide input, as well the coupling efficiency of the incoming THz beam.

$2w_{THz}$. Apart from the achievement of a better impedance matching between the THz free space and the TTWWG input, as well as an enhanced coupling efficiency, the choice of such a large value avoids the occurrence of spurious distortions in the THz electric field temporal profile, due to potential strong discontinuities. More specifically, we recall that the fabrication process for the TTWWG involves the use of PMMA holders at the two ends of a metallic bar, to ensure that the targeted wire interspacing between the wires can be obtained. Therefore, if the diameter of the hole drilled on the PMMA holder, D, is smaller than the THz beam size, then a portion of the latter would propagate through the PMMA holder, thus being partially absorbed and delayed. This would ultimately result in a distortion of the temporal pulse, which in turn might result in possible frequency dips in the spectral response, thus worsening the integration capability of the structure. Therefore, we chose an input wire interspacing of $2g_{in}$ = 1.1 mm, resulting in an aperture angle of $\vartheta \sim 0.4°$, as evaluated from Eq. (4.12) by taking into account a TTWWG length of L = 9 cm.

4.3.3. SUB-WAVELENGTH OUT-COUPLING DIFFRACTION

Another major issue that is related to the fabrication of a TTWWG with a sub-wavelength $2g_{out}$ value has to be addressed. More specifically, it involves the detection technique that has to be employed for the experimental characterization of the designed structure. As a matter of fact, after the propagation within the TTWWG, the THz field out-coupled in air from the waveguide output undergoes two main detrimental effects, which can be ascribed to the particularly small $2g_{out}$ value. The first issue is the significant impedance mismatch between the TTWWG output and air, as also mentioned in the previous section, which ultimately causes reflection losses at the waveguide output. The second and more significant issue is that, since the sub-wavelength output wire interspacing represents an effective new source for the THz far field, the emitted THz radiation undergoes a very strong diffraction. This behavior is very similar to what would happen in a PCA without the hyper-hemispherical silicon lens attached at the back of its substrate [2]. As a result, the out-coupled THz beam exhibits a very broad radiation pattern, as it can also be observed in Figure 4.6. Therefore, the gathering of the total power emitted by the TTWWG is quite unpractical. In order to evaluate the impact of this issue, we first need to highlight that, in the case of a generic THz source with such a tiny spot size, i.e. $2w_0 = 2g_{out} = 24$ μm (diameter), the Rayleigh diffraction rule does no longer apply. This is because the product of the wave-vector and the output wire interspacing is smaller than one [208], while Rayleigh diffraction rule applies when the product is larger than one. To better understand this point, in Figure 4.8 we show a two-dimensional map, where on the *x*-axis we show the central frequency of a THz pulse, on the *y*-axis we show the corresponding THz beam waist, while the color bar shows the product between the THz wave-vector (which is directly proportional to the THz pulse central frequency) and the THz beam waist. The white solid line represents the expression $k_{THz}w_{THz} = 1$. For all the cases below the white line, Bethe diffraction rule has to be applied, while Rayleigh diffraction rule can be applied for all the cases above the white line. For instance, by taking into account that the typical central wavelength of commonly-employed broadband THz sources, such as PCAs and second order crystals, fed by a 150-fs optical pulsed beam, is around 500 μm (corresponding to a central frequency of f_c =

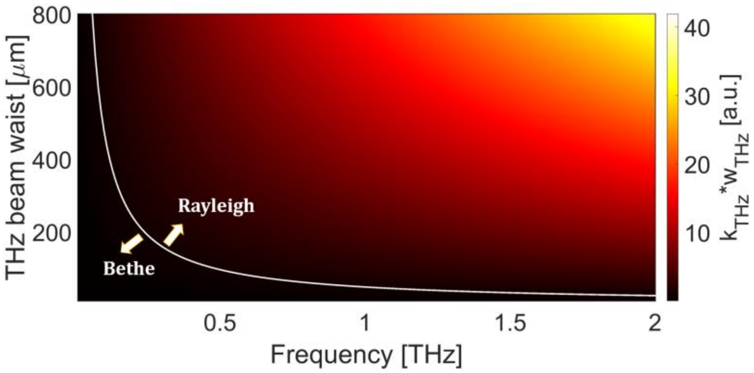

Figure 4.8. Two-dimensional color map indicating the value of the product between the THz wave-vector and the THz beam waist. The latter, in the case of a beam coupled in a tapered two-wire waveguide (TTWWG), is equal to the semi-value of the output wire interspacing, i.e. g = 12 μm. For this reason, Rayleigh diffraction rule does not apply anymore. The white line represents the condition $\boldsymbol{k_{THz}g_{out} = 1}$, being the threshold condition for the validity of the Rayleigh diffraction rule.

0.6 THz) [31,35], and by considering that the waist beam at the TTWWG output is equal to half the wire interspacing value, i.e. g_{out} = 12 μm, it is found that:

$$k_{THz} * g_{out} = \frac{2\pi}{\lambda_{THz}} g_{out} = 0.15 < 1 \tag{4.13}$$

In Eq. (4.13), k_{THz} is the wave-vector, λ_{THz} is the THz beam central wavelength, and g_{out} is the semi-wire interspacing at the TTWWG output. According to Bethe diffraction theory [163], the beam divergence depends on the second power of the THz pulse central wavelength. In more detail, the confocal parameter, z_B, which is defined as the distance from the focal plane at which the beam spot area doubles, can be written as follows:

$$z_B = \frac{k_{THz}^2 w_{THz}^3}{2} = \frac{2\pi^2 w_{THz}^3}{\lambda_{THz}^2} \tag{4.14}$$

By inserting all the values in Eq. (4.14), i.e. λ_{THz} = 500 μm and g_{out} = 12 μm, we find that z_B ~ 0.14 μm. Finally, we can evaluate the size of the THz beam after the out-coupling from the TTWWG as follows:

$$w(z) = w_{THz}\sqrt{1+\left(\frac{z}{z_B}\right)^2} \qquad (4.15)$$

In Eq. (4.15), z represents the propagation direction. The smaller the output wire interspacing, $2g_{out}$, the smaller the confocal parameter, z_B, the larger the diffraction angle of the THz beam after the out-coupling. Moreover, from Eq. (4.15) we can estimate that, even after a short propagation in air from the TTWWG output, the size of the THz beam is $w(z = 1\ cm) \sim 88$ cm. Therefore, no optical component would allow for the collection of the whole THz beam. Besides the power loss due to the only partial recover of the THz radiation, the strong beam diffraction would hamper the gathering of all the frequency components carried by the out-coupled THz pulse. For all of these reasons, far-field THz detection methods, such as FS-EOS [31] and PCAs [35], would result in the incorrect reconstruction of the THz temporal pulse, thus most likely hiding the effects of the temporal integration functionality. A very powerful solution that could be adopted for overcoming these issues is the recording of the THz electric field temporal profile via near-field detection techniques, which would allow for the retrieval of the waveform directly within the TTWWG. This task can be accomplished by exploiting a revised configuration of a well-known detection method, i.e. the air-biased coherent detection (ABCD) technique [209]. Before describing this revised configuration, it is worth describing the working principle of the standard ABCD technique.

4.4. AIR-BIASED COHERENT DETECTION TECHNIQUE FOR TERAHERTZ PULES

Generally speaking, commonly-employed detection methods based on centrosymmetric materials involve the up-conversion of the THz frequencies to the optical domain. The up-conversion is typically achieved via the frequency doubling of an optical probe beam, induced by the presence of the THz field. The resulting optical beam carries the information contained in the THz pulses, and can be easily recorded by employing standard optical detectors. The ABCD technique is based on the Terahertz-Field-Induced Second Harmonic (TFISH) generation [30], and it can be considered as a refinement of the air-breakdown coherent detection technique [210]. The TFISH can be explained as follows. The THz electric field can be regarded as static within a complete cycle of the optical wave, because the frequencies carried by a THz pulse are much smaller than those of an optical pulse, i.e. $\omega_{THz} \ll \omega_{opt}$. Therefore, when a THz beam is overlapped with the optical probe beam, in both time and space, a third beam, at approximately the second harmonic (SH) frequency of the probe beam, is generated [30,211]. The so-called TFISH beam, after a proper filtering of the remaining optical probe beam power, can be acquired by means of a photomultiplier tube (PMT). The electrical field, E_{SH}^{THz}, and the intensity, I_{SH}^{THz}, of the TFISH beam change proportionally to the THz electric field strength, E_{THz}, and its intensity, I_{THz}, respectively, according to the following two relationships:

$$E_{SH}^{THz} \propto \chi^{(3)} E_P E_P E_{THz} \tag{4.16}$$

$$I_{SH}^{THz} \propto \left(\chi^{(3)} I_P\right)^2 E_{THz}^2 \tag{4.17}$$

Here, E_P and I_P are the probe electric field and intensity, respectively, while $\chi^{(3)}$ is the nonlinear third-order coefficient of the gas (commonly air). From Equations (4.16)-(4.17), we can immediately observe that the TFISH is an incoherent process, i.e. the phase information cannot be retrieved, so that it is lost. In literature, it has been proposed that coherent detection schemes, i.e. those that are sensitive to the temporal profile of the electric field, thus allowing for the retrieval of the information about both amplitude and phase, can be implemented by inducing a beating between the THz beam with another locally generated SH beam, in what is usually referred to as an heterodyne scheme [209]. This additional SH beam can be obtained by superimposing an external bias electric field, E_{bias}, to the interaction region between the THz and optical probe beam. This is the working principle of the ABCD technique [212,213]. In more detail, both the probe and THz beams are focused in the air gap between two metal electrodes. The bias electric field is superimposed to the interaction region by applying a static bias voltage, V_{bias}, to the metal electrodes. In this case, the expression that allows to determine the SH intensity differs from that shown in Eq. (4.17), and results from the interference of two terms:

$$I_{SH}^{total} = \left(\chi^{(3)} I_P\right)^2 (E_{THz} \pm E_{bias})^2 = \left(\chi^{(3)} I_P\right)^2 (E_{THz}^2 \pm 2E_{THz}E_{bias} + E_{bias}^2) \tag{4.18}$$

The double sign in Eq. (4.18) depends on the orientation between THz electric field and that of the bias. The first quadratic term, E_{THz}^2, is related to the incoherent TFISH process, which exhibits the same repetition rate of the laser. The second quadratic term, E_{bias}^2, is a constant offset. Finally, the cross-term, $2E_{THz}E_{bias}$, is directly proportional to the THz electric field, and it is the one enabling the possibility to perform the coherent detection of the THz pulse. If the bias electric field is modulated with a modulation frequency that is different from the repetition rate of the THz electric field, the two quadratic terms in the right side of Eq. (4.18) can be rejected by carrying out the detection by using a lock-in amplifier, which is synchronized to the bias modulation frequency. Therefore, the actual readout signal can be expressed as follows:

$$I_{SH}^{total} \propto I_P^2 E_{THz} E_{bias} \tag{4.19}$$

Equation (4.19) ensures the coherent nature of the ABCD detection process. Due to the low dispersion of air, this detection technique allows to record THz fields exhibiting extremely large spectral bandwidths, i.e. $B_W > 10$ THz, with the only constraint being related to the finite temporal duration of the optical pulse.

4.4.1. TERAHERTZ ELECTRIC FIELD DETECTION WITHIN THE TAPERED TWO-WIRE WAVEGUIDE

We adapted the ABCD technique to be operated via our TTWWG, so to retrieve the THz electric field temporal profile within the waveguide. A sketch of the revised ABCD configuration is shown in Figure 4.9. We mainly show the detection path of the experimental setup employed during the investigation of the fabricated TTWWG. The THz beam is focused into the TTWWG by means of an off-axis parabolic mirror, whereas the optical probe beam, traveling through a hole drilled on the off-axis mirror, is focused inside the waveguide by means of a lens. In this way, the THz and probe beams propagate collinearly inside the TTWWG. The copper wires making up the TTWWG not only allow for the propagation of the fundamental TEM mode, but they also act as metal contacts for the delivery of the bias voltage to the waveguide. Additionally, the focal point of the probe beam can be adjusted so to generate the

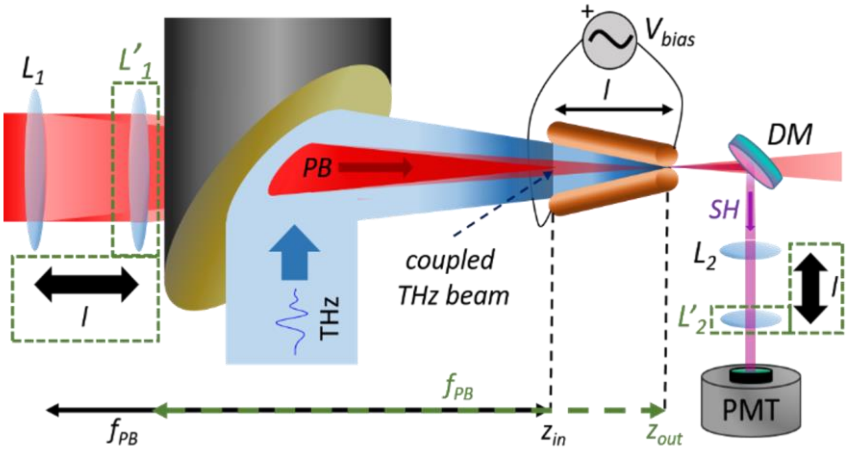

Figure 4.9. Schematic of the detection stage employed for the experimental investigation of the first-order temporal integrator. The TTWWG is placed at the focal point of an off-axis mirror. The optical probe beam is focused within the TTWWG by means of a lens (L_1), and then propagates collinearly with the THz beam. The position of the lens L_1 can be adjusted so to retrieve the THz electric field waveform at each point within the TTWWG. The SH beam emerging from the TTWWG, generated by the interaction between the THz and probe beams inside the TTWWG, which is biased at V_{bias}, is separated by the residual probe beam by means of a dichroic mirror (DM). Then, it is collimated by means of another lens, L_2, the position of which has to be adjusted accordingly to that of the focusing lens. Finally, a photomultiplier tube (PMT) acquires the SH beam intensity.

TFISH beam at different positions within the TTWWG, thus enabling the retrieval of the THz electric field at each of these positions.

This can be done by properly tuning the position of the focusing lens (L_1), while the position of the collimating lens (L_2) has to be adjusted accordingly, so that the TFISH beam can be collimated. Finally, after rejecting the residual probe beam by means of a dichroic mirror (DM), a PMT is employed to acquire the TFISH beam intensity. From Eq. (4.19) we can observe that the intensity of the TFISH beam acquired by the PMT shows a quadratic dependence on the probe beam intensity. As such, we can expect that the contribution to the TFISH intensity arises from a small region around the focal point of the probe beam within the waveguide. To validate this point, we analytically evaluated the expression in Eq. (4.19) for the specific case of the TTWWG employed in our investigation. We considered the dependence of all three terms in Eq. (4.19), i.e. the probe beam intensity, I_P, the bias electric field, E_{bias}, and the THz electric field, E_{THz}, on the propagation coordinate, z. By taking into account the TTWWG geometrical parameters indicated in Figure 4.3 and Figure 4.6, the analytical expression of the first two terms in the right-hand side of Eq. (4.19) can be determined as follows:

$$I_P(z) \propto \frac{I_0}{\sqrt{1+\left(\frac{z-z_f}{z_R}\right)^2}} \tag{4.20}$$

$$E_{bias}(z) \propto \frac{V_{bias}}{\sqrt{d^2(z)-R^2}\,cosh^{-1}\left(\frac{d(z)}{R}\right)} \tag{4.21}$$

In Eq. (4.20), I_0 is the peak intensity of the probe beam, z_f is the focal position of the probe beam inside the TTWWG, i.e. its relative coordinate to the TTWWG input, z_R is the probe Rayleigh length, which can be defined as the distance from the beam waist, along the propagation direction, where the beam radius is increased by a factor of $\sqrt{2}$. In more detail, it is expressed as follows:

$$z_R = \frac{\pi w_p^2}{\lambda_p} \tag{4.22}$$

Here, w_p is the waist of the optical probe beam, and λ_p is its wavelength. The waist size of the probe beam impinging on the focusing lens is d_{opt} = 3 mm. The waist beam size can be found as $w_p = \frac{1.22\lambda_p f_L M^2}{d_{opt}} \sim 20\ \mu m$, where f_L is the lens focal length (20 cm) and M^2 is the beam quality factor (~1.2). As a result, from Eq. (4.22) we can find that the Rayleigh length is z_R = 1.6 mm. As for the bias electric field expression, shown in Eq. (4.21), V_{bias} is the amplitude of the bias voltage applied to the copper wires, chosen as high as 150 V for the calculation. By replacing all the values in Eq. (4.21), i.e. V_{bias} = 150 V and R = 127 µm, and taking into account that the wire interspacing varies along the field propagation direction, from $2g_{in}$ = 1.1 mm to $2g_{out}$ = 24 µm, we retrieved a peak bias electric field of around 30 kV/cm at the TTWWG output. We anticipate here that the bias voltage cannot be increased beyond the chosen value, since this would result in a peak bias electric field, at the TTWWG output, that is larger than the air dielectric strength (~ 31 kV/cm) [214].

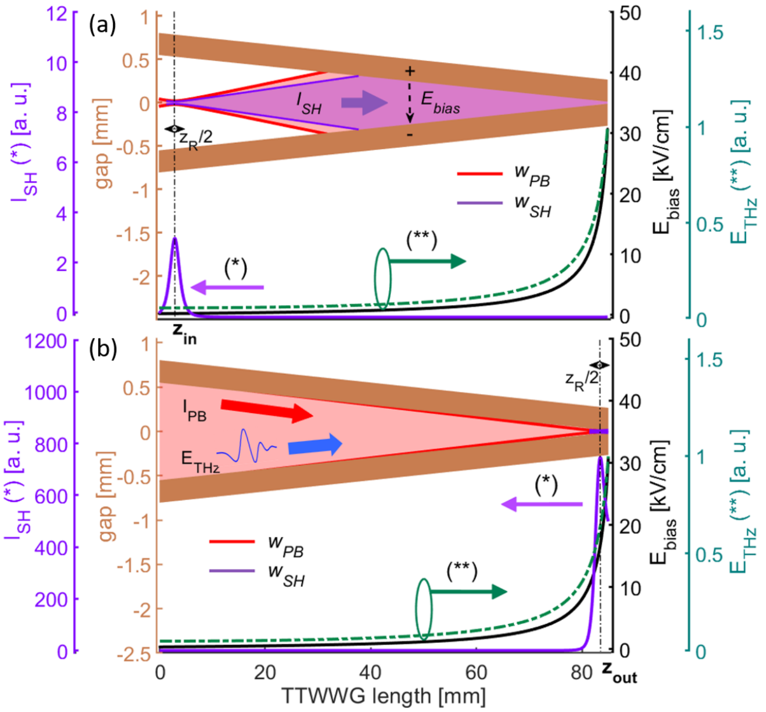

Figure 4.10. Mechanism of the TTWWG-integrated THz detection method, which gives rise to the SH beam, for the case where the optical beam is focused close to the waveguide input (a) or output (b). In both plots, the THz, probe, and SH beams propagate from left to right. Moreover, they are all polarized along the vertical axis. For sake of completeness, we also report the trends of the bias (black line) and THz (green line) electric fields along the TTWWG, as well as that of the SH beam intensity (purple line). The contribution to the total SH beam intensity is mainly generated in a region as wide as the optical beam Rayleigh length, z_R.

Finally, as far as the THz electric field is concerned, an analytical expression for its value is not easily accessible. To overcome this issue, we simulated the temporal evolution of a test THz pulse propagating inside the TTWWG by means of an FDTD algorithm. In particular, we considered a THz pulse exhibiting temporal and spatial characteristics identical to that employed in the numerical investigation discussed in Section 4.3.1. Additionally, for the accomplishment of the task, we considered the case of a Gaussian beam focused at the TTWWG input, so that we could also take into account the in-coupling effect of the THz beam into the TTWWG in the performed calculations. Moreover, we retrieved the absolute peak values exhibited by the THz electric field temporal waveform at the center of the interspacing between the two wires. The analytical results from these studies are shown in Figure 4.10. In particular, here we illustrate the actual dynamics of the probe beam propagation within the TTWWG. In more detail, we show the case of the optical probe beam focused close to (a) the TTWWG input, i.e. z_f = 3 mm, or (b) its output, i.e. z_f = 83 mm, via a 20-cm lens. It is worth pointing out that the waveguide length considered for this task is L = 8.5 cm. The orange stripes in both the plots represent the copper wires making up the TTWWG, while the red- and purple-filled areas highlight the propagation of both the probe and SH beams, respectively. Moreover, the SH beam intensity, bias and THz electric field within the waveguide are shown in the bottom part of both the figures as purple, black, and green solid lines, respectively. From the plots in Figure 4.10(a-b) we can immediately observe that the amplitude of the bias electric field remains below 1 kV/cm along half the waveguide length and then suddenly increases approaching the TTWWG output. The THz electric field shows a similar trend, with its amplitude monotonically increasing from the TTWWG input towards its output. On the other hand, the THz-induced SH beam intensity results to be noticeable only around the focal position of the probe beam (in a range equal to z_R), while it is totally negligible outside this region. Additionally, we can observe that this situation holds for any position of the probe focal point, z_f, as also highlighted in Figure 4.10(b), where the optical probe beam is focused close to the TTWWG output. This behavior guarantees that this near-field detection method allows for the monitoring of the THz electric field waveform evolution along the whole waveguide length, with a resolution as fine as half the probe Rayleigh length, z_R.

4.5. INVESTIGATION OF THE DEVICE INTEGRATION CAPABILITY

4.5.1. DEPENDENCE ON THE TERAHERTZ PULSE SPECTRAL BANDWIDTH

As highlighted in the previous sections, a THz field coupled within the TTWWG undergoes a significant enhancement once it reaches its output, which possesses a sub-wavelength wire interspacing. For a fixed value of $2g_{out}$, a shorter temporal duration of the input THz pulse implies a broader spectral content. Therefore, we can expect that the shape of the THz electric field waveform reaching the waveguide output deviates from the correct temporal integral of the input THz signal. This must be ascribed to the fact that, as the spectral content becomes broader, the shortest wavelength in it does no longer satisfy the condition imposed by

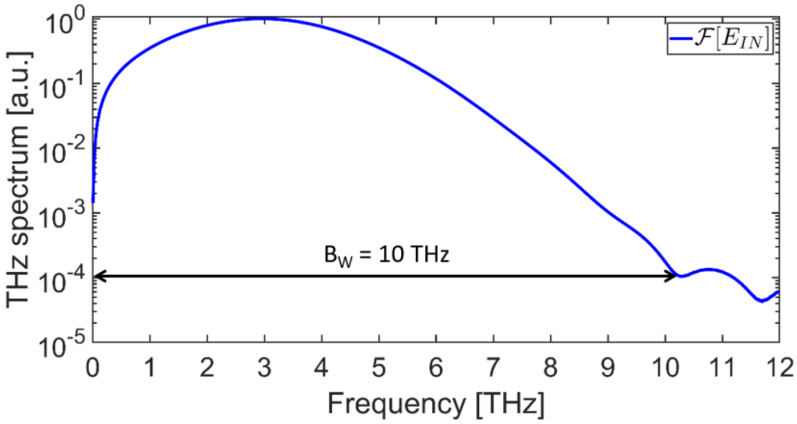

Figure 4.11. Simulated field spectrum of an ultra-broadband THz pulse, which features a central frequency of f_c ~ 3 THz, and a full spectral bandwidth of B_W = 10 THz, as indicated by the black arrow. The spectrum is normalized to its own maximum.

R [µm]	$2g_{in}$ [µm]	$2g_{out}$ [µm]	L [cm]	ϑ [deg]
127	1100	24	3.5	0.88

Table 4.1. Values chosen for the TTWWG geometrical parameters. In more detail, R is the wire radius, $2g_{in}$ and $2g_{out}$ are the wire interspacing at the waveguide input and output, respectively, L is the waveguide length, and ϑ is the aperture angle.

the THz pulse bandwidth. More specifically, as the full spectral bandwidth, B_W, is decreased, the value of the central frequency, f_c, decreases as well, while both the temporal duration of the THz pulse and the waist size of the Gaussian beam increase. Subsequently, we performed the simulation of the same THz pulse being coupled into the TTWWG under study, and we retrieved the temporal waveform at its output. In order to evaluate the integration capability of the TTWWG, we numerically-evaluated the first-order temporal derivative of the waveform retrieved at the waveguide output. Finally, we evaluated the overlap between the numerically-evaluated first-order derivative and the waveform retrieved after propagation in air, by calculating the RMSE value between the two waveforms, as shown in Eq. (4.7). All the aforementioned steps were performed for each value of the THz spectral bandwidth investigated in the numerical study. The results from this numerical investigation are shown in Figure 4.12, where we plot the calculated values of the RMSE as a function of the spectral bandwidth, B_W, of the input THz pulse. From the plot, we can immediately observe that the RMSE monotonically increases as a function of the THz pulse spectral bandwidth. This is a direct

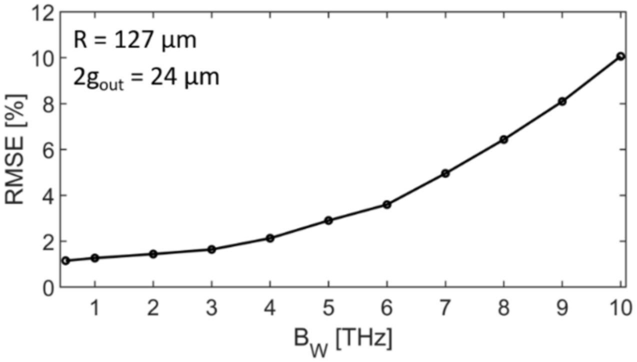

Figure 4.12. Root-mean squared error (RMSE) values, evaluated as indicated in Eq. (4.7), as a function of the spectral full-bandwidth, B_W, of the THz pulse used as input source for the numerical investigation, with the values of the TTWWG geometrical parameters being listed in Table 4.1. Note how the RMSE value monotonically increases as a function of B_W, as expected from the condition in Eq. (4.5), since the shortest wavelength in the spectral content decreases until becoming comparable in value with the output wire interspacing, i.e. $2g_{out}$ = 24 μm.

consequence of the condition imposed by Eq. (4.5), which has to be satisfied in order to achieve the targeted temporal integration functionality. Indeed, as the spectral bandwidth of the input THz pulse increases, the shortest wavelength in the spectral content exhibits smaller values. Moreover, for spectral bandwidths of B_W > 6 THz, the shortest wavelength, i.e. $\lambda_{min} < 50\ \mu m$, exhibits values that are comparable with the output wire interspacing. For instance, a THz pulse featuring a full bandwidth of B_W = 10 THz, as shown in Figure 4.11, exhibits a minimum wavelength of $\lambda_{min} = 30\ \mu m$, which is almost identical to the value of $2g_{out}$, so that the integration capability greatly worsens. This is also highlighted in Figure 4.12, where we can see that the RMSE value for the latter case is around 10%.

4.5.2. DEPENDENCE ON THE OUTPUT WIRE INTERSPACING

We further investigated the role played by $2g_{out}$ in the designed structure, in particular its influence on the TTWWG integration capability. The numerical investigation was carried following the same steps reported in the previous section. In particular, we chose a $2g_{out}$ value smaller than that used for the previous study, and a larger one, i.e. 10 and 40 μm, respectively. The values of the TTWWG geometrical parameters chosen for this investigation are listed in

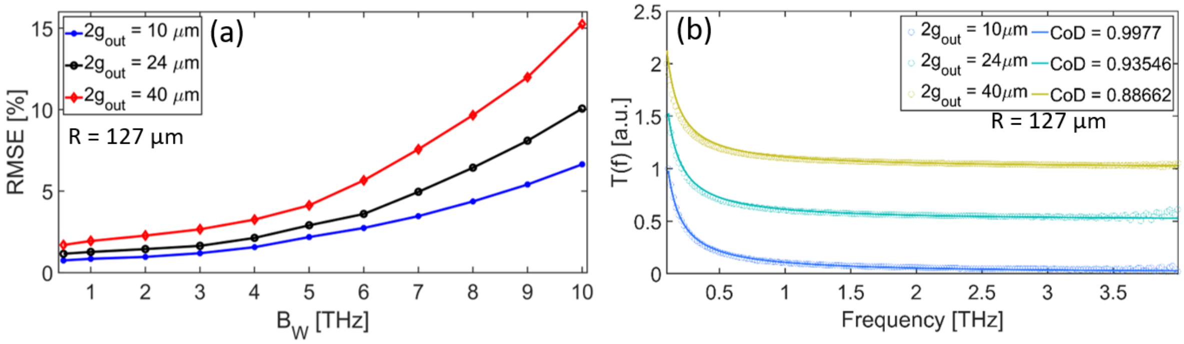

Figure 4.13. (a) Trend of the RMSE, evaluated as indicated in Eq. (4.7), as a function of the THz pulse spectral bandwidth, B_W, evaluated for three different wire interspacing values, i.e. 10 (blue line), 24 (black line), and 40 µm (red line). The wire radius is R = 127 µm, while the waveguide length is L = 3.5 cm. (b) Comparison between the simulated (open circles) transfer functions and the best hyperbolic fit (solid lines), evaluated as indicated in Eq. (4.6), for the same output wire interspacing values, and a fixed bandwidth of B_W = 4 THz. The CoD inversely scales with $2g_{out}$, implying that the simulated spectral response deviates from the ideal one as $2g_{out}$ increases. Curves in (b) are shifted along the y-axis for a better visualization.

R [µm]	$2g_{in}$ [mm]	$2g_{out}$ [µm]	L [cm]	ϑ [deg]
127	1.1	10	3.5	0.89
127	1.1	24	3.5	0.88
127	1.1	40	3.5	0.86

Table 4.2. Values chosen for the TTWWG geometrical parameters. Here, R is the wire radius, $2g_{in}$ and $2g_{out}$ are the input and output wire interspacing, respectively, L is the waveguide length, and ϑ is the waveguide aperture angle.

Table 4.2. Note that, among the TTWWG geometrical parameters, only the $2g_{out}$ value was varied, thus resulting in a simultaneous variation in the waveguide aperture angle, ϑ, defined as in Eq. (4.12). Moreover, to further investigate the effect of the output wire interspacing on the TTWWG integration capability, we also retrieved the spectral transfer function, for each $2g_{out}$ value, for a value of the THz pulse spectral bandwidth of B_W = 4 THz. The simulated spectral transfer function was retrieved as indicated in Eq. (4.6) and then compared with the *1/f* fitting function. The results from these numerical investigations are shown in Figure 4.13. In particular, in Figure 4.13(a) we show the trend of the RMSE value for the three different values of $2g_{out}$,

i.e. 10 (blue solid line), 24 (black solid line), and 40 μm (red solid line). Furthermore, the RMSE values have been retrieved for all the investigated THz pulse spectral bandwidths, B_W, in the range from 0.5 to 10 THz. From this plot, we can observe that the TTWWG integration capability worsens as $2g_{out}$ increases. More specifically, for full-bandwidths of $B_W < 5$ THz, the three configurations do not show a significant difference in the RMSE values, with the latter being smaller than 5% for all three cases. Conversely, as the bandwidth is increased, leading to a situation where $\lambda_{min} \sim 2g_{out}$, we can observe that the RMSE exhibits a large difference in value between the tree cases. This effect has to be ascribed to the fact that, for the case where $2g_{out} = 40$ μm, the condition imposed by Eq. (4.5) is no longer valid for spectral bandwidths larger than 7 THz, which corresponds to $\lambda_{min} \sim 43\ \mu m$. Moreover, in Figure 4.13(b) we plot the comparison between the simulated transfer functions (open circles) and the ideal *1/f* fitting curves (solid lines), for the same $2g_{out}$ values, while the spectral bandwidth was fixed at $B_W = 4$ THz. The agreement between the simulated and the ideal curves is evaluated by means of the CoD, the values of which are shown in the plot legend. We can observe that the CoD inversely scales with $2g_{out}$, thus further confirming the validity of the condition imposed by Eq. (4.5), as well as the simulated results shown in Figure 4.13(a).

4.5.3. DEPENDENCE ON THE WIRE RADIUS

Another important parameter that affects the TTWWG integration capability is the wire radius, *R*. As a matter of fact, we previously highlighted that its value was chosen as a trade-off between two counteracting effects. On the one hand, the enhancement factor occurring at the TTWWG output is inversely proportional to the wire radius [199,200], as also shown in Eq. (4.3), due to the fact that the THz spatial profile is squeezed into a smaller volume. On the other hand, the field enhancement is expected to exhibit a *1/f* dependence on the frequency only if $R \gg g_{out}$, as also indicated in Eq. (4.5). To validate this point, we performed a numerical investigation concerning the influence of the wire radius, *R*, has been varied during the investigation, so that the values of the other geometrical parameters are fixed. The chosen values for the wire radius, *R*, are listed in Table 4.3, together with the values set for the TTWWG geometrical parameters. Note that the values chosen for the wire radius are equal or very close

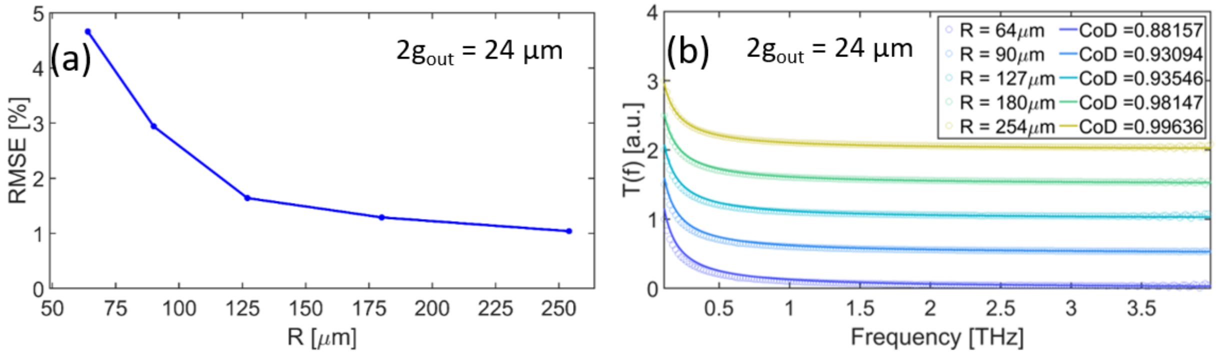

Figure 4.14. (a) Trend of the RMSE, evaluated as indicated in Eq. (4.7), as a function of the wire radius, *R*, for an output wire interspacing of $2g_{out}$ = 24 µm and considering an input THz pulse with B_W = 4 THz. The larger the wire radius, the smaller the RMSE. (b) Comparison among the simulated (open circles) simulated transfer functions, evaluated as in Eq. (4.6), and the best hyperbolic fit (solid lines), for the same radii values and spectral bandwidth in (a). The CoD decreases as a function of the wire radius, corresponding to a worsening in the TTWWG integration capability. Curves in (b) are shifted along the *y*-axis for a better visualization.

R [µm]	$2g_{in}$ [mm]	$2g_{out}$ [µm]	L [cm]	ϑ [deg]
64	1.1	24	3.5	0.88
90	1.1	24	3.5	0.88
127	1.1	24	3.5	0.88
180	1.1	24	3.5	0.88
254	1.1	24	3.5	0.88

Table 4.3. Values chosen for the TTWWG geometrical parameters. Here, R is the wire radius, $2g_{in}$ and $2g_{out}$ are the input and output wire interspacing, respectively, L is the waveguide length, and ϑ is the waveguide aperture angle.

to those commercially available for copper wires. As in the previous numerical investigation, the results of which are shown in Figure 4.13(b), the spectral bandwidth of the input THz pulse is set at B_W = 4 THz. The results obtained from the numerical investigation are shown in Figure 4.14. In more detail, in Figure 4.14(a) we compare the RMSE values for the different values of the wire radius, calculated as indicated in Eq. (4.7). As we can observe from this plot, the RMSE value diminishes as the wire radius increases, thus unveiling an improvement of the temporal integrator performance. This observation is consistent with the condition imposed by Eq. (4.5), and confirms that the TTWWG output waveform tends to resemble the shape of the ideal integrated function, as the radius becomes much larger than $2g_{out}$. Additionally, in Figure 4.14(b), we show the comparison among the simulated transfer functions, calculated as in Eq. (4.6), of the TTWWG different wire radii, along with the best hyperbolic fit curves. The resemblance between the simulated and ideal curves is evaluated by means of the CoD, the value of which is shown in the legend of the plot, for each case. As expected, the CoD decreases as a function of the wire radius, approaching a value of ~ 0.88 for the smallest wire radius value, thus further confirming the requirement imposed on the TTWWG geometrical parameters.

The results obtained from the reported numerical investigations strongly suggest that the integration functionality can be achieved for THz pulses exhibiting spectra as wide as 10 THz. Therefore, we carried out the numerical and experimental investigations of the structure in two THz spectral regimes, namely broadband and ultra-broadband [2]. For the first case, we considered the case of the optical rectification in a $LiNbO_3$ crystal [215], while in the other case we considered the THz pulses generated via a two-color plasma filament [136]. The reason behind these two choices is related to the different spectral emission of the THz pulses generated via these two techniques. On the one hand, the optical rectification in $LiNbO_3$ crystals provides a THz pulse with a broadband spectrum (B_W ~ 3 THz) and a relatively low central frequency (f_c ~ 0.5 THz), thus representing the perfect way to test the integration capability of the TTWWG. On the other hand, the ultrashort THz pulses emitted by the plasma filament cover a spectral content as wide as the full THz range, i.e. 0.1-10 THz, thus allowing us to experimentally investigate the spectral response of the device in the case of shorter wavelengths, in the order of a few tens of micrometers. We first performed the FDTD simulations of the structure as a support of the experimental investigation. For each source, we defined the input THz pulse with spectral and temporal features as shown in previous experimental works [40,216,217], so to closely reproduce the experimental conditions. Subsequently, we performed the experimental characterization of the designed TTWWG with the two aforementioned sources, using two different experimental setups, reported in the following notes.

4.6. CHARACTERIZATION WITH A LITHIUM NIOBATE SOURCE

4.6.1. NUMERICAL STUDY VIA FINITE-DIFFERENCE IN THE TIME-DOMAIN ALGORITHM

The first step of the TTWWG characterization was to perform a numerical simulation as a support for the experimental characterization. This is an important step, as it allows us to predict the behavior of the structure in terms of coupled and propagated THz pulse. As a result of the previous investigations, we set the following values for the TTWWG geometrical parameters: a wire radius of $R = 127$ µm, an input and output wire interspacing of $2g_{in} = 1.1$ mm and $2g_{out} = 24$ µm, respectively, a waveguide length of $L = 3.5$ cm, and a resulting aperture angle of $\vartheta \sim 0.9°$, as retrieved from Eq. (4.12). We also considered an input THz beam with a Gaussian spatial profile, which exhibits a beam waist of $w_{THz} = 600$ µm, a central frequency of $f_c = 0.8$ THz, and a spectral full-bandwidth of $B_W \sim 3$ THz, as retrieved from the experimental conditions. Moreover, the temporal duration of the input THz pulse was set at $\tau_{in} \sim 600$ fs. In particular, we considered a situation where the pulse is first focused in air to its diffraction-limited spot size. Then, we retrieved the temporal waveform of the THz electric field at the focal plane, and used it as a reference in the numerical investigation. In a second set of simulations, we computed the propagation of the same input THz pulse focused into the TTWWG, and retrieved the temporal waveform at its output, where the TTWWG wire interspacing is $2g_{out} = 24$ µm. We also numerically-evaluated the first-order temporal derivative of the waveform recorded at the TTWWG output. We chose to calculate the first-order temporal derivative due to the fact that differentiating the output waveform, rather than calculating the first-order time integral of the waveform recorded in air, shows the advantage of cancelling potential numerical artefacts, such as the superposition of a spurious offset value. The evaluation of the overlap quality between the calculated derivative and the input waveform allows for a qualitative investigation of the TTWWG integration capability. The results from the performed investigation are shown in Figure 4.15. In particular, in Figure 4.15(a) we illustrate temporal profiles of the THz electric field retrieved in air (blue solid line), at the TTWWG output (black solid line), and the numerically-evaluated first-order temporal derivative of the black curve (red open circles). In an ideal situation, if the integration

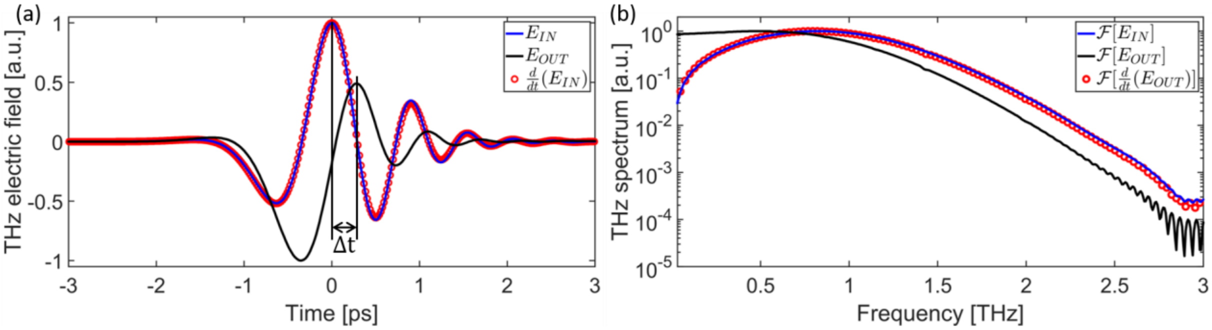

Figure 4.15. Simulated temporal profiles of the THz electric field (a) and corresponding field spectra (b) retrieved by employing an input THz pulse with characteristics identical to those of a THz pulse emitted by a $LiNbO_3$ source. The blue and black solid lines represent the input and output signals, respectively, while the red open circles represent the numerically-evaluated first-order temporal derivative of the black curve. In (a), *Δt* defines the temporal delay between the positive peaks of the input and output waveforms. All the curves are normalized to their own maxima.

functionality occurs at the waveguide output, the blue and red curves in Figure 4.15(a) should show a perfect agreement.

The first aspect we can observe from Figure 4.15(a) is the temporal delay, of around Δt = 280 fs, between the positive peaks of the blue and black curves. This delay is an effect of the time-domain integration, as it introduces a negative phase contribution, in the frequency domain, equal to $\Delta\phi$ = -85°, for the given central frequency of the input THz pulse, i.e. f_c = 0.8 THz. This value is very close to that induced by an ideal first-order temporal integrator, which is expected to be $\Delta\phi$ = -90°. In order to quantitatively evaluate the integration capability of the simulated structure, we evaluated the RMSE, as indicated in Eq. (4.7), between the red and blue curves, retrieving a value of *RMSE* = 1.64%. This low value confirms the capability of the designed structure to calculate the first-order temporal integral of a broadband THz pulse, with a good approximation. Moreover, we calculated the frequency field spectra corresponding to the retrieved temporal waveforms, via an FFT algorithm, and we plot them in Figure 4.15(b). We can immediately notice that the low-frequency portion of the black curve, i.e. below 0.5 THz, is strongly enhanced (of more than an order of magnitude) if compared to the input one (blue solid line). This is in agreement with Eq. (4.3). Furthermore, we can see a good overlap between the reference spectrum and that of the first-order derivative. Moreover, we can observe

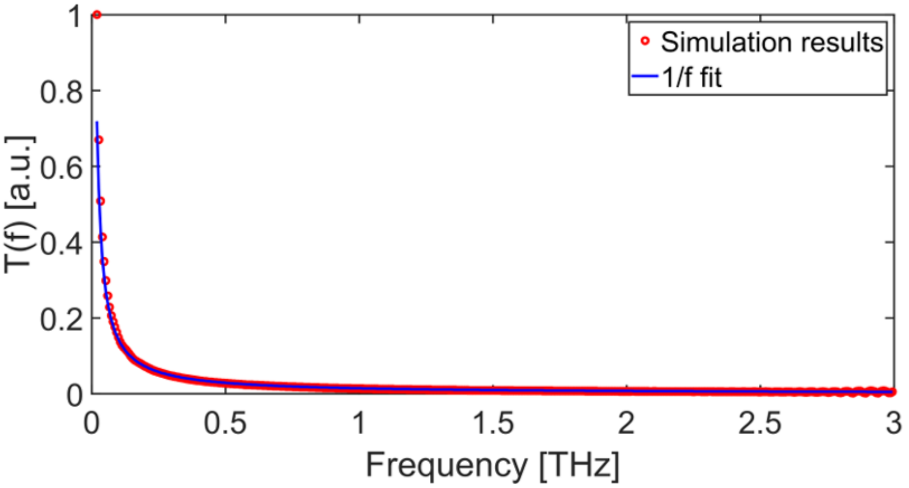

Figure 4.16. Comparison between the simulated transfer function (red open circles) and the ideal *1/f* response of a first-order temporal integrator. We can observe a good overlap between the two curves, which is also confirmed by the high value of the coefficient of determination (> 0.99).

a shift of the central frequency from f_c = 0.8 THz in the input spectrum to f_c = 0.5 THz in the output spectrum. This explains the longer pulse duration of the envelope of the output waveform, the FWHM duration of which is τ_{out} ~ 1.21 ps, longer than that of the input waveform, which is τ_{in} ~ 0.59 ps. For a better quantitative evaluation of the device integration capability in the frequency domain, we evaluated the simulated transfer function of the simulated structure, as indicated in Eq. (4.6), and fitted it with the ideal *1/f* response of a first-order temporal integrator. This comparison is plotted in Figure 4.16. We can notice that the two curves are very well overlapped, as also highlighted by the high value of the CoD, which is > 0.99. From the results obtained from this numerical investigation, we can infer that the designed structure is able to perform the first-order temporal integration of a broadband THz pulse with characteristics identical to those of a THz beam emitted by a $LiNbO_3$ source, with a good approximation. Before discussing the experimental results obtained from the characterization of the fabricated TTWWG, we provide a brief background on the optical rectification process in a $LiNbO_3$ crystal, as well as a brief introduction to the experimental setup employed for the experimental characterization.

4.6.2. TERAHERTZ GENERATION VIA OPTICAL RECTIFICATION IN ELECTRO-OPTIC CRYSTALS

Optical rectification (OR) is a second-order nonlinear effect taking place in non-centrosymmetric media that exhibit a non-zero second order susceptibility, i.e. $\chi^{(2)} \neq 0$. Essentially, OR can be recognized as a difference-frequency generation (DFG) process occurring between pairs of frequency components within the continuum bandwidth of the ultrashort optical pulses [2]. Generally speaking, these pulses exhibit a pulse duration in the femtosecond scale, and a continuum bandwidth as large as several THz. This nonlinear mixing results in a new EM wave, the spectral content of which is ideally centered close to the frequency axis origin, i.e. $f = 0$, and extends up to a few THz. From a mathematical point of view, the polarization vector can be expanded into a power series of the exciting electric field, E, as follows:

$$\boldsymbol{P}(\boldsymbol{r},t) = \chi^{(1)}(\boldsymbol{r},t)\boldsymbol{E}(\boldsymbol{r},t) + \chi^{(2)}(\boldsymbol{r},t) \colon \boldsymbol{E}(\boldsymbol{r},t)\boldsymbol{E}(\boldsymbol{r},t) + \ldots \tag{4.23}$$

Here, $\chi^{(1)}$ and $\chi^{(2)}$ are the first- and second-order susceptibility tensor, respectively. The second-order susceptibility tensor depends on the structure of the EO crystals. Many factors can affect the efficiency of the emitted THz radiation, such as the material composition, crystal orientation and thickness, material absorption, and phase matching [31]. Among these factors, the phase matching condition is the most important to take into account in a generic nonlinear process. For the case of optical rectification generating a THz wave, it requires the conservation of both energy and momentum, which can be described by the following relationship:

$$\begin{cases} \omega_{O1} - \omega_{O2} = \Omega_{THz} \\ k_{O1} - k_{O2} = k_{THz} \end{cases} \tag{4.24}$$

Here, ω_{O1}, ω_{O2}, k_{O1}, and k_{O2} are the frequencies and wave-vectors of the optical waves involved in the generation process, while Ω_{THz} and k_{THz} are the frequency and wave-vector of the generated THz wave. Ideally, when both the conditions in Eq. (4.24) are satisfied, the phase-matching occurs, which means that the waves involved in the OR process maintain the same speed while propagating, thus implying that the parent wave keeps generating the new beam through accumulation of in-phase contributions. When this happens, the maximum energy conversion efficiency is achieved [2]. However, this ideal condition is not simply observed in common materials, because of their inherent chromatic dispersion, which induces a phase-mismatch between the two propagating waves, as a consequence of the dependence of the refractive index on the frequency. Therefore, at a certain point along the propagation, the phase-mismatch leads to a back conversion of the new wave energy into that of the parent wave, eventually suppressing the new wave, in a periodic fashion. This effect is quantified in terms of the coherence length, which is defined as the interaction length for which the phase rotation reaches the value of π [33,218], and the generation process stops. The coherence length is defined, under a mathematical point of view, as follows:

$$L_C = \frac{\pi}{\delta k_O} \tag{4.25}$$

Here, $\delta k_O = k_{O1} - k_{O2}$, is the difference between the wave-vectors of the optical waves involved in the OR process. In order to obtain an efficient generation of THz radiation from a bulk crystal, its thickness has to be shorter than the coherence length, so that it is possible to achieve the highest conversion efficiency. Since the THz frequency is much lower than the optical ones, the relationships in Eq. (4.24) can be simplified by dividing the first equation by the second one, thus obtaining:

$$\frac{\delta \omega_O}{\delta k_O} = \frac{\Omega_{THz}}{k_{THz}} \tag{4.26}$$

Here, $\delta \omega_O = \omega_{O1} - \omega_{O2}$ is the difference between the frequencies of the optical waves involves in the OR process. The left-hand side term of Eq. (4.26) is essentially the group velocity of the optical wave, while that in the right-hand side is the phase velocity of the THz pulse. As such, we have that:

$$v_{g,opt} = v_{ph,THz} \tag{4.27}$$

Here, $v_{g,opt}$ is the group velocity of the optical beam, while $v_{ph,THz}$ is the phase velocity of the THz beam. Equation (4.27) implies that the phase-matching condition for the generation of the THz wave is satisfied when the group velocity of the optical beam is equal to the phase velocity of the THz beam. This condition is valid in the case of THz and optical beams collinearly propagating, which represents the simplest configuration to implement phase-matching. One of the most employed materials for the generation of THz radiation excited by femtosecond laser pulses with a central wavelength of λ_c = 800 nm, is ZnTe.

4.6.2.1. OPTICAL RECTIFICATION IN LITHIUM NIOBATE CRYSTALS

Another material that exhibits good properties for the efficient generation of THz waves is lithium niobate ($LiNbO_3$). This material shows a high optical transparency over a broad spectral range (350-5200 nm) and it possesses a strong optical nonlinearity [2]. More specifically, the large electro-optic coefficient (d_{33} = 31.5 pm/V) [2], makes it very attractive for the generation of THz pulses. Unfortunately, the material refractive index is very large at THz frequencies, which implies that it does not automatically satisfy the collinear phase-matching condition in the OR process. An ingenious way to overcome this issue is the steering of the THz radiation to the direction normal to the Cherenkov cone, i.e. the direction where the THz photons are emitted, by tilting the pulse front of the excitation optical beam with respect to the phase front, which is perpendicular to the direction of propagation of light [219]. In other words, a femtosecond laser pulse with a small beam size (compared to the central wavelength of THz radiation), acts like a point source that moves faster than the generated THz wave. In this way, the relationship between the optical beam group velocity and the THz beam phase velocity can be written as follows:

$$v_{g,opt}\cos(\vartheta_c) = v_{ph,THz} \tag{4.28}$$

Here, ϑ_c is the Cherenkov angle, a sketch of which is illustrated in Figure 4.17, and is defined as follows:

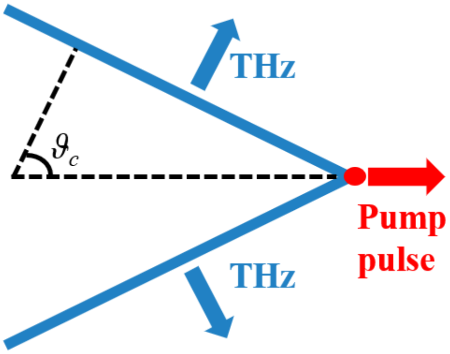

Figure 4.17. Schematic of the generation of THz pulses by using the tilted pulse front scheme for the optical rectification in a lithium niobate crystal, where ϑ_c is the Cherenkov angle.

$$\vartheta_c = \cos^{-1}\left(\frac{v_{THz}}{v_{opt}}\right) = \cos^{-1}\left(\frac{n_{THz}}{n_{opt}}\right) \approx 64° \tag{4.29}$$

Here, n_{THz} and n_{opt} are the refractive indices of $LiNbO_3$ at THz and optical frequencies, respectively. Lithium niobate is a very interesting nonlinear crystal that has been widely employed in optics because of its high nonlinearity. It possesses a higher band gap energy than other commonly-employed electro-optic materials, thus making it less susceptible to multiphoton absorption of the excitation laser pulses [2]. The latter usually results in an optical damage to the crystal, but also in the generation of free carriers in the nonlinear material that screen the THz generation (especially when using a high excitation laser power). The higher band gap energy allows $LiNbO_3$ crystals to hold a higher laser power, thus allowing for the generation of stronger THz pulses. Additionally, the robustness of the crystals to high laser power is increased by also doping the material with magnesium oxide ($MgO{:}LiNbO_3$) so that it can be employed for high power applications.

4.6.3. EXPERIMENTAL SETUP BASED ON OPTICAL RECTIFICATION IN A LITHIUM NIOBATE CRYSTAL

After performing the numerical investigation on the designed structure, the results of which are discussed in Section 4.6.1, we proceeded with the fabrication of the TTWWG. In particular, we followed the same steps reported in Section 2.2.2.1 [123], and we attached a PMMA holder to each end of the aluminum bar. One of the holders exhibited a ~ 1.6-mm-wide

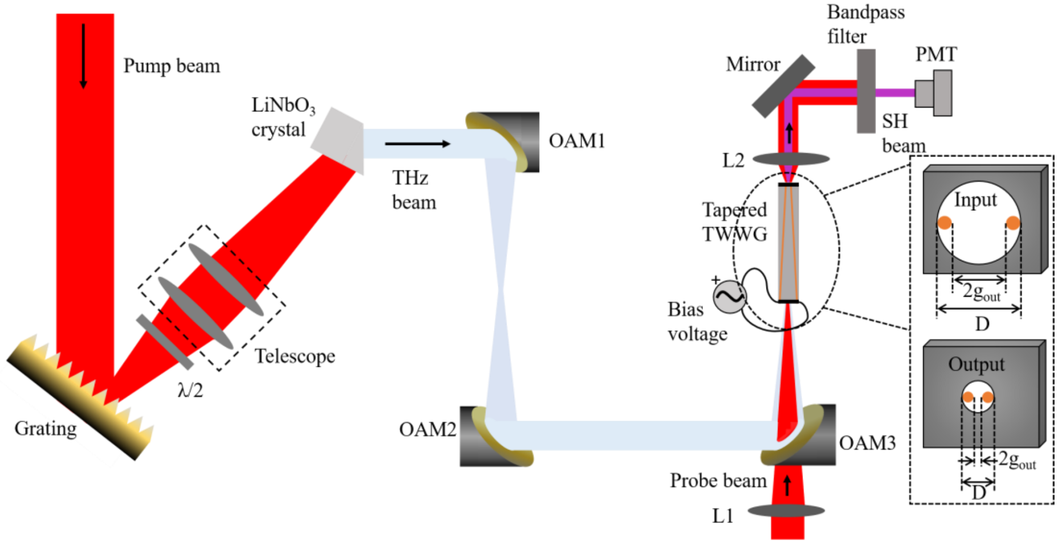

Figure 4.18. Schematic representation of the experimental set-up employed for the characterization of the fabricated TTWWG in the broadband regime. The THz pulses are generated by optical rectification in a $LiNbO_3$ crystal. The wave-front of the pump beam is tilted by means of a customized grating with 1800 grooves/mm. The THz beam is magnified by a factor of 10 and then focused at the TTWWG input via a 2-inch off-axis parabolic mirror. The probe beam is focused in the TTWWG via a lens with a focal length of 20 cm (L_1) to carry out the THz electric field detection. A voltage generator provides the required square-wave voltage to the TTWWG, so to bias the interaction region between the THz and probe beams. The SH beam emerging from the TTWWG is collected (L_2) and filtered from the remaining probe beam, before the acquisition by means of a PMT. In the inset we show a sketch of the PMMA holders with the holes drilled for guaranteeing that the wire interspacing is the designed one.

circular hole drilled on its surface, by means of a wire drill, while the other one had a ~ 0.53-mm-wide one. In this way, we could guarantee that the input and output wire interspacing were around 1.1 mm and 24 µm wide, respectively, as the same of the numerical investigation. A sketch of the PMMA holders with the hole drilled on their surface is shown in the inset of Figure 4.18. The experiment involves the use of a NIR pulsed laser beam (800 nm, 150 fs, 1.8 mJ, 1 kHz) generated by a Ti:Sapphire regenerative amplifier laser system. The pump and probe beams in the setup are obtained by means of a 90/10 beam splitter. For the generation of THz pulses, we employed a high-energy source relying on the OR process in a $LiNbO_3$ crystal [219]. For the achievement of the required phase-matching condition (see Section 4.6.2.1) between the optical and THz beams, we employed a tilted pulse front scheme. Specifically, we used a customized grating with 1800 grooves/mm to tilt the wave front of the optical pump beam by an angle of ϑ_c ~ 64°, as retrieved in Eq. (4.29), with respect to the propagation direction [219]. A half-wave plate is then placed after the grating, so to rotate the polarization of the optical pump beam from horizontal to vertical (phase-matching type II), thus setting the polarization of the pump beam to be parallel to the extraordinary axis of the crystal. Subsequently, the beam is demagnified by a factor of ~ 1.7 via a telescope, and is then focused onto the $LiNbO_3$ crystal for the generation of the THz wave, which is then collected by an off-axis parabolic mirror with a 1-cm focal length. The THz beam undertakes a 10-fold magnification through a second off-axis mirror with a 10-cm focal length and it is finally focused at the TWWG input by means of another off-axis mirror. In order to detect both the coupled and the travelling THz wave, we employed the revised configuration of the ABCD technique [209], the sketch of which is shown in Figure 4.9, implemented by applying the required square-wave voltage directly to the copper wires making up the waveguide. The optical probe beam can be focused to any coordinate along the TTWWG for the retrieval of the THz electric field, by adjusting the position of the focusing lens, which has a focal length of 20 cm (L_1). The TFISH signal [211], generated by the nonlinear interaction between the probe beam, bias and THz electric fields in the waveguide, emerging from its output, is then collimated by a fused silica lens with a focal length of 8.83 cm and is then sent through a 400 nm band-pass filter, with the goal of rejecting the residual optical probe power, and finally to a photomultiplier (PMT). The read-out signal is then acquired via a lock-in amplifier, which is synchronized to the bias modulation frequency (500 Hz, half the repetition rate of the laser).

4.6.4. EXPERIMENTAL RESULTS

As far as the experimental characterization of the fabricated TTWWG is concerned, we employed a TTWWG featuring a length of L = 9 cm. By taking into account the geometrical parameters of the TTWWG listed in Table 4.1, from Eq. (4.12) we obtained an aperture angle of ϑ ~ 0.4°. Despite its small dimension, such a value of the aperture angle allows for the improvement of the coupling efficiency of the THz beam within the waveguide, as well as an improved impedance matching between air and TTWWG. Because of the waveguide length and the size of the parabolic mirror body employed for the focusing of the THz beam into the waveguide, we employed a lens with a focal length of 20 cm, so that it would be possible to focus the optical probe beam to the targeted position along the TTWWG. An important detail to highlight before discussing the experimental results, concerns the retrieval of the reference waveform. For the task, we carried out the standard ABCD technique [209]. This choice was dictated by the fact that the tapered configuration does not allow to apply a bias voltage higher than roughly 150 V. Indeed, a larger value would result in a bias electric field higher than the air dielectric strength, i.e. ~ 31 kV/cm [214], at the waveguide output. However, the same value of the bias voltage would result in a bias electric field of $E_{bias} < 0.5$ kV/cm at the TTWWG input, where the wire interspacing is $2g_{in} = 1.1$ mm. Unfortunately, such a bias electric field is too small for carrying out the THz electric field detection at the TTWWG input. Therefore, for the task, we replaced the TTWWG with two metallic tips, separated by a 1.1-mm-wide air gap, equal to the chosen $2g_{in}$ value, and biased it with a 2 kV square-wave voltage, while the optical power of the probe beam was kept at the same value, i.e. 35 mW.

The results obtained from the experimental characterization of the TTWWG are shown in Figure 4.19. In more detail, in Figure 4.19(a) we show the THz electric field waveforms recorded in air (blue solid line) and at the TTWWG output (black solid line). Besides the clear difference in the evolution of the two THz pulses, we can also observe the occurrence of a temporal delay between their positive peaks. In other words, the waveform recorded at the TTWWG output is delayed with respect to that recorded in air. Such a temporal delay is an effect of the occurrence of the integration functionality at the waveguide output, and accounts for ~ 150 fs, which corresponds to a phase delay of 84° for the given central frequency of the input THz pulse, i.e. $f_c = 0.8$ THz. In order to confirm the occurrence of the integration functionality, we numerically-evaluated the first-order temporal derivative of the waveform recorded at its output (black line), and plotted it in the same panel as open red circles. Remarkably, this curve shows a fairly good agreement with the input THz waveform. To quantitatively evaluate the integration capability of the TTWWG, we calculated the RMSE between the evaluated derivative and the reference waveform, as indicated in Eq. (4.7). The obtained value of $RMSE = 2.4\%$ further confirms a fairly good agreement between the two curves. Moreover, the RMSE retrieved from the experimental results is very close to that

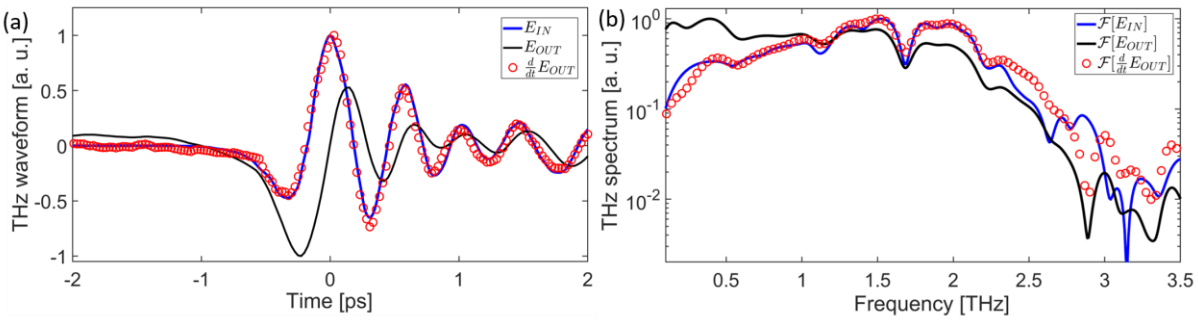

Figure 4.19. Experimental temporal profiles of the THz electric field (a) and corresponding field spectra (b) retrieved by employing a $LiNbO_3$ crystal as source for the generation of THz pulses. The blue and black solid lines illustrate the input and output signal, respectively, while the red curve represents the numerically-evaluated first-order temporal derivative of the black curve. All the curves in (a) and (b) are normalized to their own maxima.

obtained from the theoretical investigation, which we recall being *RMSE* ~ 1.7%. Furthermore, in Figure 4.19(b) we illustrate the FFT-evaluated spectra corresponding to the temporal waveforms shown in Figure 4.19(a). From this plot, we can observe how the output spectrum (black solid line) is significantly enhanced, compared to that of the input (blue solid line), for frequencies below ~ 1.1 THz. The spectral enhancement effect is actually expected from the interaction of the THz field with a sub-wavelength structure satisfying the condition imposed by Eq. (4.5), and further proves the potential of the fabricated TTWWG to perform the first-order temporal integration. The shift of the peak frequency towards lower values (from ~1.5 to ~ 0.5 THz) explains the longer pulse duration of the envelope of the output waveform, the FWHM duration of which is τ_{out} ~ 900 fs, longer than that of the input waveform, which is τ_{in} ~ 590 fs. Additionally, we evaluated the spectrum of the first-order temporal derivative (red open circles) in Figure 4.19(a), obtaining the curve in Figure 4.19(b) (red open circles). We can observe the good overlap between the latter spectrum and that of the input, which extends to a broad spectral window, up to ~ 2.5 THz. Finally, in Figure 4.20 we show the spectral response retrieved from the experiment, evaluated as indicated in Eq. (4.6), along with the best *1/f* fitting curve. The comparison between the two curves unveils a good overlap, as also highlighted by the relatively high CoD value, which is around 0.93. Both the theoretical and experimental results reported in these sections confirm the capability of the fabricated TTWWG to perform

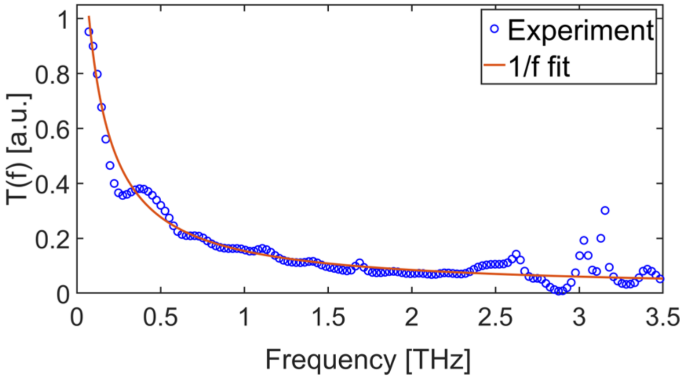

Figure 4.20. Comparison between the experimentally-retrieved transfer function (open blue circles) of the investigated TTWWG structure, and the best *1/f* fitting curve, typical of an ideal first-order integrator. From the comparison, we can see a relatively good agreement between the two curves, as also confirmed by the relatively high value of the coefficient of determination, which is ~ 0.93.

the first-order temporal integration of a broadband THz pulse, with spectral bandwidths of B_W < 4 THz.

4.7. CHARACTERIZATION WITH A TWO-COLOR PLASMA SOURCE

In order to characterize the spectral behavior of the TTWWG in the entire THz range and study and propose solutions to the limitations imposed by its geometry, we employed a source for the generation of THz pulses exhibiting a shorter temporal pulse duration, such as those emitted by a two-color plasma filament [38,220], generated by a 150-fs optical pulsed beam. Such a type of THz pulses exhibits a temporal duration as short as τ_{in} ~ 270 fs (FWHM), and a spectrum with a central frequency of f_c ~ 2 THz and a spectral full-bandwidth of B_W ~ 10 THz. As before, the numerical study was performed by using, as input source, a THz pulse that exhibits, in both the temporal and frequency domain, the same characteristics of that generated via the two-color plasma technique, which are reported in the previous works [40]. The numerical investigation was performed by exploiting the same FDTD algorithm as in the previous cases, and by following the same steps reported in the previous notes (see Section 4.3.1). We then performed the experimental characterization of the fabricated TTWWG, the process procedure of which is discussed in Section 2.2.2.1. As also highlighted in Section 4.5.1, we expect a slightly worse performance of the TTWWG, in terms of the integration capability, with a 10-THz-wide radiation, because of the condition on the TTWWG geometrical parameters imposed by Eq. (4.5). In particular, in this case the shortest wavelength in the spectral content barely satisfies the aforementioned condition. As a matter of fact, its value is λ_{min} = 30 μm for such a THz pulse, which is very close to that of the output wire interspacing, i.e. $2g_{out}$ = 24 μm.

4.7.1. NUMERICAL STUDY VIA FINITE-DIFFERENCE IN THE TIME-DOMAIN ALGORITHM

In order to simulate the behavior of the designed structure in the ultra-broadband regime, we employed a full-wave numerical solver employing the FDTD algorithm, which allows to solve the Maxwell's equations in all the spatial components (*x*, *y*, and *z*). Moreover, this algorithm allows for the retrieval of the information about the propagating THz electric and magnetic fields in the temporal domain. We retrieved the temporal profiles of the THz electric field in air, by assuming a Gaussian beam with a waist of w_{THz} ~ 150 μm focused in air and retrieving the temporal waveform at its focal plane. Subsequently we simulated the propagation of the same input THz pulse within the TTWWG and retrieved the corresponding temporal waveform at its output. We then calculated the corresponding field spectra by employing an FFT algorithm, and then the simulated spectral transfer function, as indicated in Eq. (4.6). This was then fitted with the ideal *1/f* curve of a first-order temporal integrator to evaluate the device performance, in terms of its integration capability, in the ultra-broadband regime.

The results obtained from this numerical investigation are shown in Figure 4.21. Specifically, in Figure 4.21(a) we display the temporal profiles of the THz electric field recorded in air (blue solid line), and at the TTWWG output (black solid line). We can immediately observe a delay between the peaks of the two temporal waveforms, which we believe can be ascribed to the integration functionality. The value of this delay is of ~ 110 fs, which corresponds to a phase delay of around 86° in the frequency. This value is very close to that induced by a first-order temporal integrator, i.e. 90°. To further investigate the device integration capability, we numerically-evaluated the first-order temporal derivative of the waveform recorded at the TTWWG output and we plot it in the same panel as red open circles. For a quantitative evaluation of the device integration capability, we calculated the RMSE, as indicated in Eq. (4.7), between the evaluated derivative and the input waveform, retrieving a

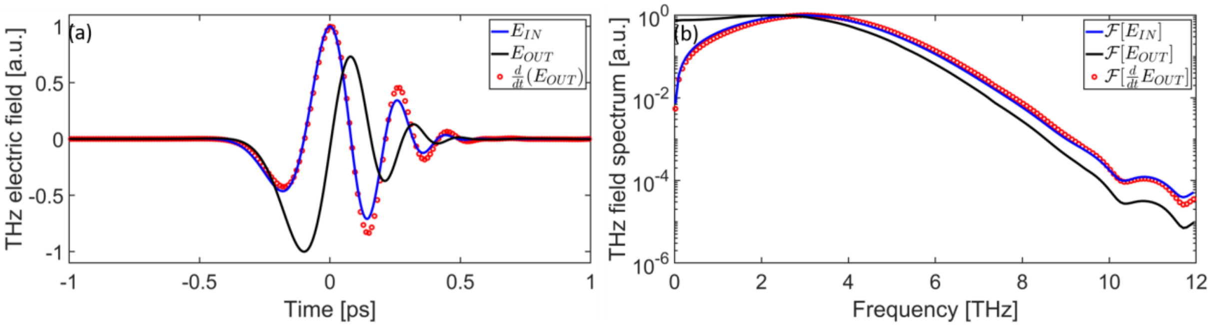

Figure 4.21. Simulated temporal profiles of the THz electric field (a) and corresponding field spectra (b) retrieved by simulating the TTWWG with an input THz pulse exhibiting temporal and spectral characteristics similar to those of the THz pulse emitted via two-color plasma technique. The blue and black solid line represent the input and output signal, respectively. Moreover, we numerically-evaluated the first-order temporal derivative of the black curve (both in the time and frequency domain), and we show it as red open circles in both the plots. All the curves are normalized to their own maxima.

value of *RMSE* ~ 10%. This value implies a much worse integration capability of the designed TTWWG, with the THz pulse under study. This aspect is also highlighted by the noticeable difference between the two waveforms in the plot (blue and red curves), such as different amplitude of the pulse lobes. Once again, such an effect had to be expected, by taking into account the constraint on the TTWWG geometrical parameters, shown in Eq. (4.5), since in this case $\lambda_{min} \approx 2g_{out}$. Furthermore, in Figure 4.21(b), we show the FFT-evaluated field spectra corresponding to the temporal waveforms shown in Figure 4.21(a). In this plot, we notice the significant enhancement of a fairly large portion of the output spectrum (black curve) with respect to that of the input (blue curve), for frequencies below 2 THz. We also recall that the field enhancement factor, expressed as in Eq. (4.3), scales with the frequency, which explains the reshaping of the spectral content, which shifts the central frequency from f_c ~ 3 THz to f_c ~ 2 THz. In the temporal domain, this translates in a different FWHM temporal duration of the two THz pulses, i.e. τ_{in} ~ 270 fs and τ_{out} ~ 400 fs (FWHM).

Moreover, the relatively large RMSE value is also evident in the frequency domain, where we can observe a difference between the input spectrum and that of the evaluated derivative (blue and red curves, respectively), especially in the high-frequency portion, i.e. $f >$ 6 THz. The transfer function, evaluated as in Eq. (4.6), is shown in Figure 4.22, where it is also fitted with an ideal *1/f* curve (red solid line). From this plot, we can observe an overall agreement

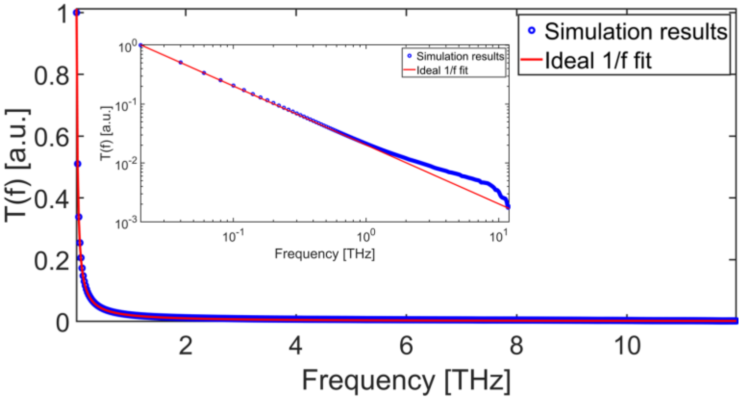

Figure 4.22. Comparison between the simulated transfer function (blue open circles) and the fitting *1/f* function typical of a first-order temporal integrator. In the inset, we illustrate the same plot in a logarithmic scale, to highlight the difference between the simulated (blue open circles) and ideal (red solid line) curves, for frequencies above 5 THz.

between the two curves, as also confirmed by the fairly large value of the CoD, i.e. *CoD* ~ 0.89. This value is lower than that obtained in the case where the TTWWG was characterized with a broadband THz pulse, i.e. that generated by employing a $LiNbO_3$ source, thus implying a worse performance. The reason behind this smaller value can be inferred in the inset of Figure 4.22, where we plot the same curves in logarithmic scale, from which we can notice the difference in the two trends. We recall that a hyperbolic function in a linear scale becomes a linear function in a logarithmic scale. From this plot we can observe a difference in the two trends, which becomes larger for frequencies above 5 THz.

In the following notes, before presenting and discussing the results obtained from the experimental characterization of the fabricated TTWWG, we provide a brief theoretical background on the generation technique employed for the sample characterization and we then introduce the experimental setup employed for the study.

4.7.2. ULTRA-BROADBAND TERAHERTZ GENERATION VIA TWO-COLOR PLASMA

As previously highlighted in this dissertation, the generation of THz pulses with a very short temporal pulse duration, which corresponds to a spectral content as wide as 10 THz, has been the main focus of several research groups worldwide, due to the many interesting applications these pulses could be employed for [221,222]. The emission of THz radiation from plasma filaments was first observed in 1993 by Hamster *et al.* [223]. With the further development of energetic femtosecond laser sources, this technique has been significantly improved. Years after that, it was proposed to mix the fundamental femtosecond laser pulse with its second harmonic, which resulted in an enhanced generation of THz pulses, as well as in the emission of a highly directional THz beam [59]. The THz radiation emitted by a two-color plasma filament is caused by three different contributions: four-wave rectification, tunneling ionization (resulting in plasma photocurrents), and longitudinal and transversal plasma waves. As an energetic, ultrashort laser pulsed beam is focused in air, its intensity peak increases while propagating towards the focal plane. As a result, the refractive index of air is primarily modulated because of the Kerr nonlinearity. This effect causes the layer of air, where the beam propagates, to behave as a focusing lens, thus resulting in an acceleration of the beam focusing, named self-focusing effect. However, as the pulse intensity keeps raising, it can reach the air breakdown threshold, beyond which it starts to ionize air and generates a plasma spark. In the plasma, several higher nonlinearities are recognized to take place, such as the peak intensity clamping to the breakdown threshold. This is due to the fact that the energy of the beam is now utilized to create a larger number of photocarriers in the plasma volume, which enlarges along the transverse direction, while greatly preventing the further increase of the pulse intensity. This effect is called plasma defocusing. Therefore, these two concurrent effects counterbalance each other, resulting in the generation of a plasma filament. In two-color plasma, the fundamental pulse is first traveling through a type-I β-barium borate (BBO) crystal while is being focused, so to generate an SH beam, which shares the same focal plane of the fundamental beam. Moreover, the rotation angle of the BBO crystal can be tuned so to achieve the proper temporal coherence between the two beams. In theory, the THz radiation intensity is maximized when the polarizations of the fundamental and SH beams are parallel, which however does not correspond to the maximum SH generation efficiency in the BBO crystal, because of the type-I phase matching. Therefore, a trade-off has to be found by playing with both the angle and the longitudinal position of the BBO crystal along the focusing path [224–226]. The efficiency of the generation of THz pulses achieved by employing this technique reaches very high levels, i.e. ~ 10^{-3}-10^{-2}.

4.7.3 EXPERIMENTAL SETUP BASED ON A TWO-COLOR PLASMA SOURCE

For the experimental investigation of the integration functionality induced by the TTWWG configuration exhibiting the geometrical parameters listed in Table 4.1, we employed an experimental setup where the detection scheme is the same shown in Figure 4.18, while the generation technique employed is the two-color plasma technique. A schematic of the employed setup is shown in Figure 4.23. We employed a train of short NIR pulses (800 nm, 150 fs, 1.8 mJ, 1 kHz) generated by a Ti:Sapphire regenerative amplifier laser system. The pump and probe beams are obtained by employing a 90/10 beam splitter. For the generation of the ultra-broadband THz pulses, the optical pump beam is focused via a 4-inch off-axis parabolic mirror along with its second harmonic, which is generated from a BBO crystal. The crystal is placed shortly before the focal plane of the off-axis mirror. The residual pump and SH beams are then filtered out by using a high-resistivity 0.5-mm-thick silicon plate, which acts as a long-pass filter. The THz beam is then focused at the TTWWG input by means of a 2-inch off-axis parabolic mirror. The optical probe beam is focused at the targeted position within the waveguide by means of a lens with a focal length of 20 cm, because of the waveguide length (L = 9 cm) and the body size of the parabolic mirror. Briefly, the TFISH signal generated within the waveguide and emerging from its output is first collimated by means of a fused silica lens with a focal length of 8.83 cm and then sent through a 400 nm band-pass filter, with the goal of rejecting the residual probe beam and transmitting only the TFISH signal. Finally, the TFISH beam is sent to a PMT. The signal recorded by the PMT is then acquired by means of a lock-in amplifier, which is synchronized to the bias modulation frequency, i.e. 500 Hz.

4.7.4. EXPERIMENTAL RESULTS

We started the experimental characterization by measuring the spot size of the optical probe beam at its focal plane, which is $w_{opt} \sim 40$ μm in diameter and corresponding to a Rayleigh length of $z_R \sim 1.6$ mm, considering a beam quality factor of $M^2 \sim 1.2$, as evaluated from Eq. (4.22). This implies that the THz electric field waveforms retrieved between two points that are closer than $z_R/2$ do not show any appreciable difference in terms of both amplitude and shape,

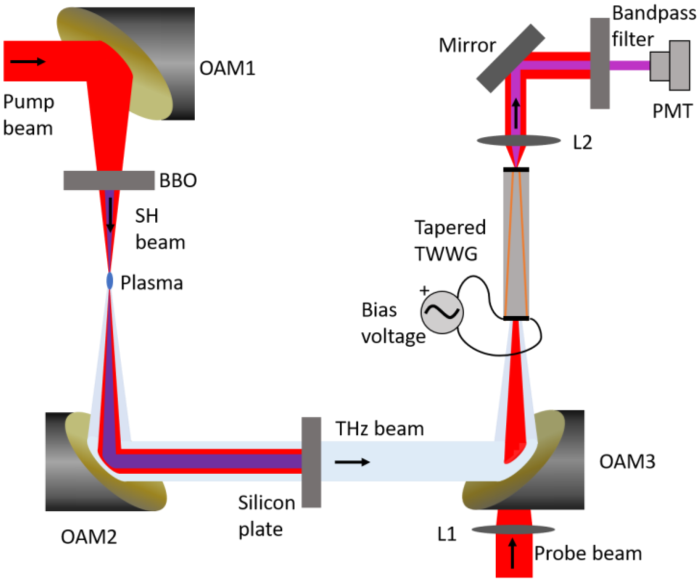

Figure 4.23. Schematic of the experimental setup employed in the ultra-broadband regime. THz pulses are generated via a two-color plasma source, achieved by mixing the pump beam and its second harmonic, obtained from a BBO crystal in the air-plasma channel. A high-resistivity 0.5-mm-thick silicon plate is used to separate the THz beam from the residual optical beams. The THz beam is then focused within the TTWWG through a 2-inch off-axis mirror. The detection stage is the same of that shown in Figure 4.18.

as also mentioned in Section 4.4.1. Moreover, as the optical probe beam is focused at the waveguide input, its diameter is still larger than the 1.1-mm wire interspacing at the TTWWG input, thus resulting in a partial loss of power before reaching the waveguide output. Nonetheless, this loss in the probe beam power does not significantly affect our experimental investigation, since we are mostly interested in the change of the THz waveform shape while propagating from the TTWWG input to its output. Following the same procedure adopted in the case of the TTWWG characterization with the broadband $LiNbO_3$ source, we first employed the standard ABCD technique to retrieve the temporal profile of the THz electric field that we then considered as reference. Subsequently, we placed the TTWWG so that the focal plane of the THz beam would coincide with the waveguide input, and applied the bias voltage to the copper wires. We then retrieved the temporal profile of the THz electric field at the TTWWG output, by employing the revised configuration of the ABCD technique discussed in Section 4.4.1. We then evaluated the corresponding field spectra by means of an FFT algorithm, and then

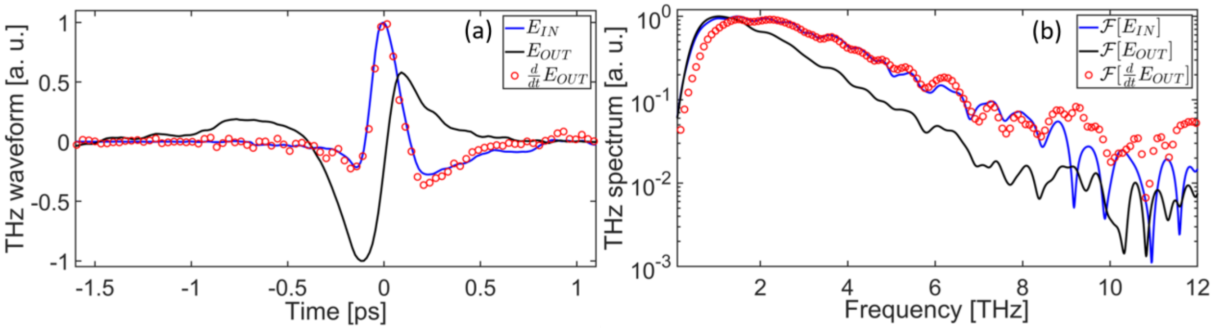

Figure 4.24. (a) Experimental temporal and spectral curves retrieved by employing a two-color plasma source and the experimental setup shown in Figure 4.23. In all the panels, the blue and black solid lines indicate the input and output signal, while the red open circles represent the numerically-evaluated first-order temporal derivative of the black curve. Both the temporal and spectral curves are normalized with respect to their own maxima.

evaluated the spectral transfer function, according to Eq. (4.6). The results obtained from the TTWWG experimental characterization are shown in Figure 4.24. In particular, in Figure 4.24(a) we show the comparison between the temporal profile of the THz electric field retrieved with the standard ABCD technique (the input waveform, shown as blue solid line), and that retrieved at the TTWWG output (black solid line). From this plot, we can observe a clear time delay between the positive peaks of the two temporal waveforms. The value of this delay is of ~ 110 fs, corresponding to an average phase delay of -82°, which is fairly close to the -90° contribution introduced by an ideal first-order temporal integrator. The phase delay retrieved in this case study is also slightly smaller than that obtained in the case of THz pulses generated via OR in a $LiNbO_3$ crystal, thus implying a slightly worse integration capability with the employed input THz pulse. This is in very good agreement with the condition on the TTWWG geometrical parameters imposed by Eq. (4.5). In order to better evaluate the integration capability of the fabricated structure, we also numerically-evaluated the first-order temporal derivative of the waveform retrieved at the waveguide output (black solid curve), and we show it in the same plot as red open circles. It is worth mentioning that the numerical differentiation has the main effect of amplifying the noise level of the original waveform, which explains why the evaluated first-order temporal derivative appears much noisier than the other two curves. Nonetheless, we observe that the first-order derivative and the input waveform (red and blue curves, respectively)

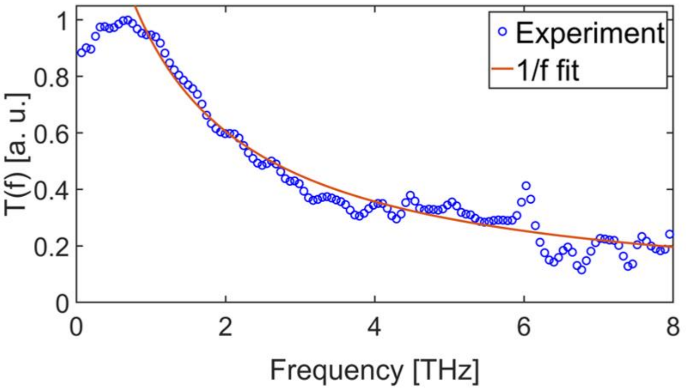

Figure 4.25. Comparison between the experimentally-retrieved transfer function (blue open circles) and the typical *1/f* behavior of an ideal first-order temporal integrator. The two curves show a fairly good agreement, especially in the frequency range from 1 to 7 THz, while the overlap greatly worsens for the frequencies outside of this range.

show a good agreement. To quantitatively investigate the performance of the device, we calculated the RMSE between the evaluated derivative and the input waveform, as indicated in Eq. (4.7), obtaining a value of $RMSE \sim 12\%$. This worsening of the TTWWG performance, if compared to the case where a $LiNbO_3$ crystal was employed as THz source, has to be ascribed to the intrinsic frequency response of the TTWWG, which had been originally designed for an optimum operation with longer THz pulses, i.e. featuring narrower bandwidths, below 4 THz. To better understand this point, we evaluated the field spectra corresponding to the waveforms shown in Figure 4.24(a), and we plot them in Figure 4.24(b). We stress the large difference between the input (blue solid line) and output (black solid line) spectra. In more detail, the output spectrum features a rich low-frequency content and a de-emphasis of the higher portion of the spectrum, with respect to the input case. This is an expected behavior due to the field enhancement induced by the sub-wavelength wire interspacing at the waveguide output. Moreover, while the spectral emission of the plasma source extends to almost 10 THz in air, the temporal pulse detected at the TTWWG output exhibits a bandwidth as large as $B_W \sim 9$ THz only. We recall that the field enhancement factor scales with the frequency, thus explaining the reshaping of the spectral content, which moves the central frequency from 1.8 THz (input spectrum) to ~ 1 THz (output spectrum). In the temporal domain, this translates to a FWHM pulse duration that lengthens from $\tau_{in} \sim 270$ fs to $\tau_{in} \sim 420$ fs. Moreover, we evaluated the spectrum corresponding to the evaluated first-order derivative, and we display it as red open circles in Figure 4.24(b). We can observe a good overlap between the red and blue curves, especially for frequencies between 1 and 8 THz. However, the overlap greatly worsens outside this frequency range. This aspect is also highlighted by the experimental transfer function, which is shown in Figure 4.25, together with the *1/f* fitting function of an ideal first-order temporal integrator. The plot unveils that the TTWWG transfer function closely follows the ideal behavior over a large portion of the spectral bandwidth. Nonetheless, we can observe an inversion of the trend for frequencies below 1 THz. Taking into account that we kept the same focusing geometry at the detection stage, the higher peak frequency exhibited by the ultra-broadband THz spectrum results in a smaller focal spot size of the THz beam at the TTWWG input, if compared to the case where we employed the $LiNbO_3$ crystal as THz source. Moreover, the THz beam generated by a plasma filament exhibits a donut-shaped transverse profile in the far field. This profile, differently from that of a Gaussian beam, assumes a cross-like shaped profile when focused [227]. Because of these effects, the overlap between the THz beam and the TTWWG input may become quite poor for the employed THz pulse, penalizing the high-frequency components, which rather radiate outside the waveguide. This effect explains the frequency loss observed in the higher part of the coupled THz spectrum, i.e. for frequencies above 8 THz. The inconsistency observed at very low frequencies, i.e. below 1 THz, may be ascribed to the detrimental effect of the aforementioned THz focused spot on the in-coupling coefficient. It is worth mentioning that the time-domain integration capability of such an ultra-broadband THz signal could be potentially improved by reducing the output wire interspacing, $2g_{out}$, as well as by adjusting that at the TTWWG input, $2g_{in}$.

CONCLUSIONS

In this dissertation, we have discussed the main results, both numerical and experimental, related to the implementation of waveguide-embedded signal-processing functionalities at THz frequencies. In particular, we demonstrated the possibility to exploit the SPR phenomenon for the realization of band-rejection filters. Moreover, to the best of our knowledge, we theoretically investigated and demonstrated, for the first time, a device that is able to perform the first-order temporal integration of both broad- and ultra-broadband THz pulses, with a good approximation. To this end, we exploited the field enhancement experienced by a THz field confined in a sub-wavelength air gap between the wires of a TTWWG.

In Chapter 1, we have introduced the reader to the THz domain, which has basically been unexplored until some decades ago. Boosted by the advances reached in the laser technology, several research groups have been attracted by the potential applications of THz radiation, especially in the communications field. Indeed, the past years have seen an ever-increasing demand for more secure communication links and for higher data-transfer rates.

In Chapter 2, we have introduced the signal-processing technology, and the importance of its development for building a fast and secure communication network. We have then provided an overview on the state-of-the-art of the waveguides operating at THz frequencies. In particular, we have explained how the dielectric-based waveguides are not suitable for the realization of broadband signal-processing operations at THz frequencies, because of the high dispersion intrinsic to dielectrics in this spectral region. As such, metal waveguides are the suitable choice for the targeted goal. For the realization of the reported signal-processing components, we have employed a two-wire waveguide structure, because of its advantages with respect to other metal-based waveguides, such as the negligible group velocity dispersion and the two-dimensional confinement of the THz field. So far, we have observed a lack of signal-processing components in the THz domain, because of the broadband nature of the THz pulses. This circumstance makes the algorithms and principles employed in other regimes, such as the optical one, quite unsuitable for the achievement of components featuring broad operational bandwidths.

In Chapter 3, we have presented our approach for the implementation of band-rejection filters at THz frequencies, based on the SPR. This phenomenon is triggered, in the THz domain, via the perforation of metal surfaces, which ultimately lowers the effective plasma frequency of metals from hundreds of THz to frequencies in the range between 0.1 and 2 THz. We have first discussed the results obtained from the numerical investigation of the designed structure, which is obtained by etching the copper wire surface with a micro-machining tool. In particular, we have demonstrated that, by properly choosing the geometrical parameters of the fabricated trenches, it is possible to induce a single resonance across the whole THz spectrum. Based on the findings from the performed numerical investigation, we fabricated two different samples with different geometrical parameters, confirming the correctness of the obtained results. In particular, we have demonstrated a narrowband frequency filter at around 0.65 THz. Moreover, we have demonstrated that, as the grating period becomes comparable with the central wavelength of the input THz pulse, the structure behaves like a Bragg Grating, with its frequency position being inversely proportional to the chosen grating period. This structure results in a weak perturbation of the THz field propagation constant in the designed structure, so that more than 100 trenches have to be fabricated on the copper wire surface. Therefore, we have designed another sample, with two different periods. The results obtained from its experimental investigation unveiled the presence of a Bragg resonance at around 0.5 THz, while all the frequency components above 0.9 THz were strongly attenuated, resulting in a low-pass filtering action.

In Chapter 4, we have shown that the confinement of a THz beam in a TTWWG exhibiting a sub-wavelength wire interspacing results in a strong enhancement of the field, which shows a frequency dependence trend resembling very closely that of a first-order temporal integrator. Throughout the Chapter, we have thoroughly explained the issues experienced during the design phase of the component, and some solutions adopted for addressing them. For example, a sub-wavelength wire interspacing at the waveguide input would result in a very low coupling efficiency of the THz beam. To solve this issue, we revised the waveguide design, employing a tapered configuration, where the wire interspacing gradually decreases from the waveguide input to its output. Moreover, we have numerically investigated the performance of the device, from which we found out that, for a fixed wire interspacing value, a THz pulse exhibiting a broader spectral bandwidth results in a deviation from the behavior of a temporal integrator. This circumstance has to be ascribed to the fact that the wire interspacing has to be much smaller than the shortest wavelength in the THz pulse spectral content. To confirm these findings, we characterized the designed structure with a broad- and ultra-broadband source. For the former case, we employed a $LiNbO_3$ crystal, while for the latter we used a two-color plasma source. While the TTWWG exhibits a behavior very close to that of an ideal integrator in the case of THz pulses generated with the $LiNbO_3$ crystal, this is not the case for an ultra-broadband source. Indeed, in this case the integration capability of the TTWWG is worse, because of detrimental effects that can be ascribed to a poor overlap between the spot of the focused THz beam and the waveguide entrance, penalizing the high-frequency components, which radiate outside the waveguide instead. This issue could be potentially solved by further reducing the size of the output wire interspacing, as well as by adjusting the TTWWG input aperture.

In conclusion, we envisage that the reported waveguide-embedded signal-processing functionalities will positively influence the development of novel communication networks based on THz pulses. Generally speaking, it is expected that THz radiation will play a major role in the new communication systems, such as sixth-generation (6G) wireless systems, which will allow for the handling of massive volumes of data, as well as very high data transfer rates. As far as the devices reported and discussed in this dissertation, the waveguide-embedded THz Bragg Grating would show a large potential for sensing applications. Moreover, such a device could pave the way to the design and realization of more complex signal-processing components in the THz domain. For instance, this structure could be employed for the implementation of a phase-shifted Bragg Grating. Such a device, in a similar way to its counterpart at telecom wavelengths, could be realized via the insertion of a defect in the periodicity of the Bragg Grating, e.g. an increase in the distance between the two trenches. In particular, such a defect would have to be placed in strategic points along the grating structure, i.e. the center of the grating itself. On the other hand, as far as the first-order temporal integrator is concerned, it is known to be a key building block for the construction of a wide range of complex analog systems for both signal-processing and computing. For instance, it could be employed for the real-time computation of differential equations. A more relevant example concerns the implementation of emphasis/de-emphasis communication protocols. In this case, the THz pulses would be sent through a pre-conditioning stage (emphasis) before being delivered in free-space, and detected in a THz receiver, where the time integration (de-emphasis) could be used to restore the original signal information. By adopting this strategy, the higher frequencies would be firstly enhanced, so to counteract the atmospheric absorption loss, and then attenuated, so to equalize the signal to its original shape. This could result in an increase in the propagation distances of long-haul communication links using THz radiation, which would represent a crucial advancement in the future communication systems.

CONCLUSIONS

Dans ce travail de thèse, nous avons discuté les principaux résultats liés à la mise en œuvre des fonctionnalités de traitement de signaux intégrés dans des guides d'ondes aux fréquences THz. En particulier, nous avons démontré la possibilité d'exploiter le phénomène SPR pour la réalisation de filtres à réjection de bande. En outre, à notre connaissance, nous avons étudié et démontré, pour la première fois, un dispositif capable d'effectuer l'intégration temporelle du premier ordre d'impulsions THz à large bande et à ultra large bande, avec une bonne approximation. À cette fin, nous avons exploité l'amélioration du champ ressentie par un champ THz confiné dans un entrefer de sous-longueur d'onde entre les fils d'un TTWWG.

Dans le chapitre 1, nous avons présenté au lecteur le domaine THz, qui était essentiellement inexploré jusqu'à il y a quelques décennies. Encouragés par les progrès réalisés dans la technologie laser, plusieurs groupes de recherche ont été attirés par les applications potentielles du rayonnement THz, en particulier dans le domaine des communications. En effet, ces dernières années ont vu une demande toujours croissante de liaisons de communication plus sûres et de taux de transfert de données plus élevés.

Dans le chapitre 2, nous avons présenté la technologie de traitement du signal et l'importance de son développement pour la construction des réseaux de communication rapides et sécurisés. Nous avons ensuite donné un aperçu de l'état de l'art des guides d'onde dans le domaine THz. En particulier, nous avons expliqué comment les guides d'ondes à base de matériaux diélectriques ne sont pas adaptés à la réalisation d'opérations de traitement de signaux à large bande, en raison de la forte dispersion intrinsèque des diélectriques dans cette région spectrale. En tant que tels, les guide d'ondes métalliques sont le choix approprié pour l'objectif visé. Pour la réalisation des composants de traitement des signaux, nous avons utilisé une structure de guide d'ondes à deux fils, en raison de ses avantages par rapport à d'autres guides d'ondes à base de métal, tels que la dispersion de vitesse de groupe négligeable et le confinement bidimensionnel du champ THz. Jusqu'à présent, nous avons observé un manque de composants de traitement du signal dans le domaine THz, en raison de la nature à large bande des impulsions THz. Cette circonstance rend les algorithmes et les principes utilisés dans d'autres régimes, comme le régime optique, tout à fait inadéquats à la réalisation de composants à large bande opérationnelle.

Au chapitre 3, nous avons discuté notre approche pour la mise en œuvre de filtres à réjection de bande aux fréquences THz, sur la base du SPR. Ce phénomène est déclenché, dans le domaine THz, par la perforation des surfaces métalliques, qui finit par abaisser la fréquence effective du plasma des métaux de centaines de THz à des fréquences comprises entre 0,1 et 2 THz. Nous avons d'abord discuté des résultats obtenus par l'étude numérique de la structure conçue, qui est obtenue par la gravure de la surface du fil de cuivre avec un outil de micro-usinage. En particulier, nous avons démontré qu'en choisissant correctement les paramètres géométriques des tranchées fabriquées, il est possible d'induire une seule résonance sur tout le spectre. Sur la base des résultats des études numériques réalisées, nous avons fabriqué deux échantillons différents avec des paramètres géométriques différents, confirmant ainsi l'exactitude des résultats obtenus. En particulier, nous avons démontré un filtre de fréquence à bande étroite à environ 0,65 THz. De plus, lorsque la période du réseau devient comparable à la longueur d'onde centrale de l'impulsion THz à l'entrée, la structure se comporte comme un réseau de Bragg, sa position en fréquence étant inversement proportionnelle à la période du réseau choisie. Cette structure entraîne une faible perturbation de la constante de propagation du champ THz dans la structure conçue, de sorte que plus de 100 tranchées doivent être fabriquées sur la surface du fil de cuivre. C'est pourquoi nous avons conçu un autre échantillon, avec deux périodes différentes. Les résultats obtenus lors de son étude expérimentale ont révélé la présence d'une résonance de Bragg à environ 0,5 THz, alors que toutes les composantes de fréquence supérieures à 0,9 THz étaient fortement atténuées, ce qui a entraîné un filtrage passe-bas.

Au chapitre 4, nous avons montré que le confinement d'un faisceau THz dans un TTWWG présentant un espacement des fils inférieur à la longueur d'onde entraîne une forte amélioration du champ, qui présente une tendance de dépendance en fréquence très proche de celle d'un intégrateur temporel du premier ordre. Tout au long du chapitre, nous avons expliqué en détail les problèmes rencontrés lors de la phase de conception du composant et certaines solutions adoptées pour y remédier. Par exemple, un espacement des fils de sous-longueur d'onde à l'entrée du guide d'ondes entraînerait une très faible efficacité de couplage du faisceau THz. Pour résoudre ce problème, nous avons révisé la conception du guide d'onde, en utilisant une configuration conique, où l'espacement des fils diminue progressivement de l'entrée du guide d'onde à sa sortie. De plus, nous avons étudié numériquement la performance du dispositif, ce qui nous a permis de découvrir que, pour une valeur fixe d'espacement des fils, une impulsion THz présentant une largeur de bande spectrale plus large entraîne une déviation du comportement d'un intégrateur temporel. Cette circonstance doit être attribuée au fait que l'espacement entre les fils doit être beaucoup plus petit que la longueur d'onde la plus courte dans le contenu spectral de l'impulsion THz. Pour confirmer ces résultats, nous avons caractérisé la structure conçue avec une source à large et ultra large bande. Pour le premier cas, nous avons utilisé un cristal de $LiNbO_3$, tandis que pour le second, nous avons utilisé une source de plasma bicolore. Alors que le TTWWG présente un comportement très proche de celui d'un intégrateur idéal dans le cas d'impulsion THz générées avec le cristal $LiNbO_3$, ce n'est pas le cas pour une source à ultra-large bande. En effet, dans ce cas, la capacité d'intégration du TTWWG est pire, en raison des effets néfastes qui peuvent être attribués à un mauvais chevauchement entre le point du faisceau THz focalisé et l'entrée du guide d'ondes, pénalisant les composantes à haute fréquence, qui rayonnent plutôt à l'extérieur du guide d'ondes. Ce problème pourrait être résolu en réduisant davantage la taille de l'espacement des fils de sortie, ainsi qu'en ajustant l'ouverture d'entrée du TTWWG.

En conclusion, nous pensons que les fonctionnalités de traitement des signaux intégrées aux guides d'ondes qui ont été signalés influenceront positivement le développement de nouveaux réseaux de communication basés sur les impulsions THz. D'une manière générale, on s'attend à ce que le rayonnement THz joue un rôle majeur dans les nouveaux systèmes de communication, tels que les systèmes sans fil de sixième génération (6G), qui permettront de traiter des volumes massifs de données, ainsi que des taux de transfert de données très élevés. Plus spécifiquement, la mise en œuvre du réseau de Bragg pourrait ouvrir la voie à la réalisation de composants de traitement du signal plus complexes. Par exemple, outre le potentiel évident pour les applications de détection, la structure réalisée pourrait être utilisée pour la mise en œuvre d'un réseau de Bragg déphasé. De manière similaire à son homologue dans les longueurs d’onde des télécommunications, un tel composant pourrait être réalisé en insérant un défaut dans la structure périodique, tel qu’une augmentation de la distance entre deux tranchées. En ce qui concerne l’intégrateur temporel du premier ordre, on sait qu’il est un élément clé pour la construction d’une large gamme de systèmes analogiques complexes, tant pour le traitement des signaux que pour le calcul. Par exemple, il pourrait être utilisé pour le calcul en temps réel d’équations différentielles. Un exemple plus pertinent concerne la mise en œuvre de protocoles de communication d’accentuation/désaccentuation. Dans ce cas, les impulsions THz seraient envoyées à travers un étage de pré-conditionnement (accentuation) avant d’être délivrées en espace libre, et détectées dans un récepteur THz, où l’intégration temporelle (désaccentuation) pourrait être utilisée pour restaurer les informations du signal original. En adoptant cette stratégie, les hautes fréquences seraient d’abord augmentées, afin de contrer la perte par absorption atmosphérique, puis atténuées, afin d’égaliser le signal à sa forme originale. Il pourrait en résulter une augmentation des distances de propagation des liaisons de communication à longue distance utilisant le rayonnement THz, ce qui représenterait un progrès crucial pour les futurs systèmes de communication.

CONCLUSIONI

In questo lavoro di tesi, abbiamo discusso i risultati principali, sia numerici che sperimentali, legati all'implementazione di dispositivi integrati in guida per l'elaborazione di segnali nel campo THz. In particolare, abbiamo dimostrato la possibilità di sfruttare il fenomeno della risonanza plasmonica di superficie per l'implementazione di filtri elimina-banda. Inoltre, al meglio della nostra conoscenza, abbiamo investigato e dimostrato, per la prima volta, un dispositivo in grado di calcolare l'integrale di primo ordine di impulsi THz a banda larga ed ultra-larga. A tal fine, abbiamo sfruttato l'arricchimento del campo THz quando è confinato nello spazio (avente dimensioni molto inferiori alla lunghezza d'onda) tra i due fili di una TTWWG.

Nel primo capitolo, abbiamo introdotto il lettore al campo THz, il quale è rimasto essenzialmente inesplorato fino a qualche decennio fa. Stimolati dai progressi ottenuti nella tecnologia laser, diversi gruppi di ricerca si sono interessati a questa radiazione, per via delle sue applicazioni potenziali, soprattutto nel campo delle comuicazioni. Infatti, in questi ultimi anni è stata registrata una domanda sempre crescente per collegamenti di comunicazione più sicuri e per velocità di trasferimento dati più elevate.

Nel secondo capitolo, abbiamo introdotto la tecnologia di elaborazione dei segnali, e l'importanza del suo sviluppo per la progettazione di reti di comunicazione veloci e sicure. Abbiamo quindi fornito una panoramica sullo stato dell'arte delle guide d'onda nel campo THz. In particolare, abbiamo spiegato come le guide basate su materiali dielettrici non sono adatte per la realizzazione di operazioni di elaborazione di segnali a larga banda, a causa della loro innata elevata dispersione. Di conseguenza, le guide metalliche sono una scelta opportuna per l'obiettivo prefissato. Per la realizzazione dei componenti riportati in questo lavoro di tesi, abbiamo impiegato una struttura bifilare, a causa dei suoi vantaggi rispetto ad altre guide metalliche, come per esempio la dispersione della velocità di gruppo trascurabile e il confinamento bidimensionale del campo THz. Finora, abbiamo potuto osservare una mancaza di tali componenti nel campo THz, per via della natura a larga banda degli impulsi THz. Tale circostanza rende gli algoritmi ed i principi usati in altri regimi, come ad esempio quello ottico, poco adeguati per la realizzazione di componenti che abbiano larghe bande operative.

Nel terzo capitolo, abbiamo presentato il nostro approccio per l'implementazione di filtri elimina-banda, basati sulla risonanza plasmonica di superficie. Questo fenomeno viene innescato, nel campo THz, attraverso la perforazione di superfici metalliche. In questo modo, è possibile diminuire la frequenza di plasma efficace dei metalli, da alcune centinaia di THz ad un intervallo compreso tra 0.1 e 2 THz. Abbiamo dapprima discusso i risultati ottenuti dallo studio numerico di tale struttura, la quale è ottenuta dall'incisione della superficie del filo con uno strumento di *micro-machining*. In particolare, abbiamo dimostrato che, scegliendo in maniera appropriata i parametri geometrici degli scavi fabbricati, è possibile indurre una singola risonanza a cavallo dell'intera risposta spettrale. Dai risultati ottenuti da questi studi teorici, abbiamo fabbricato due campioni differenti, aventi parametri geometrici diversi, confermando la correttezza dei risultati teorici. In particolare, abbiamo dimostrato un filtro in frequenza a banda stretta attorno a 0.65 THz. Inoltre, abbiamo provato che, quando il periodo del reticolo diventa paragonabile alla lunghezza d'onda centrale dell'impulso THz al suo ingresso, la struttura si comporta in maniera simile ad un reticolo di Bragg, dove la posizione in frequenza della risonanza è inversamente proporzionale al periodo del reticolo. Una tale struttura comporta una debole perturbazione della costante di propagazione del campo THz. Di conseguenza, è necessario realizzare più di 100 scavi sulla superficie del filo di rame. Pertanto, abbiamo fabbricato un altro campione, con due diverse periodicità. Dai risultati ottenuti dalla caratterizzazione sperimentale, abbiamo potuto notare la presenza di una risonanza a circa 0.5 THz, mentre tutte le componenti in frequenza al di sopra di 0.9 THz sono state fortemente attenuate.

Nel quarto capitolo, abbiamo mostrato che il confinamento di un fascio THz in una TTWWG con un interspazio tra i fili molto più piccolo della lunghezza d'onda (*sub-wavelength*) produce un forte arricchimento del campo THz. Il comportamento in frequenza di questa struttura è molto simile a quello di un integratore temporale del primo ordine. In tutto il capitolo, abbiamo spiegato, in maniera esaustiva, le problematiche riscontrate durante la fase di progettazione del componente, ed alcune soluzioni adottate per superare tali ostacoli. Ad esempio, un valore molto piccolo dell'interspazio tra i fili all'ingresso della guida comporterebbe una efficienza di accoppiamento del campo molto bassa. Al fine di risolvere tale problematica, abbiamo modificato la struttura della guida, impiegando una configurazione a tromba, dove l'interspazio tra i fili decresce gradualmente dall'ingresso della guida verso la sua uscita. Inoltre, abbiamo investigato la prestazione del dispositivo, trovando che, per un valore fisso dell'interspazio tra i fili, un impulso THz con un contenuto spettrale più ampio comporta una deviazione dal comportamento ideale di un integratore. Ciò può essere attribuito al fatto che l'interspazio tra i fili deve assumere valori molto più piccoli rispetto alla minima lunghezza d'onda nel contenuto spettrale dell'impulso THz. A tale scopo, abbiamo caratterizzato la guida d'onda con una sorgente a larga banda ed una a banda ultra-larga. Nel primo caso, abbiamo utilizzato un cristallo di niobato di litio ($LiNbO_3$), mentre nel secondo casso abbiamo utilizzato una sorgente a plasma bicolore. Mentre la guida mostra un comportamento molto vicino a quello di un integratore ideale nel primo caso, ciò non è vero nel secondo. Infatti, nel caso di una sorgente a banda ultra-larga, la prestazione dell'integratore peggiora, a causa di effetti deleteri che possono essere attribuiti alla scarsa sovrapposizione tra la forma del fascio THz focalizzato e l'ingresso della guida. Ciò comporta una penalizzazione delle componenti ad alta frequenza, che irradiano al di fuori della guida. Tale problematica potrebbe essere potenzialmente risolta riducendo ulteriormente il valore dell'interspazio tra i fili all'uscita della guida, oltre che modificando l'apertura della guida al suo ingresso.

In conclusione, prevediamo che le funzionalità riportate in questo lavoro di tesi influenzeranno positivamente lo sviluppo di nuove reti di comunicazione basate sulla radiazione THz. In generale, ci si aspetta che la radiazione THz avrà un ruolo principale nello sviluppo di nuovi sistemi di comunicazione, come ad esempio quelli di sesta generazione (6G). Tali sistemi permetteranno la gestione di volumi enormi di dati e velocità di trasferimento molto elevate. Più in dettaglio, la realizzazione del reticolo di Bragg potrebbe spianare la strada verso la realizzazione di componenti più complessi. Ad esempio, oltre l'ovvio potenziale per applicazioni di *sensing*, la struttura potrebbe essere impiegata per la realizzazione di un reticolo di Bragg sfasato. In maniera molto simile alla sua controparte ottica, alle lunghezze d'onda telecom, un tale componente potrebbe essere realizzato alterando la periodicità della struttura, ad esempio aumentando la distanza tra due scavi. Per quanto riguarda l'integratore del primo ordine, è noto che sia un elemento chiave per la realizzazione di un’ampia gamma di sistemi analogici omplessi per l’elaborazione di segnali. Ad esempio, potrebbe essere impiegato per la risoluzione in tempo reale di equazioni differenziali. Un esempio più rilevante riguarda la realizzazione di protocolli di comunicazioni enfasi/deenfasi. In questo caso, l’impulso THz sarebbe trasmesso attraverso uno stadio di pre-condizionamento (enfasi) prima di essere inviato al ricevitore THz, dove l’integrazione temporale (deenfasi) potrebbe essere usata per ripristinare l’informazione originale del segnale. Adottando una tale strategia, le frequenze più elevate verrebbero dapprima arricchite, così da controbilanciare le perdite dovute all’assorbimento atmosferico, e quindi attenuate, così da ripristinare il segnale alla sua forma originale. Ciò potrebbe comportare un aumento nelle distanze di propagazione nei sistemi di comunicazione basati sulla radiazione THz, rappresentando dunque un progresso notevole per i futuri sistemi di comunicazione.

APPENDIX A

TWO-WIRE WAVEGUIDE

A.1. TERAHERTZ FIELD CONFINEMENT IN THE TWO-WIRE WAVEGUIDE

As briefly mentioned in Chapter 2, the two-wire waveguide shows many advantages with respect to other metal- and dielectric-based waveguides, designed and demonstrated so far in the THz range. One of the main advantages of such an architecture is the fact that it supports a TEM wave as its fundamental mode (lowest TM mode, TM_0), with the latter exhibiting a linear polarization. This circumstance makes the coupling of a THz beam emitted by a commonly-employed source, such as a PCA, quite efficient. This is true as long as the wire interspacing is comparable in value with the central wavelength of the coupled THz pulse, and its waist size. On the one hand, if the wire interspacing is larger than the THz central wavelength, e.g. three to four times larger, then the typical TEM fundamental mode of the TWWG no longer exists between the two wires. Rather, there are individual Sommerfeld modes, similar to the fundamental mode of a SWWG, around each wire, resulting in a negligible coupling coefficient of the incoming THz beam [116], because of the polarization mismatch between the incoming THz field and the waveguide fundamental mode. Additionally, if the wire interspacing is much smaller than the THz beam waist, the coupling efficiency of the free-space THz beam is strongly reduced, as also discussed in Section 4.3.1 and shown in Figure 4.5 for the case of a waist radius of $w_{THz} = 600$ μm. In order to validate this assert, we performed modal simulations with the aim of retrieving the distribution of the THz field in the investigated

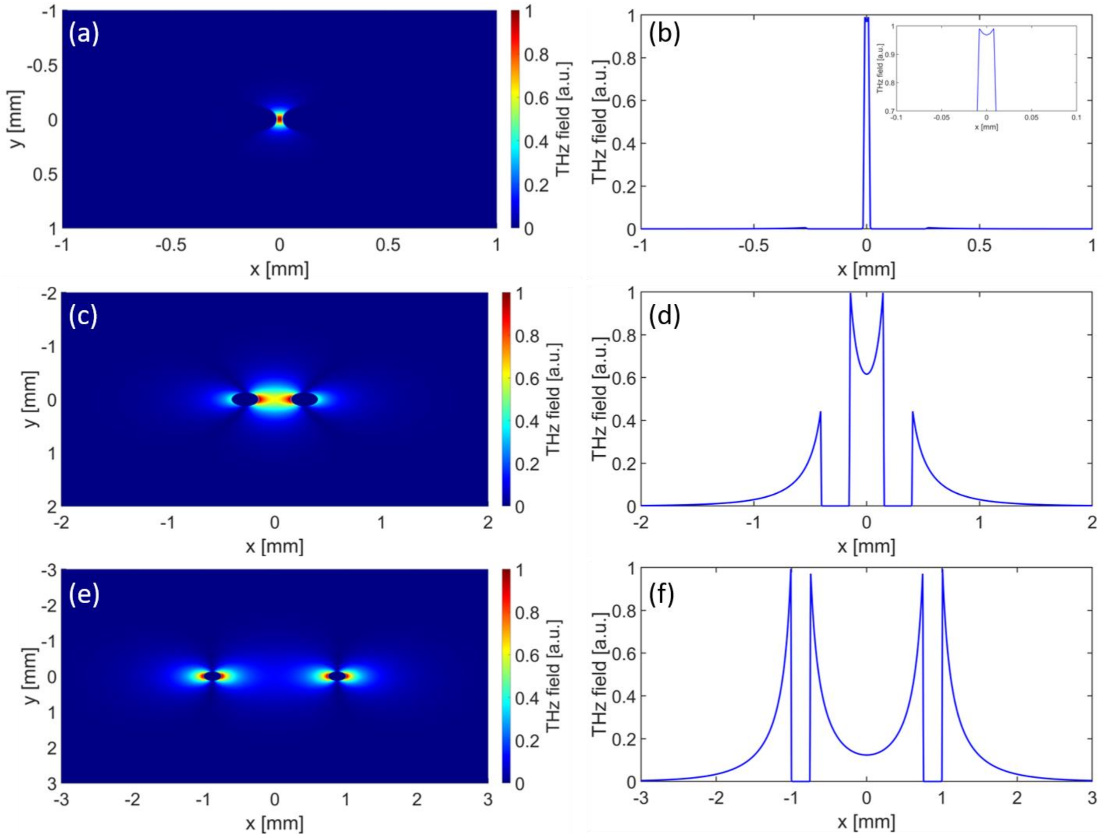

Figure A.1. THz electric field distribution of the fundamental TEM mode (a, c, e) and its transverse profile calculated on the line hosting the wire centers (b, d, f) for TWWGs featuring a wire interspacing of (a-b) $2g$ = 24 μm, (c-d) $2g$ = 300 μm, and (e-f) $2g$ = 1500 μm. The inset in (b) shows a zoom of the electric field profile in the sub-wavelength wire interspacing, for a better visualization.

waveguide. In particular, we investigated the effect of the wire interspacing on the field distribution. For this task, we set a test frequency of f_c = 1 THz and a wire radius of R = 127 μm, while we investigated three different values of the wire interspacing, i.e. $2g$ = 24 μm, $2g$ = 300 μm and $2g$ = 1500 μm. The simulations were performed by means of an eigenmode solver. It is worth highlighting that, for the goal of this and the following theoretical investigations, we considered copper as the metal material for the wires. In particular, we inserted the complex-valued permittivity for the metal, i.e. $\varepsilon_{copper} = -1.7 * 10^5 + \frac{1.1*10^6}{f}$ [2], where f is the frequency expressed in THz.

The results from the study are shown in Figure A.1. In more detail, we show the THz electric field distribution and its transverse profile on the line hosting the two wire centers, i.e.

$y = 0$, for three different wire interspacing values: $2g$ = 24 μm (a-b), $2g$ = 300 μm (c-d) and $2g$ = 1500 μm (e-f). From Figure A.1(a-d) we can notice how, for wire interspacing values smaller or comparable to the THz wavelength, i.e. λ_c = 300 μm, the THz field is distributed in the air gap between the two wires. Conversely, as the wire interspacing is increased and becomes much larger than the THz central wavelength, the coupled THz field is more distributed around the copper wires, as it can be observed in Figure A.1(e-f). Moreover, the x-component of the fundamental mode exhibits two evanescent tails on the outer sides of the wires, with their amplitude increasing as a function of the wire interspacing. This aspect is highlighted in the electric field transverse profiles, shown in Figure A.1(d, f). Furthermore, the amplitude of the coupled THz field at the center of the gap between the two wires exhibits lower values as the wire interspacing increases, which is consistent with the field distribution being located in the area close to the wires as the wire interspacing is increased. Conversely, for a wire interspacing smaller than the THz central wavelength, this amplitude is larger. This aspect can be better observed in Figure A.1(b) and its inset, where we can observe that the amplitude of the THz electric field exhibits a negligible change in the air gap between the two wires. Another geometrical parameter that affects the distribution of the TWWG fundamental mode is the wire radius. To better investigate this aspect, we performed the same type of study for this geometrical parameter. For the task, we set the same test frequency, i.e. f_c = 1 THz, while the chosen wire interspacing was $2g$ = 300 μm. The results from this investigation are shown in Figure A.2. In more detail, we show the THz electric field distribution, and its transverse profile on the line hosting the wire centers, i.e. $y = 0$, for three different values of the wire radius, i.e. R = 64 μm (a-b), R = 127 μm (c-d), and R = 254 μm (e-f). We can see here a similar dynamic as in the case of the wire interspacing. In other words, the larger the wire radius, the more the TWWG fundamental mode is confined in the volume between the two wires, as we can observe from Figure A.2(b), (d), and (f). Moreover, as the wire radius is increased, we can observe the presence of the evanescent tails seen in the previous case for a large wire interspacing, with their amplitude increasing as the wire radius is decreased. These preliminary results seem to indicate that the best performance of the TWWG, in terms of field confinement, is achieved with a larger wire radius and a small wire interspacing.

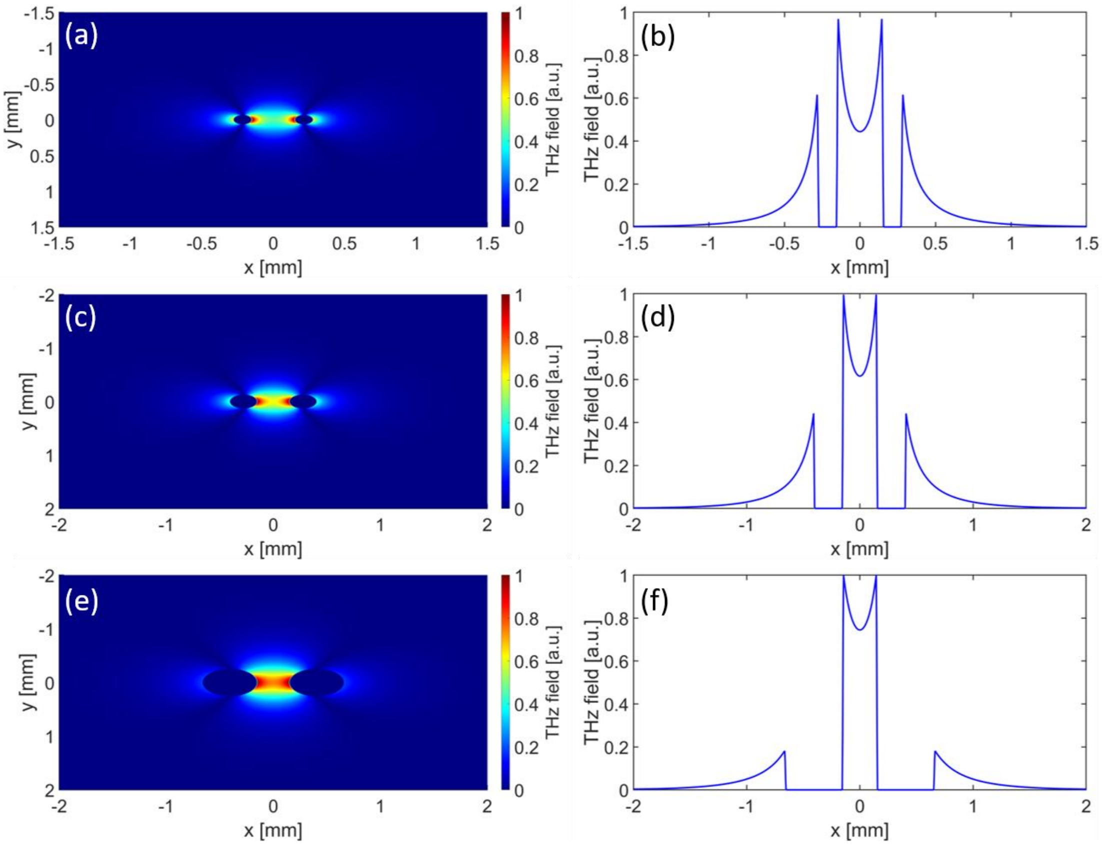

Figure A.2. THz electric field distribution of the fundamental TEM mode (a, c, e) and its transverse profile calculated on the line hosting the wire centers (b, d, f) for TWWGs featuring a wire radius of (a-b) *R* = 64 μm, (c-d) *R* = 127 μm, and (e-f) *R* = 254 μm.

A.2. TWO-WIRE WAVEGUIDE MODAL LOSSES

Another significant advantage of the TWWG is its low modal losses, due to the confinement of the coupled THz field in the air gap. Moreover, this parameter is strongly dependent on both the wire radius and interspacing. To better investigate this aspect, we performed a theoretical analysis with the aim of investigating how the TWWG geometrical parameters affect the waveguide modal losses. In particular, we performed two studies, where we varied one of the two geometrical parameters, i.e. wire interspacing and radius, while keeping the other one fixed. In the first numerical investigation, we analyzed the effect of the wire interspacing, by evaluating the modal losses at a fixed value of the wire radius of *R* = 127 μm. Moreover, this parameter was investigated in the frequency range from 0.1 to 4 THz, while we took into account three different interspacing values, i.e. $2g$ = 24 µm, $2g$ = 300 µm and $2g$ = 1500 µm. The modal losses were evaluated as follows. Firstly, from the modal analysis, we retrieved the effective refractive index of the waveguide at the given frequency f_c, $n_{eff} = n_r + jn_i$, with n_r and n_i being its real and imaginary parts, respectively. Subsequently, the modal losses were calculated from the following relationship:

$$\alpha\left[\frac{dB}{m}\right] = \frac{4\pi f_c}{c} n_i \tag{A.1}$$

The results are shown in Figure A.3(a), where the light blue, yellow, and dark red curves show the trends for the 24, 300, and 1500 µm wire interspacing, respectively. From the plot in Figure A.3(a) we can notice how the values of the modal losses for the TWWG are quite low, i.e. < 0.1 dB/cm, for all the investigated wire interspacing and frequency values. Additionally, the modal losses increase as a function of the frequency. This increase might be ascribed to the change in the distribution of the THz field within the TWWG, which would mostly be located on the outer side of the TWWG than between the two wires. Another aspect that can be observed from the plot in Figure A.3(a) is that, for a fixed frequency value, the modal losses significantly decrease as the wire interspacing increases. This is caused by the larger distribution of the THz field as the wire interspacing exhibits large values. Moving the wires farther apart, i.e. to values much larger than the THz wavelength, results in the THz electric field surrounding the metal wires, which ultimately results in lower losses, even though this comes at the expenses of the waveguide supporting higher-order modes, as well as the aforementioned polarization mismatch between the single wire fundamental mode, i.e. radially-polarized and that of a THz beam emitted by a THz source, i.e. linearly-polarized.

In the second theoretical investigation, we analyzed the effect of the wire radius on the modal losses, following the same procedure reported in the previous notes. In this case, we kept the wire interspacing fixed at $2g$ = 300 µm, while the frequency was varied in a range from 0.1 to 4 THz, similarly to the previous case. We carried out the simulation for three different radii values, i.e. R = 64 µm, R = 127 µm, and R = 254 µm. The results from this investigation are shown in Figure A.3(b), where the light blue, yellow, and dark red curves show the trends for

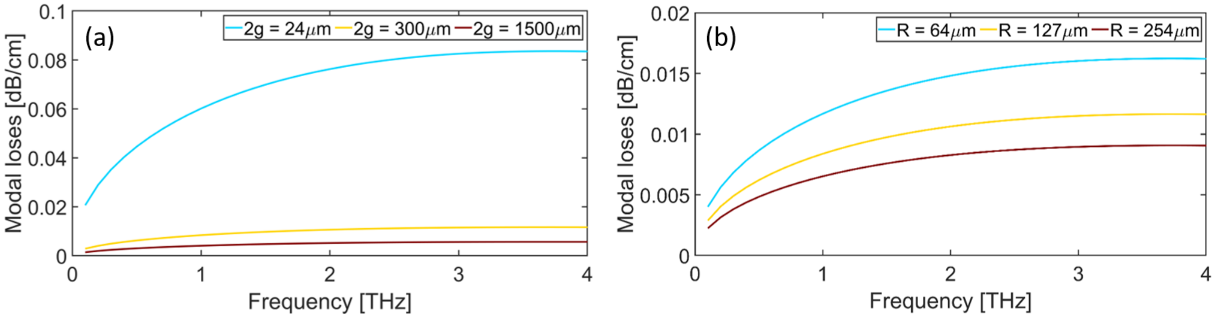

Figure A.3. Modal losses of the TWWG fundamental mode, evaluated as indicated in Eq. (A.1), as a function of the THz frequency for three different values of the wire interspacing (a) and radius (b). In (a), the wire interspacing values are *2g* = 24 µm (light blue line), *2g* = 300 µm (yellow line), and *2g* = 1500 µm (dark red line), while the wire radius is *R* = 127 µm. In (b), the wire radius values are *R* = 64 µm (light blue line), *R* = 127 µm (yellow line), and *R* = 254 µm (dark red line), with the wire interspacing being fixed at *2g* = 300 µm.

the 64, 127, and 254 µm radii values, respectively. From the plots in Figure A.3(b) we can immediately observe that, for a fixed frequency value, the modal losses strongly increase as the wire radius is increased. The reason behind this dynamic is actually very similar to that seen for the wire interspacing values. As a matter of fact, as the wire radius increases, the THz field is distributed over a longer area. Moreover, as we can see from the plots in Figure A.2, as the wire radius is increased, the evanescent tails outside the TWWG strongly decrease in amplitude, thus leading to smaller losses during the propagation.

APPENDIX B

B.1. LIST OF ARTICLES PUBLISHED IN SCIENTIFIC JOURNALS

1. **G. Balistreri**, A. Tomasino, J. Dong, A. Yurtsever, S. Stivala, J. Azaña, and R. Morandotti, "*Time-Domain Integration of broadband terahertz pulses in tapered two-wire waveguides*", manuscript in preparation.
2. J. Dong, A. Tomasino, **G. Balistreri**, P. You, A. Vorobiov, A. Yurtsever, S. Stivala, M. A. Vincenti, C. De Angelis, D. Kip, J. Azaña, and R. Morandotti, "*Terahertz Polarization-division Multiplexing and Signal-Processing Devices Based on Four-wire Waveguides*", manuscript in preparation.

B.2. LIST OF CONFERENCE PROCEEDINGS

1. **G. Balistreri**, A. Tomasino, S. Stivala, P. Livreri, A. C. Cino, and A. Busacca, "*Terahertz Time-Domain Spectroscopy Based on Photoconductive Antennas*", 48th National Meeting of the Italian Electronics Group (GE), 22-24 June 2016, Brescia, Italy, (poster).
2. **G. Balistreri**, A. Tomasino, S. Stivala, P. Livreri, A. C. Cino, and A. Busacca, "*Terahertz Time-Domain Spectroscopy Based on Photoconductive Antennas*", 18th National Meeting of the Photonic Technologies (FOTONICA 2016), 6-8 June 2016, Rome, Italy, (poster).
3. **G. Balistreri**, A. Tomasino, S. Stivala, P. Livreri, A. C. Cino, and A. Busacca, "*Dependence of Terahertz Emission and Detection in Photoconductive Antennas on Laser Parameters*", Photonics North 2017, 6-8 June 2017, Ottawa, Canada, (poster).

4. **G. Balistreri**, A. Tomasino, V. Aglieri, R. Piccoli, C. Foucher, A. Markov, S. Stivala, A. Busacca, F. De Angelis, R. Carzino, A. Toma, L. Razzari, J. Azaña, and R. Morandotti, "*Design and Fabrication of Terahertz Bragg Gratings on a Two-Wire Waveguide*", Photonics North 2018, 5-7 June 2018, Montreal, Canada, (oral).
5. **G. Balistreri**, A. Tomasino, J. Dong, R. Piccoli, S. Stivala, A. Yurtsever, L. Razzari, J. Azaña, and R. Morandotti, "*Design and Fabrication of Terahertz Metallic Gratings on a Two-Wire Waveguide*", Photonics North 2019, 21-23 May 2019, Quebec City, Canada, (oral).

REFERENCES

1. X.-C. Zhang and J. Xu, *Introduction to THz Wave Photonics* (Springer US, 2010).
2. Y.-S. Lee, *Principles of Terahertz Science and Technology* (Springer, 2009).
3. A. Y. Pawar, D. D. Sonawane, K. B. Erande, and D. V. Derle, "Terahertz technology and its applications," Drug Invent. Today **5**(2), 157–163 (2013).
4. P. H. Siegel, *Terahertz Technology* (2002), **50**(3).
5. X. Lu and X.-C. Zhang, "Investigation of ultra-broadband terahertz time-domain spectroscopy with terahertz wave gas photonics," Front. Optoelectron. **7**(2), 121–155 (2014).
6. F. Zernike and P. R. Berman, "Generation of Far Infrared as a Difference Frequency," Phys. Rev. Lett. **16**(3), 117–117 (1966).
7. C. H. Lee, "Picosecond optoelectronic switching in GaAs," Appl. Phys. Lett. **30**(2), 84–86 (1977).
8. Chi Lee and V. Mathur, "Picosecond photoconductivity and its applications," IEEE J. Quantum Electron. **17**(10), 2098–2112 (1981).
9. G. Mourou, C. V. Stancampiano, A. Antonetti, and A. Orszag, "Picosecond microwave pulses generated with a subpicosecond laser-driven semiconductor switch," Appl. Phys. Lett. **39**(4), 295–296 (1981).
10. J. Valdmanis, G. Mourou, and C. Gabel, "Subpicosecond electrical sampling," IEEE J. Quantum Electron. **19**(4), 664–667 (1983).
11. J.-C. Diels and W. Rudolph, *Ultrashort Laser Pulse Phenomena : Fundamentals, Techniques, and Applications on a Femtosecond Time Scale* (Elsevier/Academic Press, 2006).
12. K. Sakai, *Terahertz Optoelectronics* (Springer, 2011).
13. C. Rullière, *Femtosecond Laser Pulses : Principles and Experiments* (Springer, 2005).
14. M. Tonouchi, "Cutting-edge terahertz technology," Nat. Photonics **1**(2), 97–105 (2007).
15. C. Zandonella, "T-ray specs," Nature **424**(6950), 721–722 (2003).
16. B. Ferguson and X.-C. Zhang, "Materials for terahertz science and technology," Nat. Mater. **1**(1), 26–33 (2002).
17. D. Dragoman and M. Dragoman, "Terahertz fields and applications," Prog. Quantum Electron. **28**(1), 1–66 (2004).

18. S. Cherry, "Edholm's law of bandwidth," IEEE Spectr. **41**(7), 58–60 (2004).

19. C. A. Schmuttenmaer, "Exploring Dynamics in the Far-Infrared with Terahertz Spectroscopy," (2004).

20. J. Lloyd-Hughes and T. I. Jeon, "A review of the terahertz conductivity of bulk and nano-materials," J. Infrared, Millimeter, Terahertz Waves **33**(9), 871–925 (2012).

21. S. Sim, M. Brahlek, N. Koirala, S. Cha, S. Oh, and H. Choi, "Ultrafast terahertz dynamics of hot Dirac-electron surface scattering in the topological insulator Bi2 Se3," Phys. Rev. B - Condens. Matter Mater. Phys. **89**(16), (2014).

22. T. Yasui, T. Yasuda, K. I. Sawanaka, and T. Araki, "Terahertz paintmeter for noncontact monitoring of thickness and drying progress in paint film," Appl. Opt. **44**(32), 6849–6856 (2005).

23. C. Yu, S. Fan, Y. Sun, and E. Pickwell-Macpherson, "The potential of terahertz imaging for cancer diagnosis: A review of investigations to date.," Quant. Imaging Med. Surg. **2**(1), 33–45 (2012).

24. S. Fan, B. S. Y. Ung, E. P. J. Parrott, V. P. Wallace, and E. Pickwell-MacPherson, "*In vivo* terahertz reflection imaging of human scars during and after the healing process," J. Biophotonics **10**(9), 1143–1151 (2017).

25. J. F. Federici, B. Schulkin, F. Huang, D. Gary, R. Barat, F. Oliveira, and D. Zimdars, "THz imaging and sensing for security applications—explosives, weapons and drugs," Semicond. Sci. Technol. **20**(7), S266–S280 (2005).

26. H. Breitenborn, J. Dong, R. Piccoli, A. Bruhacs, L. V. Besteiro, A. Skripka, Z. M. Wang, A. O. Govorov, L. Razzari, F. Vetrone, R. Naccache, and R. Morandotti, "Quantifying the photothermal conversion efficiency of plasmonic nanoparticles by means of terahertz radiation," APL Photonics **4**(12), 126106 (2019).

27. R. Naccache, A. Mazhorova, M. Clerici, R. Piccoli, L. K. Khorashad, A. O. Govorov, L. Razzari, F. Vetrone, and R. Morandotti, "Terahertz Thermometry: Combining Hyperspectral Imaging and Temperature Mapping at Terahertz Frequencies," Laser Photonics Rev. **11**(5), 1600342 (2017).

28. T. Nagatsuma, G. Ducournau, and C. C. Renaud, "Advances in terahertz communications accelerated by photonics," Nat. Photonics **10**(6), 371–379 (2016).

29. H. M. Cheema, R. Mahmoudi, and A. H. M. Roermund, *60-GHz CMOS Phase-Locked Loops* (Springer Netherlands, 2010).

30. A. Nahata and T. F. Heinz, "Detection of freely propagating terahertz radiation by use of optical second-harmonic generation," Opt. Lett. **23**(1), 67 (1998).

31. Q. Wu and X. -C. Zhang, "Free-space electro-optic sampling of terahertz beams," Appl. Phys. Lett. **67**(24), 3523–3525 (1995).

32. Q. Wu and X. C. Zhang, "7 terahertz broadband GaP electro-optic sensor," Appl. Phys. Lett. **70**(14), 1784–1786 (1997).

33. A. Nahata, A. S. Weling, and T. F. Heinz, "A wideband coherent terahertz spectroscopy system using optical rectification and electro-optic sampling," Appl. Phys. Lett. **69**(16), 2321–2323 (1996).

34. P. R. Smith, D. H. Auston, and M. C. Nuss, "Subpicosecond photoconducting dipole antennas," IEEE J. Quantum Electron. **24**(2), 255–260 (1988).

35. M. Tani, S. Matsuura, K. Sakai, and S. Nakashima, "Emission characteristics of photoconductive antennas based on low-temperature-grown GaAs and semi-insulating GaAs," Appl. Opt. **36**(30), 7853 (1997).

36. Y. C. Shen, P. C. Upadhya, H. E. Beere, E. H. Linfield, A. G. Davies, I. S. Gregory, C. Baker, W. R. Tribe, and M. J. Evans, "Generation and detection of ultrabroadband terahertz radiation using photoconductive emitters and receivers," Appl. Phys. Lett. **85**(2), 164–166 (2004).

37. C.-Y. Li, D. V. Seletskiy, Z. Yang, and M. Sheik-Bahae, "Broadband field-resolved terahertz detection via laser induced air plasma with controlled optical bias," Opt. Express **23**(9), 11436 (2015).

38. J.-M. Manceau, M. Massaouti, and S. Tzortzakis, "Strong terahertz emission enhancement via femtosecond laser filament concatenation in air," Opt. Lett. **35**(14), 2424 (2010).

39. X. Lu, N. Karpowicz, and X.-C. Zhang, "Broadband terahertz detection with selected gases," J. Opt. Soc. Am. B **26**(9), A66 (2009).

40. A. Tomasino, A. Mazhorova, M. Clerici, M. Peccianti, S.-P. Ho, Y. Jestin, A. Pasquazi, A. Markov, X. Jin, R. Piccoli, S. Delprat, M. Chaker, A. Busacca, J. Ali, L. Razzari, and R. Morandotti, "Solid-state-biased coherent detection of ultra-broadband terahertz pulses," Optica **4**(11), 1358 (2017).

41. A. Tomasino, R. Piccoli, Y. Jestin, S. Delprat, M. Chaker, M. Peccianti, M. Clerici, A. Busacca, L. Razzari, and R. Morandotti, "Invited Article: Ultra-broadband terahertz coherent detection via a silicon nitride-based deep sub-wavelength metallic slit," APL Photonics **3**(11), 110805 (2018).

42. M. Shafi, A. F. Molisch, P. J. Smith, T. Haustein, P. Zhu, P. De Silva, F. Tufvesson, A. Benjebbour, and G. Wunder, "5G: A tutorial overview of standards, trials, challenges, deployment, and practice," IEEE J. Sel. Areas Commun. **35**(6), 1201–1221 (2017).

43. H. Yu, H. Lee, and H. Jeon, "What is 5G? Emerging 5G Mobile Services and Network Requirements," Sustainability **9**(10), 1848 (2017).

44. J. F. O'Hara, S. Ekin, W. Choi, and I. Song, "A Perspective on Terahertz Next-Generation Wireless Communications," Technologies **7**(2), 43 (2019).

45. D. Saeedkia, *Handbook of Terahertz Technology for Imaging, Sensing and Communications* (WP Woodhead Publishing, 2013).

46. M. Giordani, M. Polese, M. Mezzavilla, S. Rangan, and M. Zorzi, "Towards 6G Networks: Use Cases and Technologies," (2019).

47. S. Mumtaz, J. M. Jornet, J. Aulin, W. H. Gerstacker, X. Dong, and B. Ai, "Terahertz Communication for Vehicular Networks," IEEE Trans. Veh. Technol. **66**(7), 5617–5625 (2017).

48. M. Z. Chowdhury, M. Shahjalal, S. Ahmed, and Y. M. Jang, "6G Wireless Communication Systems: Applications, Requirements, Technologies, Challenges, and Research Directions," (2019).

49. D. Kedar and S. Arnon, "Urban optical wireless communication networks: the main challenges and possible solutions," IEEE Commun. Mag. **42**(5), S2–S7 (2004).

50. D. J. T. Heatley, D. R. Wisely, I. Neild, and P. Cochrane, "Optical wireless: The story so far," IEEE Commun. Mag. **36**(12), 72–82 (1998).

51. J. Federici and L. Moeller, "Review of terahertz and subterahertz wireless communications," J. Appl. Phys. **107**(11), (2010).

52. J. F. Federici, J. Ma, and L. Moeller, "Review of weather impact on outdoor terahertz wireless communication links," Nano Commun. Netw. **10**, 13–26 (2016).

53. A. J. Seeds, H. Shams, M. J. Fice, and C. C. Renaud, "TeraHertz Photonics for Wireless Communications," J. Light. Technol. **33**(3), 579–587 (2015).

54. T. Kleine-Ostmann and T. Nagatsuma, "A Review on Terahertz Communications Research," J. Infrared, Millimeter, Terahertz Waves **32**(2), 143–171 (2011).

55. H. J. Song and T. Nagatsuma, "Present and future of terahertz communications," IEEE Trans. Terahertz Sci. Technol. **1**(1), 256–263 (2011).

56. R. Piesiewicz, J. Jemai, M. Koch, and T. Kurner, "THz channel characterization for future wireless gigabit indoor communication systems," in *Proceedings of the SPIE, Volume 5727, p. 166-176 (2005).*, R. J. Hwu and K. J. Linden, eds. (2005), **5727**, p. 166.

57. A. Hirata, T. Nagatsuma, T. Kosugi, H. Takahashi, R. Yamaguchi, N. Shimizu, N. Kukutsu, K. Murata, Y. Kado, H. Ikegawa, H. Nishikawa, and T. Nakayama, "10-Gbit/s wireless communications technology using sub-terahertz waves," in M. Anwar, A. J. DeMaria, and M. S. Shur, eds. (2007), p. 67720B.

58. A. Hirata, M. Harada, and T. Nagatsuma, "120-ghz wireless link using photonic techniques for generation, modulation, and emission of millimeter-wave signals," J. Light. Technol. **21**(10), 2145–2153 (2003).

59. M. Clerici, M. Peccianti, B. E. Schmidt, L. Caspani, M. Shalaby, M. Giguère, A. Lotti, A. Couairon, F. Légaré, T. Ozaki, D. Faccio, and R. Morandotti, "Wavelength scaling of

terahertz generation by gas ionization," Phys. Rev. Lett. **110**(25), 253901 (2013).

60. K. Wang and D. M. Mittleman, "Guided Propagation of Terahertz Pulses on Metal Wires," in *Terahertz Frequency Detection and Identification of Materials and Objects* (Springer Netherlands, n.d.), pp. 55–68.

61. S. Atakaramians, S. Afshar V., T. M. Monro, and D. Abbott, "Terahertz dielectric waveguides," Adv. Opt. Photonics **5**(2), 169 (2013).

62. S. Atakaramians, "Terahertz waveguides: a study of microwires and porous fibres.," (2011).

63. Q. J. Gu, "THz interconnect: the last centimeter communication," IEEE Commun. Mag. **53**(4), 206–215 (2015).

64. J. Azaña, "Ultrafast analog all-optical signal processors based on fiber-grating devices," IEEE Photonics J. **2**(3), 359–386 (2010).

65. M. Kulishov and J. Azaña, "Long-period fiber gratings as ultrafast optical differentiators," Opt. Lett. **30**(20), 2700 (2005).

66. N. K. Berger, B. Levit, B. Fischer, M. Kulishov, D. V. Plant, and J. Azaña, "Temporal differentiation of optical signals using a phase-shifted fiber Bragg grating," Opt. Express **15**(2), 371 (2007).

67. M. H. Asghari and J. Azaña, "Design of all-optical high-order temporal integrators based on multiple-phase-shifted Bragg gratings," Opt. Express **16**(15), 11459 (2008).

68. M. H. Asghari and J. Azana, "On the Design of Efficient and Accurate Arbitrary-Order Temporal Optical Integrators Using Fiber Bragg Gratings," J. Light. Technol. **27**(17), 3888–3895 (2009).

69. T. Ma, K. Nallapan, H. Guerboukha, and M. Skorobogatiy, "Analog signal processing in the terahertz communication links using waveguide Bragg gratings: example of dispersion compensation," Opt. Express **25**(10), 11009 (2017).

70. M. H. Asghari and J. Azaña, "All-optical Hilbert transformer based on a single phase-shifted fiber Bragg grating: design and analysis," Opt. Lett. **34**(3), 334 (2009).

71. P. R. Griffiths and J. A. de Haseth, *Fourier Transform Infrared Spectrometry* (John Wiley & Sons, Inc., 2007).

72. M. van Exter, C. Fattinger, and D. Grischkowsky, "Terahertz time-domain spectroscopy of water vapor," Opt. Lett. **14**(20), 1128 (1989).

73. J. D. Jackson, *Classical Electrodynamics 2ed (1975)* (Wiley, 1975).

74. E. S. Lee and T.-I. Jeon, "Tunable THz notch filter with a single groove inside parallel-plate waveguides," Opt. Express **20**(28), 29605 (2012).

75. E. S. Lee, Y. Bin Ji, and T.-I. Jeon, "Terahertz band gap properties by using metal slits

in tapered parallel-plate waveguides," Appl. Phys. Lett. **97**(18), 181112 (2010).

76. E. S. Lee, J.-K. So, G.-S. Park, D. Kim, C.-S. Kee, and T.-I. Jeon, "Terahertz band gaps induced by metal grooves inside parallel-plate waveguides," Opt. Express **20**(6), 6116 (2012).

77. E. S. Lee, S.-G. Lee, C.-S. Kee, and T.-I. Jeon, "Terahertz notch and low-pass filters based on band gaps properties by using metal slits in tapered parallel-plate waveguides," Opt. Express **19**(16), 14852 (2011).

78. J. Capmany, J. Cascon, J. L. Martin, S. Sales, D. Pastor, and J. Marti, "Synthesis of fiber-optic delay line filters," J. Light. Technol. **13**(10), 2003–2012 (1995).

79. A. V. Oppenheim and R. W. Schafer, *Discrete-Time Signal Processing* (n.d.).

80. L. Venema, "Photonic technologies," Nature **424**(6950), 809–809 (2003).

81. M. Vasilyev, Y. Su, and C. J. McKinstrie, "Introduction to the Special Issue on Nonlinear-Optical Signal Processing," IEEE J. Sel. Top. Quantum Electron. **14**(3), 527–528 (2008).

82. A. V. Oppenheim, A. S. Willsky, and S. H. Nawab, *Signals and Systems* (Prentice Hall, 1997).

83. Ching-Wen Hsue, Lin-Chuan Tsai, and Yi-Hsien Tsai, "Time-constant control of microwave integrators using transmission lines," IEEE Trans. Microw. Theory Tech. **54**(3), 1043–1047 (2006).

84. C.-W. Hsue, L.-C. Tsai, and K.-L. Chen, "Implementation of First-Order and Second-Order Microwave Differentiators," IEEE Trans. Microw. Theory Tech. **52**(5), 1443–1448 (2004).

85. R. S. Tucker and K. Hinton, "Energy consumption and energy density in optical and electronic signal processing," IEEE Photonics J. **3**(5), 821–833 (2011).

86. E. L. Hines, E. Llobet, and J. W. Gardner, "Electronic noses: A review of signal processing techniques," IEE Proc. Circuits, Devices Syst. **146**(6), 297–310 (1999).

87. A. Klekamp, F. Buchali, and H. Bülow, "Electronic Dispersion Compensation," J. Light. Technol. Vol. 26, Issue 1, pp. 158-167 **26**(1), 158–167 (2008).

88. J. H. Keighley and P. Rhodes, "Derivative spectroscopy-I. The design and construction of an electronic differentiator," Infrared Phys. **12**(4), 277–285 (1972).

89. G. S. Campbell, "A micropower electronic integrator for meteorological applications," Agric. Meteorol. **13**(3), 399–404 (1974).

90. B. S. Kawasaki, K. O. Hill, D. C. Johnson, and Y. Fujii, "Narrow-band Bragg reflectors in optical fibers," Opt. Lett. **3**(2), 66 (1978).

91. M. A. Preciado and M. A. Muriel, "Ultrafast all-optical integrator based on a fiber Bragg

grating: proposal and design," Opt. Lett. **33**(12), 1348 (2008).

92. M. Asghari, C. Wang, J. Yao, and J. Azaña, "High-order passive photonic temporal integrators," Opt. Lett. **35**(8), 1191 (2010).

93. R. Kashyap, *Fiber Bragg Gratings* (Academic Press, 2010).

94. A. M. Vengsarkar, P. J. Lemaire, J. B. Judkins, V. Bhatia, T. Erdogan, and J. E. Sipe, "Long-period fiber gratings as band-rejection filters," J. Light. Technol. **14**(1), 58–65 (1996).

95. M. Kulishov, D. Krcmarík, and R. Slavík, "Design of terahertz-bandwidth arbitrary-order temporal differentiators based on long-period fiber gratings," Opt. Lett. **32**(20), 2978 (2007).

96. J. M. Lopez-Higuera, L. Rodriguez Cobo, A. Quintela Incera, and A. Cobo, "Fiber Optic Sensors in Structural Health Monitoring," J. Light. Technol. **29**(4), 587–608 (2011).

97. D. R. Walt, "Fibre optic microarrays," Chem. Soc. Rev. **39**(1), 38–50 (2010).

98. S.-H. Kim, E. S. Lee, Y. Bin Ji, and T.-I. Jeon, "Improvement of THz coupling using a tapered parallel-plate waveguide," Opt. Express **18**(2), 1289 (2010).

99. K. Iwaszczuk, A. Andryieuski, A. Lavrinenko, X.-C. Zhang, and P. U. Jepsen, "Terahertz field enhancement to the MV/cm regime in a tapered parallel plate waveguide," Opt. Express **20**(8), 8344 (2012).

100. V. R. Almeida, Q. Xu, C. A. Barrios, and M. Lipson, "Guiding and confining light in void nanostructure," Opt. Lett. **29**(11), 1209 (2004).

101. T. Monro, "Beyond the diffraction limit," Nat. Photonics **1**(2), 89–90 (2007).

102. J. S. Melinger, S. S. Harsha, N. Laman, and D. Grischkowsky, "Guided-wave terahertz spectroscopy of molecular solids [Invited]," J. Opt. Soc. Am. B **26**(9), A79 (2009).

103. M. Nagel, M. Först, and H. Kurz, "THz biosensing devices: fundamentals and technology," J. Phys. Condens. Matter **18**(18), S601–S618 (2006).

104. S. A. Maier, S. R. Andrews, L. Martín-Moreno, and F. J. García-Vidal, "Terahertz Surface Plasmon-Polariton Propagation and Focusing on Periodically Corrugated Metal Wires," Phys. Rev. Lett. **97**(17), 176805 (2006).

105. M. Naftaly and R. E. Miles, "Terahertz Time-Domain Spectroscopy for Material Characterization," Proc. IEEE **95**(8), 1658–1665 (2007).

106. R. Mendis and D. Grischkowsky, "Plastic ribbon THz waveguides," J. Appl. Phys. **88**(7), 4449 (2000).

107. S. P. Jamison, R. W. McGowan, and D. Grischkowsky, "Single-mode waveguide propagation and reshaping of sub-ps terahertz pulses in sapphire fibers," Appl. Phys. Lett. **76**(15), 1987–1989 (2000).

108. H. Han, H. Park, M. Cho, and J. Kim, "Terahertz pulse propagation in a plastic photonic crystal fiber," Appl. Phys. Lett. **80**(15), 2634–2636 (2002).

109. L.-J. Chen, H.-W. Chen, T.-F. Kao, J.-Y. Lu, and C.-K. Sun, "Low-loss subwavelength plastic fiber for terahertz waveguiding," Opt. Lett. **31**(3), 308 (2006).

110. M. Rozé, B. Ung, A. Mazhorova, M. Walther, and M. Skorobogatiy, "Suspended core subwavelength fibers: towards practical designs for low-loss terahertz guidance," Opt. Express **19**(10), 9127 (2011).

111. C. Yeh, F. Shimabukuro, and P. H. Siegel, "Low-loss terahertz ribbon waveguides," Appl. Opt. **44**(28), 5937 (2005).

112. A. Hassani, A. Dupuis, and M. Skorobogatiy, "Porous polymer fibers for low-loss Terahertz guiding," Opt. Express **16**(9), 6340 (2008).

113. B. Ung, A. Mazhorova, A. Dupuis, M. Rozé, and M. Skorobogatiy, "Polymer microstructured optical fibers for terahertz wave guiding," Opt. Express **19**(26), B848 (2011).

114. R. W. Boyd, *Nonlinear Optics* (Academic Press, 2008).

115. R. W. McGowan, G. Gallot, and D. Grischkowsky, "Propagation of ultrawideband short pulses of terahertz radiation through submillimeter-diameter circular waveguides," Opt. Lett. **24**(20), 1431 (1999).

116. T. I. Jeon, J. Zhang, and D. Grischkowsky, "THz Sommerfeld wave propagation on a single metal wire," Appl. Phys. Lett. **86**(16), 1–3 (2005).

117. M. Wächter, M. Nagel, and H. Kurz, "Frequency-dependent characterization of THz Sommerfeld wave propagation on single-wires," Opt. Express **13**(26), 10815 (2005).

118. K. Wang and D. M. Mittleman, "Metal wires for terahertz wave guiding," Nat. 2004 4327015 **432**(7015), 376 (2004).

119. R. Mendis and D. Grischkowsky, "Undistorted guided-wave propagation of subpicosecond terahertz pulses," Opt. Lett. **26**(11), 846 (2001).

120. R. Mendis and D. M. Mittleman, "Comparison of the lowest-order transverse-electric (TE1) and transverse-magnetic (TEM) modes of the parallel-plate waveguide for terahertz pulse applications.," Opt. Express **17**(17), 14839–50 (2009).

121. R. Mendis and D. Grischkowsky, "THz interconnect with low-loss and low-group velocity dispersion," IEEE Microw. Wirel. Components Lett. **11**(11), 444–446 (2001).

122. M. Mbonye, R. Mendis, and D. M. Mittleman, "A terahertz two-wire waveguide with low bending loss," Appl. Phys. Lett. **95**(23), 233506 (2009).

123. M. K. Mridha, A. Mazhorova, M. Clerici, I. Al-Naib, M. Daneau, X. Ropagnol, M. Peccianti, C. Reimer, M. Ferrera, L. Razzari, F. Vidal, and R. Morandotti, "Active terahertz two-wire waveguides," Opt. Express **22**(19), 22340 (2014).

124. H. Pahlevaninezhad and T. E. Darcie, "Coupling of terahertz waves to a two-wire waveguide," Opt. Express **18**(22), 22614 (2010).

125. H. Pahlevaninezhad, T. E. Darcie, and B. Heshmat, "Two-wire waveguide for terahertz," Opt. Express **18**(7), 7415 (2010).

126. R. Mendis, *First Broadband Experimental Study of Planar THz Waveguides* (n.d.).

127. W. H. (William H. Hayt and J. A. Buck, *Engineering Electromagnetics* (McGraw-Hill, 2012).

128. M. E. Van Valkenburg and W. M. Middleton, *Reference Data for Engineers: Radio, Electronics, Computers and Communications* (2001).

129. G. Yan, A. Markov, Y. Chinifooroshan, S. M. Tripathi, W. J. Bock, and M. Skorobogatiy, "Low-loss terahertz waveguide Bragg grating using a two-wire waveguide and a paper grating," Opt. Lett. **38**(16), 3089 (2013).

130. S. S. Haykin and B. Van Veen, *Signals and Systems* (Wiley, 2002).

131. D. Stranneby and W. Walker, *Digital Signal Processing and Applications: Second Edition* (Elsevier Ltd, 2004).

132. B. S. Nair, *Digital Electronics and Logic Design* (Prentice-Hall of India, 2006).

133. T. Ma, K. Nallapan, H. Guerboukha, and M. Skorobogatiy, "Analog signal processing in the terahertz communication links using waveguide Bragg gratings: example of dispersion compensation," Opt. Express **25**(10), 11009 (2017).

134. D. Dragoman and M. Dragoman, "Time-frequency signal processing of terahertz pulses," Appl. Opt. **43**(19), 3848–3853 (2004).

135. A. Rice, Y. Jin, X. F. Ma, X. C. Zhang, D. Bliss, J. Larkin, and M. Alexander, "Terahertz optical rectification from 〈110〉 zinc-blende crystals," Appl. Phys. Lett. **64**(11), 1324–1326 (1994).

136. D. J. Cook and R. M. Hochstrasser, "Intense terahertz pulses by four-wave rectification in air," Opt. Lett. **25**(16), 1210 (2000).

137. Y. Zhu, S. Vegesna, V. Kuryatkov, M. Holtz, M. Saed, and A. A. Bernussi, "Terahertz bandpass filters using double-stacked metamaterial layers," Opt. Lett. **37**(3), 296 (2012).

138. R. Mendis, A. Nag, F. Chen, and D. M. Mittleman, "A tunable universal terahertz filter using artificial dielectrics based on parallel-plate waveguides," Appl. Phys. Lett. **97**(13), 131106 (2010).

139. S. S. Harsha, N. Laman, and D. Grischkowsky, "High-Q terahertz Bragg resonances within a metal parallel plate waveguide," Appl. Phys. Lett. **94**(9), 091118 (2009).

140. Y.-J. Chiang, C.-S. Yang, Y.-H. Yang, C.-L. Pan, and T.-J. Yen, "An ultrabroad terahertz bandpass filter based on multiple-resonance excitation of a composite metamaterial,"

Appl. Phys. Lett. **99**(19), 191909 (2011).

141. S. F. Zhou, L. Reekie, H. P. Chan, Y. T. Chow, P. S. Chung, and K. Man Luk, "Characterization and modeling of Bragg gratings written in polymer fiber for use as filters in the THz region," Opt. Express **20**(9), 9564 (2012).

142. S. F. Zhou, L. Reekie, Y. T. Chow, H. P. Chan, and K. M. Luk, "Phase-Shifted Fiber Bragg Gratings for Terahertz Range," IEEE Photonics Technol. Lett. **24**(20), 1875–1877 (2012).

143. Z. Xie, X. Wang, J. Ye, S. Feng, W. Sun, T. Akalin, and Y. Zhang, "Spatial terahertz modulator," Sci. Rep. **3**(1), 1–4 (2013).

144. H. T. Chen, W. J. Padilla, M. J. Cich, A. K. Azad, R. D. Averitt, and A. J. Taylor, "A metamaterial solid-state terahertz phase modulator," Nat. Photonics **3**(3), 148–151 (2009).

145. D. Mittleman, "Device physics: A terahertz modulator," Nature **444**(7119), 560–561 (2006).

146. N. Karl, K. Reichel, H. T. Chen, A. J. Taylor, I. Brener, A. Benz, J. L. Reno, R. Mendis, and D. M. Mittleman, "An electrically driven terahertz metamaterial diffractive modulator with more than 20 dB of dynamic range," Appl. Phys. Lett. **104**(9), 091115 (2014).

147. K. S. Reichel, N. Lozada-Smith, I. D. Joshipura, J. Ma, R. Shrestha, R. Mendis, M. D. Dickey, and D. M. Mittleman, "Electrically reconfigurable terahertz signal processing devices using liquid metal components," Nat. Commun. **9**(1), 1–6 (2018).

148. T. Yasui, H. Takahashi, K. Kawamoto, Y. Iwamoto, K. Arai, T. Araki, H. Inaba, and K. Minoshima, "Widely and continuously tunable terahertz synthesizer traceable to a microwave frequency standard," Opt. Express **19**(5), 4428 (2011).

149. V. L. Bratman, Y. K. Kalynov, and V. N. Manuilov, "Large-orbit gyrotron operation in the terahertz frequency range," Phys. Rev. Lett. **102**(24), 245101 (2009).

150. M. Katoh and S. Bielawski, "Coherent terahertz synthesizer," Nat. Photonics **6**(2), 76–77 (2012).

151. A. Filin, M. Stowe, and R. Kersting, "Time-domain differentiation of terahertz pulses," Opt. Lett. **26**(24), 2008 (2001).

152. L. Chen, Z. Cheng, J. Xu, X. Zang, B. Cai, and Y. Zhu, "Controllable multiband terahertz notch filter based on a parallel plate waveguide with a single deep groove," Opt. Lett. **39**(15), 4541 (2014).

153. R. B. M. Schasfoort, ed., *Handbook of Surface Plasmon Resonance* (Royal Society of Chemistry, 2017).

154. R. S. Anwar, H. Ning, and L. Mao, "Recent advancements in surface plasmon polaritons-

plasmonics in subwavelength structures in microwave and terahertz regimes," Digit. Commun. Networks **4**(4), 244–257 (2018).

155. D. W. Matolak, A. Kodi, S. Kaya, D. Ditomaso, S. Laha, and W. Rayess, "Wireless networks-on-chips: Architecture, wireless channel, and devices," IEEE Wirel. Commun. **19**(5), 58–65 (2012).

156. J. M. Merlo, N. T. Nesbitt, Y. M. Calm, A. H. Rose, L. D'Imperio, C. Yang, J. R. Naughton, M. J. Burns, K. Kempa, and M. J. Naughton, "Wireless communication system via nanoscale plasmonic antennas," Sci. Rep. **6**(1), 1–8 (2016).

157. E. Abbe, *Gesammelte Abhandlungen* (G. Fischer, 1904).

158. C. R. Yonzon, E. Jeoung, S. Zou, G. C. Schatz, M. Mrksich, and R. P. Van Duyne, "A comparative analysis of localized and propagating surface plasmon resonance sensors: The binding of Concanavalin A to a monosaccharide functionalized self-assembled monolayer," J. Am. Chem. Soc. **126**(39), 12669–12676 (2004).

159. G. Raschke, S. Kowarik, T. Franzl, † C. Sönnichsen, A. T. A. Klar, J. Feldmann, A. N. And, and K. Kürzinger, "Biomolecular Recognition Based on Single Gold Nanoparticle Light Scattering," (2003).

160. E. Hutter and J. H. Fendler, "Exploitation of localized surface plasmon resonance," Adv. Mater. **16**(19), 1685–1706 (2004).

161. N. Fang, H. Lee, C. Sun, and X. Zhang, "Sub-diffraction-limited optical imaging with a silver superlens," Science (80-.). **308**(5721), 534–537 (2005).

162. I. I. Smolyaninov, J. Elliott, A. V. Zayats, and C. C. Davis, "Far-field optical microscopy with a nanometer-scale resolution based on the in-plane image magnification by surface plasmon polaritons," Phys. Rev. Lett. **94**(5), 057401 (2005).

163. H. A. Bethe, "Theory of diffraction by small holes," Phys. Rev. **66**(7–8), 163–182 (1944).

164. R. H. Ritchie, "Plasma Losses by Fast Electrons in Thin Films," Phys. Rev. **106**(5), 874–881 (1957).

165. C. J. Powell and J. B. Swan, "Origin of the characteristic electron energy losses in aluminum," Phys. Rev. **115**(4), 869–875 (1959).

166. H. Raether, *Surface Plasmons on Smooth and Rough Surfaces and on Gratings*, Springer Tracts in Modern Physics (Springer Berlin Heidelberg, 1988), **111**.

167. T. W. Ebbesen, H. J. Lezec, H. F. Ghaemi, T. Thio, and P. A. Wolff, "Extraordinary optical transmission through sub-wavelenght hole arrays," Nature **391**(6668), 667–669 (1998).

168. A. Sommerfeld, "Ueber die Fortpflanzung elektrodynamischer Wellen längs eines Drahtes," Ann. der Phys. und Chemie **303**(2), 233–290 (1899).

169. R. W. Wood, "On a Remarkable Case of Uneven Distribution of Light in a Diffraction

Grating Spectrum," Proc. Phys. Soc. London **18**(1), 269 (1902).

170. D. Pines, "Collective energy losses in solids," Rev. Mod. Phys. **28**(3), 184–198 (1956).

171. R. H. Ritchie, E. T. Arakawa, J. J. Cowan, and R. N. Hamm, "Surface-plasmon resonance effect in grating diffraction," Phys. Rev. Lett. **21**(22), 1530–1533 (1968).

172. E. Kretschmann and H. Raether, "Radiative Decay of Non Radiative Surface Plasmons Excited by Light," Zeitschrift fur Naturforsch. - Sect. A J. Phys. Sci. **23**(12), 2135–2136 (1968).

173. A. Otto, "Excitation of nonradiative surface plasma waves in silver by the method of frustrated total reflection," Zeitschrift für Phys. **216**(4), 398–410 (1968).

174. W. L. Barnes, A. Dereux, and T. W. Ebbesen, "Surface plasmon subwavelength optics," Nature **424**(6950), 824–830 (2003).

175. E. Ozbay, "Plasmonics: Merging Photonics and Electronics at Nanoscale Dimensions," Science (80-.). **311**(5758), 189–193 (2006).

176. J. B. Pendry, L. Martín-Moreno, and F. J. Garcia-Vidal, "Mimicking Surface Plasmons with Structured Surfaces," Science (80-.). **305**(5685), 847–848 (2004).

177. J. G. Rivas, M. Kuttge, P. H. Bolivar, H. Kurz, and J. A. Sánchez-Gil, "Propagation of Surface Plasmon Polaritons on Semiconductor Gratings," Phys. Rev. Lett. **93**(25), 256804 (2004).

178. F. J. García de Abajo and J. J. Sáenz, "Electromagnetic Surface Modes in Structured Perfect-Conductor Surfaces," Phys. Rev. Lett. **95**(23), 233901 (2005).

179. R. Ulrich and M. Tacke, "Submillimeter waveguiding on periodic metal structure," Appl. Phys. Lett. **22**(5), 251–253 (1973).

180. Y. Liang, H. Yu, H. C. Zhang, C. Yang, and T. J. Cui, "On-chip sub-terahertz surface plasmon polariton transmission lines in CMOS," Sci. Rep. **5**(1), 1–13 (2015).

181. S. Liu, X. Shou, and A. Nahata, "Coherent detection of multiband terahertz radiation using a surface plasmon-polariton based photoconductive antenna," IEEE Trans. Terahertz Sci. Technol. **1**(2), 412–415 (2011).

182. R. K. Vinnakota and D. A. Genov, "Terahertz optoelectronics with surface plasmon polariton diode," Sci. Rep. **4**(1), 1–6 (2014).

183. N. Yu, Q. J. Wang, M. A. Kats, J. A. Fan, S. P. Khanna, L. Li, A. G. Davies, E. H. Linfield, and F. Capasso, "Designer spoof surface plasmon structures collimate terahertz laser beams," Nat. Mater. **9**(9), 730–735 (2010).

184. M. Aghadjani, M. Erementchouk, and P. Mazumder, "Spoof Surface Plasmon Polariton Beam Splitter," IEEE Trans. Terahertz Sci. Technol. **6**(6), 832–839 (2016).

185. K. S. Kunz and R. J. Luebbers, *The Finite Difference Time Domain Method for*

Electromagnetics (CRC Press, 1993).

186. T. Jiang, L. Shen, X. Zhang, and L.-X. Ran, "High-order modes of spoof surface plasmon polaritons on periodically corrugated metal surfaces," Prog. Electromagn. Res. M **8**, 91–102 (2009).

187. F. J. Garcia-Vidal, L. Martín-Moreno, and J. B. Pendry, "Surfaces with holes in them: new plasmonic metamaterials," J. Opt. A Pure Appl. Opt. **7**(2), S97–S101 (2005).

188. L. Shen, X. Chen, Y. Zhong, and K. Agarwal, "Effect of absorption on terahertz surface plasmon polaritons propagating along periodically corrugated metal wires," Phys. Rev. B **77**(7), 075408 (2008).

189. L. Shen, X. Chen, and T.-J. Yang, "Terahertz surface plasmon polaritons on periodically corrugated metal surfaces," Opt. Express **16**(5), 3326 (2008).

190. Q. Zhang, J. J. Xiao, D. Han, F. F. Qin, X. M. Zhang, and Y. Yao, "Microwave band gap and cavity mode in spoof-insulator-spoof waveguide with multiscale structured surface," J. Phys. D. Appl. Phys. **48**(20), (2015).

191. Y. Meng, H. Xiang, R.-Y. Zhang, X. Wu, D. Han, C. T. Chan, and W. Wen, "Topological interface states in multiscale spoof-insulator-spoof waveguides," Opt. Lett. **41**(16), 3698 (2016).

192. L. Duvillaret, F. Garet, and J.-L. Coutaz, "A reliable method for extraction of material parameters in terahertz time-domain spectroscopy," IEEE J. Sel. Top. Quantum Electron. **2**(3), 739–746 (1996).

193. G. Gallot, J. Zhang, R. W. McGowan, T. I. Jeon, and D. Grischkowsky, "Measurements of the THz absorption and dispersion of ZnTe and their relevance to the electro-optic detection of THz radiation," Appl. Phys. Lett. **74**(23), 3450–3452 (1999).

194. G. Gallot, S. P. Jamison, R. W. McGowan, and D. Grischkowsky, "Terahertz waveguides," J. Opt. Soc. Am. B **17**(5), 851 (2000).

195. Q. Gan, Z. Fu, Y. J. Ding, and F. J. Bartoli, "Ultrawide-bandwidth slow-light system based on thz plasmonic graded metallic grating structures," Phys. Rev. Lett. **100**(25), 1–4 (2008).

196. A. Podzorov and G. Gallot, "Low-loss polymers for terahertz applications," Appl. Opt. **47**(18), 3254–3257 (2008).

197. Y. Park, J. Azaña, and R. Slavík, "Ultrafast all-optical first- and higher-order differentiators based on interferometers," Opt. Lett. **32**(6), 710 (2007).

198. M. A. Preciado, V. Garcia-Muñoz, and M. A. Muriel, "Ultrafast all-optical Nth-order differentiator based on chirped fiber Bragg gratings," Opt. Express **15**(12), 7196 (2007).

199. J.-H. Kang, D.-S. Kim, and M. Seo, "Terahertz wave interaction with metallic nanostructures," Nanophotonics **7**(5), 763–793 (2018).

200. M. A. Seo, H. R. Park, S. M. Koo, D. J. Park, J. H. Kang, O. K. Suwal, S. S. Choi, P. C. M. Planken, G. S. Park, N. K. Park, Q. H. Park, and D. S. Kim, "Terahertz field enhancement by a metallic nano slit operating beyond the skin-depth limit," Nat. Photonics **3**(3), 152–156 (2009).

201. K. Iwaszczuk, A. Andryieuski, A. Lavrinenko, X.-C. Zhang, and P. U. Jepsen, "Non-invasive terahertz field imaging inside parallel plate waveguides," Appl. Phys. Lett. **99**(7), 071113 (2011).

202. S. A. Glantz and B. K. Slinker, *Primer of Applied Regression & Analysis of Variance* (McGraw-Hill, Medical Pub. Division, 2001).

203. F. M. Dekking, C. Kraaikamp, H. P. Lopuhaä, and L. E. Meester, *A Modern Introduction to Probability and Statistics*, Springer Texts in Statistics (Springer London, 2005).

204. E. L. Lehmann and G. Casella, *Theory of Point Estimation* (Springer, 2013).

205. A. G. Barnston, "Correspondence among the correlation, RMSE, and Meidke Foresast verification measures; Refinement of the Neidke Score," Weather Forecast. **7**(4), 699–709 (1992).

206. P. Tannouri, M. Peccianti, P. L. Lavertu, F. Vidal, and R. Morandotti, "Quasi-TEM mode propagation in twin-wire THz waveguides (Invited Paper)," Chinese Opt. Lett. Vol. 9, Issue 11, pp. 110013- **9**(11), 110013 (2011).

207. S. Ramo, J. R. Whinnery, and T. Van Duzer, *Fields and Waves in Communication Electronics* (Wiley, 1994).

208. H. A. Bethe, "Theory of diffraction by small holes," Phys. Rev. **66**(7–8), 163–182 (1944).

209. N. Karpowicz, J. Dai, X. Lu, Y. Chen, M. Yamaguchi, H. Zhao, X.-C. Zhang, L. Zhang, C. Zhang, M. Price-Gallagher, C. Fletcher, O. Mamer, A. Lesimple, and K. Johnson, "Coherent heterodyne time-domain spectrometry covering the entire “terahertz gap,”" Appl. Phys. Lett. **92**(1), 011131 (2008).

210. J. Dai, X. Xie, and X.-C. Zhang, "Detection of Broadband Terahertz Waves with a Laser-Induced Plasma in Gases," Phys. Rev. Lett. **97**(10), 103903 (2006).

211. D. J. Cook, J. X. Chen, E. A. Morlino, and R. M. Hochstrasser, "Terahertz-field-induced second-harmonic generation measurements of liquid dynamics," Chem. Phys. Lett. **309**(3–4), 221–228 (1999).

212. J. Dai, B. Clough, I.-C. Ho, X. Lu, J. Liu, and X.-C. Zhang, "Recent Progresses in Terahertz Wave Air Photonics," IEEE Trans. Terahertz Sci. Technol. **1**(1), 274–281 (2011).

213. J. Dai, J. Liu, and X.-C. Zhang, "Terahertz Wave Air Photonics: Terahertz Wave Generation and Detection With Laser-Induced Gas Plasma," IEEE J. Sel. Top. Quantum Electron. **17**(1), 183–190 (2011).

214. D. R. Lide, "CRC handbook of chemistry and physics : a ready reference book of chemical and physical," 2454 (1928).

215. J. Hebling, G. Almasi, I. Kozma, and J. Kuhl, "Velocity matching by pulse front tilting for large area THz-pulse generation," Opt. Express **10**(21), 1161 (2002).

216. J. Hebling, A. G. Stepanov, G. Almási, B. Bartal, and J. Kuhl, "Tunable THz pulse generation by optical rectification of ultrashort laser pulses with tilted pulse fronts," Appl. Phys. B Lasers Opt. **78**(5), 593–599 (2004).

217. F. Blanchard, X. Ropagnol, H. Hafez, H. Razavipour, M. Bolduc, R. Morandotti, T. Ozaki, and D. G. Cooke, "Effect of extreme pump pulse reshaping on intense terahertz emission in lithium niobate at multimilliJoule pump energies," Opt. Lett. **39**(15), 4333 (2014).

218. A. Tomasino, A. Parisi, S. Stivala, P. Livreri, A. C. Cino, A. C. Busacca, M. Peccianti, and R. Morandotti, "Wideband THz Time Domain Spectroscopy based on Optical Rectification and Electro-Optic Sampling," Sci. Rep. **3**(1), 3116 (2013).

219. J. Hebling, G. Almasi, I. Kozma, and J. Kuhl, "Velocity matching by pulse front tilting for large area THz-pulse generation," Opt. Express **10**(21), 1161 (2002).

220. H. Hamster, A. Sullivan, S. Gordon, W. White, and R. W. Falcone, "Subpicosecond, electromagnetic pulses from intense laser-plasma interaction," Phys. Rev. Lett. **71**(17), 2725–2728 (1993).

221. K. Tanaka, H. Hirori, and M. Nagai, "THz Nonlinear Spectroscopy of Solids," IEEE Trans. Terahertz Sci. Technol. **1**(1), 301–312 (2011).

222. H. Hirori and K. Tanaka, "Nonlinear Optical Phenomena Induced by Intense Single-Cycle Terahertz Pulses," IEEE J. Sel. Top. Quantum Electron. **19**(1), 8401110–8401110 (2013).

223. H. Hamster, A. Sullivan, S. Gordon, W. White, and R. W. Falcone, *Subpicosecond, Electromagnetic Pulses from Intense Laser-Plasma Interaction* (1993), **71**.

224. J. Dai, X. Xie, and X. C. Zhang, "Detection of broadband terahertz waves with a laser-induced plasma in gases," Phys. Rev. Lett. **97**(10), 103903 (2006).

225. M. Kress, T. Löffler, S. Eden, M. Thomson, and H. G. Roskos, "Terahertz-pulse generation by photoionization of air with laser pulses composed of both fundamental and second-harmonic waves," Opt. Lett. **29**(10), 1120 (2004).

226. X. Xie, J. Dai, and X.-C. Zhang, "Coherent Control of THz Wave Generation in Ambient Air," Phys. Rev. Lett. **96**(7), 075005 (2006).

227. P. Klarskov, A. C. Strikwerda, K. Iwaszczuk, and P. U. Jepsen, "Experimental three-dimensional beam profiling and modeling of a terahertz beam generated from a two-color air plasma," New J. Phys. **15**(13pp), 75012 (2013).

LIST OF FIGURES

LIST OF TABLES

LIST OF ABBREVIATIONS

ABCD	Air-Biased Coherent Detection
ASP	Analog Signal-Processing
BBO	β-Barium Borate
BG	Bragg Grating
CoD	Coefficient of Determination
CW	Continuous Wave
DFG	Difference-Frequency Generation
DSP	Digital Signal-Processing
EM	Electromagnetic
EO	Electro-Optic
EOS	Electro-Optic Sampling
FBG	Fiber Bragg Grating
FDTD	Finite Difference in the Time Domain
FE	Field Enhancement
FFT	Fast Fourier Transform
FIR	Far Infrared
FS-EOS	Free-Space Electro-Optic Sampling
FTIR	Fourier-Transform Infrared
Gbps	Gigabit per second
GVD	Group Velocity Dispersion
HCWG	Hollow-Circular Waveguide
HDPE	High-Density Polyethylene
HLSW	Horizontally-Localized Standing Wave
ICT	Information and Communication Technologies
IoT	Internet of Things

IR	Infrared
LMN	Laboratory of Micro- and Nanofabrication
LPG	Long Period Grating
LTG	Low-Temperature Grown
MMW	Millimeter Wave
NIR	Near Infrared
OBCD	Optically-Biased Coherent Detection
OR	Optical Rectification
PCA	Photoconductive Antenna
PCS	Photoconductive Sampling
PEC	Perfect Electric Conductor
PMMA	Polymethyl Methacrylate
PMT	Photomultiplier Tube
PPWG	Parallel-Plate Waveguide
PSP	Photonic Signal Processing
RF	Radio-Frequency
RMSE	Root Mean Squared Error
SH	Second Harmonic
SP	Surface Plasmons
SPP	Surface Plasmon Polaritons
SPR	Surface Plasmon Resonance
SSBCD	Solid-State-Biased Coherent Detection
SSPP	Spoof Surface Plasmon Polaritons
SWWG	Single-Wire Waveguide
TDS	Time-Domain Spectroscopy
TE	Transverse Electric
TEM	Transverse Electromagnetic
TFISH	Terahertz-Field-Induced Second Harmonic
THz	Terahertz
TM	Transverse Magnetic

TPPWG	Tapered Parallel-Plate Waveguide
TTWWG	Tapered Two-Wire Waveguide
TWWG	Two-Wire Waveguide
UV	Ultra-Violet
VLSW	Vertically-Localized Standing Wave